

**ELECTRONIC, MAGNETIC, AND
MECHANICAL PROPERTIES OF NOVEL
TWO DIMENSIONAL MONOLAYER
MATERIALS**

**A Thesis Submitted to
the Graduate School of Engineering and Sciences of
İzmir Institute of Technology
in Partial Fulfillment of the Requirements for the Degree of**

DOCTOR OF PHILOSOPHY

in Physics

**by
Mehmet YAĞMURCUKARDEŞ**

**July 2017
İZMİR**

We approve the thesis of **Mehmet YAĞMURCUKARDEŞ**

Examining Committee Members:

Prof. Dr. R. Tuğrul SENGER

Department of Physics, İzmir Institute of Technology

Assoc. Prof. Dr. Haldun SEVİNÇLİ

Department of Materials Science and Engineering, İzmir Institute of Technology

Assoc. Prof. Dr. A. Devrim GÜÇLÜ

Department of Physics, İzmir Institute of Technology

Prof. Dr. Hamza POLAT

Department of Physics, Dokuz Eylül University

Assoc. Prof. Dr. Engin DURGUN

Department of Materials Science and Nanotechnology, Bilkent University

27 July 2017

Prof. Dr. R. Tuğrul SENGER

Supervisor, Department of Physics
İzmir Institute of Technology

Assoc. Prof. Dr. Hasan ŞAHİN

Co-Supervisor, Department of Photonics
İzmir Institute of Technology

Prof. Dr. R. Tuğrul SENGER

Head of the Department of
Physics

Prof. Dr. Aysun SOFUOĞLU

Dean of the Graduate School of
Engineering and Sciences

ACKNOWLEDGMENTS

First of all, I would like to express my deeply thanks to my advisor Prof. Dr. R. Tuğrul SENGER for his intensive guidance, patient instruction, generous help and support in my studies and this thesis work.

I would like to specially thank to my co-advisor Assoc. Prof. Dr. Hasan ŞAHİN for his great contributions and unique assistance.

I would also like to thank my group mates Cihan BACAŞIZ and Fadıl İYİKANAT, my best friends Selma Mayda, Duygu Özaydın, Atike İnce, Elif Özçeri, and Hasan Aydın for their unique friendship and special motivation at difficult times.

Most importantly, none of this would have been possible without the love and patience of my family. I would like to express my heart-felt gratitude to my parents, sisters and brothers, my wife Nesli Yağmurcukardeş for everything they have done for me.

Finally, I would like to take the opportunity to thank all persons in İYTE who have ever helped me before.

This research was supported by TUBİTAK with 111T318 and 114F397 project numbers.

ABSTRACT

ELECTRONIC, MAGNETIC, AND MECHANICAL PROPERTIES OF NOVEL TWO DIMENSIONAL MONOLAYER MATERIALS

Layered materials exhibit different properties when they are thinned down to a few monolayers. Following the successful isolation of graphene in 2004, there has been a rapid increase in the number of studies focusing on other novel two dimensional (2D) materials such as hexagonal Boron Nitride (BN), transition metal dichalcogenides (TMDs), post transition metal chalcogenides (PTMCs), and in-plane anisotropic monolayers (Re-dichalcogenides and blackphosphorus). In addition to their electronic, optical, and magnetic properties, mechanical properties of 2D materials are of fundamental importance. Measurements of elastic constants of 2D materials are still challenging. Therefore, theoretical investigation of the mechanical properties is particularly important. Moreover, investigation of Raman spectra of these materials requires a thorough understanding of their vibrational properties. In these regards, we investigate the electronic, magnetic, and mechanical properties of some novel monolayer 2D materials (such as, auxetic pentagonal monolayers, flexible monolayers of holey graphene crystals, ultra-flexible monolayers of PTMCs, and in-plane anisotropic monolayers of ReS_2 and blackphosphorus) by means of first-principles calculations based on density functional theory (DFT). In addition, tuning electronic properties of a van der Waals heterobilayer structure composed of monolayers of $\text{Mg}(\text{OH})_2$ and WS_2 upon an external out-of-plane electric field is studied. The effect of biaxial strain on the vibrational properties of novel 2D materials is also studied through their off-resonant Raman activities. Our findings will be useful to clarify several issues related to the experiments of novel 2D materials.

ÖZET

YENİ İKİ BOYUTLU TEK KATMANLI MALZEMELERİN ELEKTRONİK, MANYETİK VE MEKANİK ÖZELLİKLERİ

Katmanlı yapılar birkaç katmana indirgendiklerinde farklı özellikler sergilemektedir. Grafenin 2004 yılında başarılı bir şekilde izole edilmesini takiben, hegzagonal Boron Nitrat (BN), geçiş metali dikalkojenleri (GMD), post geçiş metali kalkojenleri (PGMK), ve düzlem içi anisotropik karafosfor yapıları gibi diğer iki boyutlu malzemeler üzerine yapılan çalışmalarda hızlı bir artış olmuştur. İki boyutlu tek katmanlı malzemenin elektronik, optik, ve manyetik özelliklerine ek olarak mekanik özellikleride temel önem arz etmektedir. İki boyutlu malzemelerin elastil sabitlerinin ölçülmesi hala ilgi çekicidir. Bu yüzden, mekanik özelliklerin teorik olarak araştırılması önemlidir. Buna ek olarak, bu malzemelerin Raman spektrumunun araştırılması titreşimsel özelliklerinin anlaşılmasını gerektirmektedir. Bu bağlamda, auxetik tek katmanlı pentagonal yapılar, esnek tek katmanlı delikli grafen kristalleri, ultra-esnek tek katmanlı PGMK lar, ve düzlem içi anisotropik tek katmanlı ReS₂ ve karafosfor gibi bazı yeni iki boyutlu malzemelerin elektronik, manyetik ve mekanik özelliklerini ilk prensiplere dayanan yoğunluk fonksiyoneli teorisi tabanlı hesaplamalar yoluyla araştırdık. Ek olarak, tek katmanlı Mg(OH)₂ ve WS₂ yapılarından oluşan iki katmanlı van der Waals hetero yapısının elektronik özelliklerinin düzlem dışı bir elektrik alan altında ayarlanması çalışılmıştır. İki eksenli gerilmenin yeni iki boyutlu malzemelerin titreşimsel özelliklerine olan etkisi bu malzemelerin rezonant olmayan Raman aktiviteleri vasıtasıyla çalışılmıştır. Bulgularımız yeni iki boyutlu malzemelerin deneylerine ilişkin birçok sorunun açıklığa kavuşmasında yararlı olacaktır.

To my wife Nesli and my lovely baby Nesil...

TABLE OF CONTENTS

LIST OF FIGURES	x
LIST OF TABLES	xv
CHAPTER 1. INTRODUCTION	1
CHAPTER 2. METHODOLOGY	7
2.1. Many-Electron Systems	7
2.1.1. Born-Oppenheimer Approximation	8
2.1.2. Thomas-Fermi Model	9
2.1.3. Density Functional Theory	9
2.1.3.1. Hohenberg-Kohn Theorems	10
2.1.3.2. The Kohn-Sham Equations	10
2.1.3.3. The Types of Exchange-Correlation Functionals	12
2.2. Mechanical Properties of Materials	13
2.2.1. Elastic Constants	13
2.2.1.1. Young Modulus	14
2.2.1.2. Poisson Ratio	14
2.2.2. Elastic Constants in 2D Limit	15
2.2.2.1. In-plane Stiffness	15
2.2.3. Stress-Strain Relation	18
2.3. Theory of Phonons	20
2.3.1. Raman Spectrum	22
2.3.1.1. Theory of Raman Activity	23
2.4. Computational Details	27
CHAPTER 3. MECHANICAL PROPERTIES OF MONOLAYERS OF PENTAG- ONAL CRYSTAL STRUCTURE	29
3.1. Structural Properties	30
3.2. Electronic Properties	32
3.3. Elastic Constants	34
3.4. Conclusions	38

CHAPTER 4. PREDICTION OF NOVEL 2D MONOLAYERS OF HOLEY GRAPHENE	
CRYSTALS	40
4.1. Structural Properties.....	41
4.2. Electronic And Magnetic Properties	44
4.3. Mechanical Properties.....	45
4.4. Effect Of Defects	47
4.5. Conclusion.....	50
 CHAPTER 5. FLEXIBLE MONOLAYERS OF GA-MONOCHALCOGENIDES	
(GAS AND GASE)	52
5.1. Structural and electronic properties	54
5.2. Linear and Non-Linear Elastic Properties.....	57
5.2.1. In-plane Stiffness	57
5.2.2. Poisson Ratio	59
5.2.3. Ultimate Strength.....	60
5.2.4. Dynamical Instability	61
5.3. Conclusion.....	63
 CHAPTER 6. HYDROGEN-INDUCED STRUCTURAL TRANSITION IN SIN-	
GLE LAYER ReS ₂	65
6.1. Structural and Electronic Properties.....	67
6.1.1. Monolayer ReS ₂	67
6.1.2. Single H-atom Adsorption on Monolayer ReS ₂	68
6.1.3. Full-Hydrogenation of Monolayer ReS ₂	70
6.2. Linear Elastic Properties of Monolayer ReS ₂ and 1T ^{Re₂} -ReS ₂ H ₂	
Crystals	71
6.3. Conclusion.....	74
 CHAPTER 7. Mg(OH) ₂ -WS ₂ HETEROBILAYER: ELECTRIC FIELD TUNABLE	
BANDGAP CROSSOVER	76
7.1. Single layer Mg(OH) ₂ and WS ₂	77
7.2. Heterobilayer	79
7.3. Effect of External Electric Field	81
7.4. Conclusion.....	83

CHAPTER 8. STRAIN-DEPENDENT VIBRATIONAL PROPERTIES OF NOVEL TWO DIMENSIONAL SINGLE LAYER CRYSTALS	85
8.1. Strain-Dependent Raman Activity	87
8.1.1. Mono-Elemental Single-Layer Crystals.....	88
8.1.2. Diatomic Single-Layer Crystals	90
8.1.3. TMDs Single-Layer Crystals	92
8.1.4. Anisotropic Single-Layer Crystals	95
8.1.4.1. Rhenium Dichalcogenides (ReS ₂ and ReSe ₂) Single- Layer Crystals	96
8.1.4.2. Monolayer Black Phosphorus Single-Layer Crystal	99
8.2. Conclusions.....	102
 CHAPTER 9. CONCLUSION	 104
 REFERENCES	 106

LIST OF FIGURES

<u>Figure</u>	<u>Page</u>
Figure 2.1. A general stress-strain curve demonstrating elastic and plastic regions for a material including defects or dislocations which are the generators of plastic region.	18
Figure 2.2. A typical experimental setup for the Raman scattering process. \hat{e}_i and \hat{e}_s represent the polarization vectors of incident light and scattered radiation.	25
Figure 3.1. Top view and side view of pentagonal (a) graphene (b) AgN ₃ , (c) B ₂ N ₄ , (d) B ₄ N ₂	30
Figure 3.2. Band-structures of pentagonal (a) graphene (b) AgN ₃ , (c) B ₂ N ₄ , (d) B ₄ N ₂ where blue lines denote up spins while dashed red lines denote down spins respectively.	33
Figure 3.3. Charge density difference of pentagonal (a) graphene, (b) AgN ₃ , (c) B ₂ N ₄ and (d) B ₄ N ₂	35
Figure 3.4. Energy variation of the pentagonal structures under applied strain and the corresponding atomic configurations at given strain strengths.	37
Figure 3.5. Phonon modes of pentagonal (a) graphene (b) AgN ₃ , (c) B ₂ N ₄ , (d) B ₄ N ₂	38
Figure 4.1. Top view of C ₂ X holey graphene monolayer structure where X represents N, P or As atoms.	41
Figure 4.2. Band-structures (left-panel) and corresponding partial density of states (right-panel) of (a) C ₂ N (b) C ₂ P, and (c) C ₂ As where red curves are for bands calculated within GGA approximation while dashed blue curves are for bands calculated within HSE06 on top of GGA. The Fermi energy (E_F) level is set to the valence band maximum.	43
Figure 4.3. Charge density difference, $\rho_{up}-\rho_{down}$, of C ₂ As monolayer structure for (a) fully anti-ferromagnetic (AFM-1) order and (b) anti-ferromagnetic order in the benzene ring (AFM-2) where green/yellow color is for minority/majority spin states. The plotted isosurface values are $10^{-3} e/\text{\AA}^3$ and $10^{-5} e/\text{\AA}^3$ for (a) and (b) respectively.	45
Figure 4.4. (a) Change of total energy of the three holey graphene monolayers under applied strain. Structural changes under applied strain of (b) C ₂ N, (c) C ₂ P and (d) C ₂ As.	46

Figure 4.5. Optimized X-vacancy and their H substituted structures of (a) C ₂ N, (b) C ₂ P, (c) C ₂ As respectively.	48
Figure 4.6. Total DOS for defected and H-impurity structures of (a) C ₂ N, (b) C ₂ P, and (c) C ₂ As respectively.	50
Figure 5.1. Top and side view of monolayer (a) GaS and (b) GaSe. Red dashed lines represent the rectangular unit cell and <i>a</i> and <i>b</i> are the lattice vectors. <i>h</i> is the thickness of the monolayer GaS and GaSe crystals. The charge distribution on the individual atoms for monolayer (c) GaS and (d) GaSe are shown in side view. Increasing charge density is shown by a color scheme from blue to red with linear scaling between zero (blue) and 6.7 e/Å ³ (red). (e) and (f) show the calculated energy-band structure within GGA+SOC and GGA+SOC+GW approximations for monolayer GaS and GaSe, respectively. The Fermi energy (<i>E_F</i>) level is set to the valence band maximum. The red dashed lines indicate the GW band structure while blue lines indicate the indirect GGA+SOC band structure.	53
Figure 5.2. Calculated energy-band structures within GGA for different applied strain values for monolayer (a) GaS and (c) GaSe. The Fermi energy (<i>E_F</i>) level is set to the VBM of each structure. The change in the band gap with applied strain for monolayer (b) GaS and (d) GaSe.	55
Figure 5.3. (a) The change of strain energy and (b) the created stress in the different monolayer materials under applied biaxial strain. (c) The geometries of each monolayer crystals at fracture strain values.	56
Figure 5.4. Total charge density difference between the bare and 0.1 charged ($\rho_{0.1}-\rho_0$), and 0.2 charged ($\rho_{0.2}-\rho_0$) cases for monolayer GaS and GaSe. Increasing charge density is shown by a color scheme from blue to red with linear scaling between zero (blue) and maximum charge (red).	58
Figure 5.5. In-plane stiffness values: (a) lattice constant, (b) cohesive energy per atom, and (c) work function of monolayer GaS and GaSe crystals. The number near the symbols gives the amount of added charge per unit cell.	60
Figure 5.6. Poisson ratio values: (a) lattice constant, (b) cohesive energy per atom, and (c) work function of monolayer GaS and GaSe crystals. The numbers above the symbols refer to the amount of added charge per unit cell.	61

Figure 5.7. Phonon-band dispersions for monolayer (a) GaS at 17% and (b) GaSe 18% biaxial strains. The three acoustic phonon modes are given on the right panel.	62
Figure 6.1. For the monolayer ReS ₂ ; (a) top and side views of the structure, (b) the phonon-band structure, (c) VBM and CBM surfaces. (d) The corresponding partial density of states.	66
Figure 6.2. (a) Possible adsorption sites for a single H atom, labeled by numbers. (b) Top and side views of single H adsorbed monolayer ReS ₂ and (c) the corresponding partial density of states (PDOS).	68
Figure 6.3. (a) Top and side views of monolayers of 1T-ReS ₂ H ₂ (top panel) and 1T^{Re2} -ReS ₂ H ₂ (bottom panel). Corresponding phonon-band dispersions for (b) 1T ReS ₂ H ₂ and (c) 1T^{Re2} -ReS ₂ H ₂ . (d) The phase transition from Re ₄ clusters in bare structure (on the left side) to Re ₂ dimers in 1T^{Re2} -ReS ₂ H ₂ (on the right side) and the corresponding charge densities on the same Re-planes.	69
Figure 6.4. For the monolayer 1T^{Re2} -ReS ₂ H ₂ ; (a) VBM and CBM surfaces and (b) the corresponding partial density of states.	69
Figure 6.5. Time vs. temperature diagrams of the MD simulations. Two sets of calculations are given. (a) and (c) show the first set in which the temperature increases from 0 to 800 K for the monolayer ReS ₂ and 1T^{Re2} -ReS ₂ H ₂ , respectively. (b) and (d) show the second set in which the temperature increases from 700 to 1500 K for the monolayer ReS ₂ and 1T^{Re2} -ReS ₂ H ₂ , respectively. (b) indicates that the monolayer ReS ₂ remains stable even at 1500 K. In (d), the dissociation of the 1T^{Re2} -ReS ₂ H ₂ appears as a sudden increase in the system temperature at ~2 ps. In lower panel, the structural forms of the 1T^{Re2} -ReS ₂ H ₂ are shown before and after dissociation.	73
Figure 7.1. Top and side view of monolayers of (a) Mg(OH) ₂ and (b) WS ₂ . The charge distribution on the individual atoms are shown in top and side views of (c) Mg(OH) ₂ and (d) WS ₂ . Increasing charge density is shown by a color scheme from blue to red with the formula $F(N)=1 \times 1000^{N/step}$ where step size taken to be 10 and N ranges from -1 to 2.	78
Figure 7.2. Calculated energy-band structure of monolayer (a) Mg(OH) ₂ and (b) WS ₂ . The Fermi energy (E_F) level is set to the valence band maximum.	80

Figure 7.3. Different possible stacking configurations for the heterobilayer structure. (a) W atom on top of Mg atom, (b) W atom on top of upper OH group, and (c) W atom on top of lower OH group.	80
Figure 7.4. The band structure (left) and the corresponding partial density of states (PDOS) (right) of the heterobilayer structure calculated within SOC. The Fermi energy (E_F) level is set to the valence band maximum.	81
Figure 7.5. (a) The effect of an external out-of-plane electric field on the band structure of the heterobilayer and (b) the corresponding band alignments (vacuum levels are set to zero). The band gap regions are highlighted in yellow while the CBM and VBM are highlighted in pink and gray for $Mg(OH)_2$ and WS_2 , respectively.	82
Figure 8.1. Top and side view of typical single-layer structures; (a) mono-atomic, (b) diatomic, (c) TMDs, (d) anisotropic single-layer structures, and (e) black phosphorus. Color code of atoms given in corresponding figure. Primitive cells are indicated with red solid lines.	86
Figure 8.2. The response of activity of Raman active modes to the applied biaxial strain for (a) graphene, (b) silicene, and (c) germanene. The insets in (b) and (c) are for ZO phonon mode.	89
Figure 8.3. The response of activity of Raman active modes to the applied biaxial strain for single-layer (a) h -BN, (b) h -AlN, and (c) h -GaN. The given response is for the LO-TO phonon mode which is the only Raman active mode for diatomic single-layers.	91
Figure 8.4. (a) The response of frequencies and (b) Raman activities of Raman active modes to the applied biaxial strain for single-layers of mono- and di-atomic crystal structures.	94
Figure 8.5. The response of activity of Raman active modes to the applied biaxial strain for single-layer (a) MoS_2 , (b) WS_2 , (c) $MoSe_2$, and (d) WSe_2 . The vibrational motions of atoms in corresponding phonon modes are shown below.	95
Figure 8.6. The response of frequencies of Raman active modes and their Raman activities to the applied biaxial strain for single-layers of TMDs for (a) E' mode and (b) A_1	96
Figure 8.7. The response of frequencies and Raman activities of 18 Raman active modes of single-layer ReS_2 to the biaxial strain.	98

Figure 8.8. The response of frequencies and Raman activities of 18 Raman active modes of single-layer ReSe ₂ to the biaxial strain.	99
Figure 8.9. (a) The response of frequencies and (b) Raman activities of 6 Raman active modes of single-layer BP to the biaxial strain. Vibrational motion of P atoms in each phonon mode are given below.	100
Figure 8.10. The response of 3 prominent Raman active modes of single-layer BP to the applied biaxial strain.	101

LIST OF TABLES

<u>Table</u>	<u>Page</u>
Table 3.1. Geometry of pentagonal structures, calculated lattice parameter a , the distance between atoms d_{XY} , buckling of the monolayer h , total magnetic moment μ , the amount of charge lost or gained by the atoms $\Delta\rho$, the total cohesive energy of a primitive unitcell E_c , the energy band gap of the structure E_g , work function Φ , Poisson's ratio ν and in-plane stiffness C	31
Table 4.1. The calculated ground state properties of C_2X -structures, structural geometry, lattice parameters of primitive unit cell, a (see Fig. 4.1); the distance between C-X atoms, d_{C-X} ; the distance between two carbon atoms, d_{C-C} ; the average charge donated to (+) or from (-) each C atom, $\Delta\rho$; the cohesive energy per atom in primitive unitcell, E_{coh} ; the energy band gap of the structure calculated within, GGA with the inclusion of SOC, E_g^{GGA} , and HSE06, E_g^{HSE} ; workfunction, Φ ; Poisson's ratio, ν ; and in-plane stiffness C . Calculated parameters for graphene and h-BN are given for comparison. ¹ (Lee <i>et al.</i> , 2008) and ² (Berseneva <i>et al.</i> , 2013)	42
Table 4.2. The calculated ground state properties of defected C_2X -structures, structural geometry, lattice parameters of 2×2 supercell, a and b , the net magnetic moment of the structure, μ , and the cohesive energy per atom in supercell E_{coh}	49
Table 5.1. The calculated ground state properties of monolayer graphene, MoS ₂ , GaS and GaSe crystals: proper thickness h_p , magnetic state, the amount of charge received by the a chalcogenide atom $\Delta\rho$, calculated energy band gap within GGA (E_g^{GGA}), SOC (E_g^{SOC}), GW (E_g^{GW}), and workfunction Φ , in-plane stiffness C , Poisson ratio ν , ultimate strength σ_U , ultimate strain ε_U , and fracture strain ε_F . ¹ (Shi <i>et al.</i> , 2013)	54
Table 6.1. For the monolayer ReS ₂ and $1T^{Re_2}$ -ReS ₂ H ₂ structures; structure, calculated lattice parameters a and b , the average charge donation of a Re atom, $\Delta\rho$, the energy band gap of the structures calculated within; GGA (E_g^{GGA}), SOC on top of GGA (E_g^{SOC}), and the work function Φ . ..	67

Table 6.2.	Elastic parameters along \perp - (perpendicular to Re_4 chains) and \parallel -directions (parallel to Re_4 chains) for the monolayers of ReS_2 and $1\text{T}^{\text{Re}_2}\text{-ReS}_2\text{H}_2$ structures; calculated in-plane stiffness C_{\perp} and C_{\parallel} , Poisson ratio ν_{\perp} and ν_{\parallel} , effective Young modulus E_{\perp} and E_{\parallel}	71
Table 7.1.	The calculated ground state properties of monolayer and their heterobilayer structures: structure, lattice parameters of primitive unit cell, a and b (see Fig. 7.1), the distance between the individual atoms contained in each monolayer d_{X-Y} , magnetic state, the total amount of charge received by the O or S atoms $\Delta\rho$, the energy band gap of the structure calculated within GGA ($E_{\text{g}}^{\text{GGA}}$), SOC ($E_{\text{g}}^{\text{SOC}}$) and HSE06 ($E_{\text{g}}^{\text{HSE}}$), and workfunction Φ determined from $\text{Mg}(\text{OH})_2$ side.	78
Table 8.1.	For the single-layer crystal structures; the structure, planar (PL), low-buckled (LB), or puckered (P), calculated lattice parameters a and b , the point group of the single-layer, total number of Raman active phonon modes, the in-plane static (low-frequency) dielectric constant, ϵ , and the energy-band gap of the structures calculated within SOC on top of GGA ($E_{\text{g}}^{\text{SOC}}$). Note : * The average in-plane static dielectric constant taken for anisotropic materials. ¹ (Gmitra <i>et al.</i> , 2009), ² (Tabert and Nicol, 2013), ³ (Liu <i>et al.</i> , 2011), ⁴ (Kim, Hsu, Jia, Kim, Shi, Dresselhaus, Palacios, and Kong, Kim <i>et al.</i>), ⁵ (Hüser <i>et al.</i> , 2013), and ⁶ (Ramasubramaniam, 2012).	86

CHAPTER 1

INTRODUCTION

Layered materials when thinned down to their monolayer limit exhibit remarkable properties as a consequence of quantum effects and strong electron confinement. Due to the confinement of electrons in out-of-plane direction, physical properties of layered materials show strong enhancement. The real story of two dimensional (2D) monolayer form of materials begins with successful isolation of graphene (Novoselov *et al.*, 2004), 2D honeycomb structure of carbon atoms. Due to its extraordinary physical properties such as having low absorption ratio of 2.3% (Kuzmenko *et al.*, 2008; Nair *et al.*, 2008), exhibiting high electron mobility at room temperature (Novoselov *et al.*, 2004; Mayorov *et al.*, 2011)($2.5 \times 10^5 \text{ cm}^2 \text{V}^{-1} \text{s}^{-1}$), and high thermal conductivity (Chen *et al.*, 2008; Geim and Kim, 2008) (3000 WmK^{-1}). In addition, it has shown that graphene can have very high densities of electric current (Moser *et al.*, 2007) (million times higher than that of copper) and can be chemically functionalized for tuning its properties (Elias *et al.*, 2009; Loh *et al.*, 2010; Nair *et al.*, 2010). Beside all these properties, graphene is known to exhibit extreme mechanical properties with its very high Young modulus ($\sim 1 \text{ TPa}$) and intrinsic strength of 130 GPa (Lee *et al.*, 2008; Liu *et al.*, 2007). With all these extreme properties, graphene has opened up a new research of field in 2D monolayer materials.

Generally, mechanical properties of a crystalline solid can be controlled by characteristics of its pristine crystal lattice and structural defects like dislocations and grain boundaries contained in the structure (Lothe and Hirth, 1982). However, in the 2D limit defects can be absent in the non-deformed state due to nanoscale and free-surface effects. Therefore, such solids can exhibit superior strength values close to its ideal highest value. The elastic properties of graphene were first systematically investigated by Lee *et al.* in 2008 in a series of experiments (Lee *et al.*, 2008). In their experiment, graphene was mechanically deposited onto a substrate and applied load was achieved by a tip of Atomic Force Microscopy (AFM). It was reported by means of its stress-strain relation that graphene demonstrates both non-linear elastic and brittle fracture. In the elastic limit of graphene its Young modulus was observed to be 1 TPa. In addition, the fracture strength of graphene at its brittle point was found to be 130 GPa which is the largest value experienced ever. They also reported that although graphene is a stiff and brittle material, it can be easily bent over due to its low bending modulus. As mentioned above, graphene has the highest measured elastic modulus and tensile strength among all

natural materials which arise from the strong sp^2 C-C bonding in its structure. However, in nature many type of defects can exist in graphene as in other materials, and the mechanical properties of the crystal can be deformed upon these defects (Grantab *et al.*, 2010; Wei *et al.*, 2012; Warner *et al.*, 2012; Dettori *et al.*, 2012; Jing *et al.*, 2012). Grantab *et al.* has addressed this outstanding problem in mechanical properties of graphene by means of DFT and molecular dynamics (MD) calculations (Grantab *et al.*, 2010). They showed that graphene sheets having large-angle tilt boundaries with a high density of defects are as strong as the pristine material surprisingly. In addition, these graphene sheets can be much stronger than those having low-angle boundaries with fewer defects densities. It is seen that existence of high defect density may be able to conserve the mechanical characteristics of graphene. It was also reported that failure and ultimate strain values for graphene can be enhanced with grain boundary angle. Some time later, Wei *et al.* clearly explained the physical mechanism causing the weakening or enhancement of strength of graphene having grain boundaries (Wei *et al.*, 2012). They showed that the reason for tuning of strength of graphene is not just the density of defects, the arrangements of defects are also important. It was reported that the strengths of tilt grain boundaries increase as the square of their tilt angles if pentagon-heptagon defects are evenly spaced in the structure. This trend breaks down if pentagon-heptagon defects are not evenly distributed. Their findings are very important because pentagon-heptagon rings are one of the most common defects found in graphene. Young modulus of materials is an important elastic parameter describing mechanical characteristics of the structure. Behavior of Young modulus in defected graphene has been investigated by Jing *et al.* (Jing *et al.*, 2012) and it was shown that the vacancy and Stone Wales type defects reduce the value of Young modulus of graphene. However, the reconstruction of these defects can stabilize the Young modulus. In addition, a possible hydrogenation of vacancy defect sites will enhance the Young modulus while an opposite behavior is observed for hydrogenation of Stone Wales defect sites. Experimentally the existence of these defects and dislocations is directly related to synthesis techniques used for graphene. For example, in some studies it was observed that graphene synthesized by chemical vapor deposition (CVD) method has much lower Young modulus and tensile strength than those of exfoliated graphene (Ruiz-Vargas *et al.*, 2011; Lin *et al.*, 2013). The underlying mechanisms causing the decrease in these mechanical parameters were then explained in detail (Lee *et al.*, 2013; Tsen *et al.*, 2012; Yu *et al.*, 2011; Kim *et al.*, 2011). As a common result, it was reported that the transfer process is an important key for existing of ripples and defects which strongly affect the young modulus and ultimate strength of graphene. Lee *et al.* studied different types of transfer processes for CVD

graphene and found that adopting polydimethylsiloxane (PDMS) as the transfer medium instead of polymethyl methacrylate (PMMA) strongly enhances the value of 2D Young modulus of graphene (339 ± 17 N/m which very close to that of exfoliated graphene, 340 N/m) (Lee *et al.*, 2013).

As we mentioned above, defects, dislocations, and grain boundaries which may intrinsically exist in production of graphene are the main reasons for decreasing in values of mechanical parameters. Not only for defected graphene but also for a perfect sheet of graphene, it is an important issue to enhance its mechanical properties for use in various applications. In many studies, researchers tried to increase mechanical efficiency of graphene by external effects such as functionalization of its surfaces with various types of molecules and functional groups. Zhao *et al.* reported a significant enhancement of mechanical parameters of nanocomposites based on fully exfoliated graphene nanosheets and poly(vinyl alcohol) (PVA) (Zhao *et al.*, 2010). They showed that a significant improvement of tensile strength (150% increase) and a nearly 10 times increase in Young modulus which strongly depends on the density of graphene sheets included in nanocomposites (nearly at 1.8% volume of graphene addition). Xu *et al.* successfully prepared such nanocomposite material by using graphene oxide and reported a layered composite which is mechanically strong and ductile (Xu *et al.*, 2009). It is important to note that the brittle character of graphene was tuned to ductile behavior by functionalizing oxidized graphene. In another study Fang *et al.* reported an efficient method to functionalize graphene nanosheets with molecules that are covalently bonded to its surface (Fang *et al.*, 2009). It was shown that the resultant polystyrene nanocomposites with inclusion of 0.9% graphene nanosheets reveals an increase of 70% and 57% tensile strength and Young modulus, respectively.

Enhancing mechanical properties of graphene is not limited to its strength and Young modulus. In addition to these mechanical parameters, Poisson ratio takes an important place in field of engineering of graphene's mechanical properties. It is already known that graphene has a positive Poisson ratio value as usual materials. However, Jiang *et al.* shown that graphene can exhibit negative Poisson ratio which is robust and independent of its size and temperature (Jiang and Park, 2014). They showed that the nature of this negative Poisson ratio occurs due to the interplay between two intrinsic deformation pathways that are the bond stretching and angle bending interactions. In another study, Wan *et al.* investigated the auxetic (negative Poisson ratio material) behavior in graphene oxide paper which depends on the oxidation level (Wan *et al.*, 2017). They reported that the Poisson ratio is sufficiently tunable with oxidation level of graphene oxide paper. It

was found that when the graphene layer is fully oxidized, the Poisson ratio takes a value of -0.57. Grima *et al.* studied the effect of defects on Poisson ratio of graphene and found that the existence of vacancy defects can lead to auxetic behavior in graphene (Grima *et al.*, 2015).

Graphene can be explained in much more sentences with its extreme mechanical properties. Because of its extraordinary physical properties, graphene has opened a new research of field, searching of novel 2D monolayer materials. Although it has many excellent properties, the lack of a band gap in graphene limits its application especially in optoelectronic devices. Thus, following the successful isolation of graphene many other 2D monolayer materials such as hexagonal structures of III-V binary compounds (*h*-BN (Novoselov *et al.*, 2005; Zeng *et al.*, 2010; Song *et al.*, 2010) and *h*-AlN (Bacaksiz *et al.*, 2015; Tsipas *et al.*, 2013), monolayers of transition metal dichalcogenides (TMDs) (Gordon *et al.*, 2002; Wang *et al.*, 2012; Radisavljevic *et al.*, 2011; Lu *et al.*, 2014; Ramakrishna Matte *et al.*, 2010), monolayers of post-transition metal chalcogenides (PTMC) (Ga- and In-monochalcogenides) (Late *et al.*, 2012; Li *et al.*, 2014; Cai *et al.*, 2016; Huser *et al.*, 2013), and recently in-plane anisotropic monolayer materials (Re-dichalcogenides (Tongay *et al.*, 2014; Wolverson *et al.*, 2014), blackphosphorus (Li *et al.*, 2014; Liu *et al.*, 2014), and TiS₃ (Island *et al.*, 2014) were successfully brought into this material family.

Mechanical properties of 2D monolayer materials can generally be presented in terms of their in-plane stiffness, Poisson ratio, and ultimate strength. Evidently, the AFM indentation method which was used by Lee *et al.*, was shown to be applicable for other 2D materials beyond graphene. Bertolazzi *et al.* (Bertolazzi *et al.*, 2011a) measured the in-plane stiffness and breaking strength of monolayer MoS₂ by the same methodology of Lee *et al.*. They reported a value of 180 ± 60 N/m and 23 GPa for stiffness and breaking strength, respectively. The observed values are smaller than those of graphene which is expected because of the non-planar structure of monolayer MoS₂. Another report on the Young modulus of few layer MoS₂ was announced by Gomez *et al.* by performing a bending test experiment using tip of an AFM (Castellanos-Gomez *et al.*, 2012). They found a value of 0.33 ± 0.07 TPa for the Young modulus of few layer (down to 5 layers) suspended MoS₂. Another important finding is the high-elasticity of these suspended MoS₂ nanosheets. They reported that the suspended sheets are so tough that they can stand high deformations without breaking. Cooper *et al.* investigated the non-linear elastic properties of suspended monolayer MoS₂ both theoretically and experimentally (Cooper *et al.*, 2013). They found that in-plane Young modulus and intrinsic strength of mono-

layer MoS₂ are 130 and 16.5 N/m, respectively. It was also supported by experiment that mechanically exfoliated monolayer MoS₂ was subjected to a nanoindentation test by an AFM tip and an average value of 120 N/m was found for in-plane Young modulus which agrees well with the calculated DFT value. Different from those studies, Liu *et al.* investigated the in-plane Young modulus of CVD grown monolayer MoS₂ for the first time (Liu *et al.*, 2014). As reported for graphene, the experimental synthesis technique is an important key for the value of Young modulus in 2D monolayer materials. Thus, study of Liu *et al.* is significantly important for the understanding of rigidity of MoS₂. They reported a value of 170 N/m for in-plane Young modulus of MoS₂ which is about half that of graphene.

Since graphene and monolayer MoS₂ are in-plane isotropic materials, it is not possible to distinguish their direction-dependent mechanical properties. Thus, successful synthesis of monolayers having in-plane anisotropy has opened an important area in the applications of these materials. Monolayer black phosphorus (BP) is an important example to these in-plane anisotropic monolayers. Due to its puckered structure, it is highly anisotropic in different chiralities. As a first experimental observation, Tao *et al.* identified the lattice orientations in 2D few layer BP to probe the anisotropic mechanical properties of the material by using AFM bending method (Tao *et al.*, 2015). The measured Young modulus of few layer BP was reported to be 58.6 ± 11.7 and 27.2 ± 4.1 GPa in zigzag and armchair directions, respectively. This high in-plane anisotropy was also observed for the breaking stress of few layer BP as 4.79 ± 1.43 and 2.31 ± 0.71 GPa in zigzag and armchair directions, respectively. As seen from the given values, breaking strengths are almost compatible with Young modulus values. Apart from this experimental study, Wang *et al.* theoretically investigated the effect of uniaxial strain on the mechanical properties of BP and showed that uniaxial strain efficiently enhances the anisotropy in the structure (Wang *et al.*, 2015). It was shown that the Poisson ratio of BP vary non-monotonically with the direction of applied uniaxial strain while the Young modulus vary monotonically from zigzag direction to armchair direction. Because of its low in-plane Young modulus values BP is not a stiff material and with its low fracture strength its applications in mechanical devices is limited. The physical mechanism behind having such low mechanical parameters was demonstrated by Liu *et al.* (Liu *et al.*, 2016) It was showed that the fracture of BP under uniaxial strain along armchair direction is caused by a break in the interlayer bond angles while it is attributed to the break in both intra-layer angles and bonds for the uniaxial strain along zigzag direction. Understanding of such phenomenon could be important for enhancing the mechanical constants of BP. In addition to Young modulus and fracture

strain of BP, it is a special monolayer material with its negative Poisson ratio. Jiang *et al.* reported that negative Poisson ratio in monolayer BP occurs intrinsically (Jiang and Park, 2014). They showed theoretically that in contrast to bulk auxetic materials which are mostly hand-made, auxetic behavior of monolayer BP naturally occurs due to its puckered crystal structure. It was reported that the auxetic behavior is special to out-of-plane direction in monolayer BP. Recently, Du *et al.* investigated the anisotropic strain responses of few-layer BP films to uniaxial tensile and compressive strains experimentally (Du *et al.*, 2016). They showed the existence of negative Poisson ratio by examining the Raman evolution of uniaxially strained BP. In addition, by examining DFT based calculations they reported that this interlayer auxetic behavior occurs under armchair strain.

Monolayers of ReS₂ and ReSe₂ are two important examples for in-plane anisotropic materials. Due to their distorted 1T (1T') structure, strong anisotropy in their electronic, optical, and transport properties were reported (Liu *et al.*, 2015; Jariwala *et al.*, 2016; Hafeez *et al.*, 2016). However, studies on mechanical properties of these distorted monolayer TMDs are missing when compared to those for BP. In one of those studies Yu *et al.* investigated both in-plane and out-of-plane elastic modulus (Young modulus) for monolayer ReS₂ and reported that for the directions along Re₄ clusters and the direction along the line having 120 degree with Re₄ clusters the Young modulus is isotropic with a value of 142 N/m while it is very high along out-of-plane direction (352 N/m) (Yu *et al.*, 2011). It should be noted that strong in-plane anisotropy is missing in mechanical constants for the chosen directions. In our very recent study, we investigated the mechanical properties of monolayer ReS₂ and its fully hydrogenated crystal structure (Yagmurcukardes *et al.*, 2017). Our results are mainly consistent with those reported by Yu *et al.* that for two directions, one along Re₄ clusters and another is perpendicular to that, the in-plane anisotropy is very small for Young modulus along those directions (we found 166 and 159 N/m values). However, we reported that a possible full hydrogenation of monolayer ReS₂ results in strong mechanical anisotropy. Thus, functionalization is a way for tuning of the mechanical properties of monolayer ReS₂.

CHAPTER 2

METHODOLOGY

2.1. Many-Electron Systems

Interacting many-electron systems generate some of the most outstanding challenges in quantum mechanics for researchers to understand such systems for many applications. However, due to the difficulty of solving such systems using quantum mechanical wave functions, density functional theory (DFT) has become a useful and popular approach.

DFT is the most popular and powerful quantum mechanical approach for the determination of ground state; electronic, magnetic, optical, and mechanical properties of interacting many-electron systems such as solids and molecules used in physics, chemistry, and materials science. Since the wave function is not a real observable in quantum mechanics, describing all physical ground state properties of materials in terms of an electronic density makes DFT a powerful and most used methodology due to its ability for producing very accurate results at low cost.

A quantum mechanical wave function contains all the information about a physical system. The mathematical expression for such a wave function may be represented by the time-independent non-relativistic Schrodinger equation

$$\hat{H}\Psi = E\Psi \quad (2.1)$$

where the operator \hat{H} is the energy operator known as the Hamiltonian and the E is the corresponding eigenvalue for the Hamiltonian operator. The solution of the Eq. 2.1 is the wavefunction Ψ which are the eigenfunctions of the Schrodinger equation. In usual model of a matter, the Schödinger equation should be written for a many-electron system's Hamiltonian. When a N -body system is assumed, it is very difficult to solve the Eq. 2.1 without considering any approximations.

For such a system containing M nuclei and N electrons the Hamiltonian operator contains the terms for all possible interactions between electrons and nuclei. As a result of this form of \hat{H} , the wavefunction of the system will be the function of spatial coordinates of nuclei ($\{R_A\}$, $A=1,\dots,M$) and that of electrons ($\{r_i\}$, $i=1,\dots,N$). The \hat{H} operator has the

general form for N-body system is

$$\hat{H} = -\sum_{i=1}^N \frac{\nabla_i^2}{2} - \sum_{A=1}^M \frac{\nabla_A^2}{2M_A} + \sum_{i=1}^N \sum_{j>i}^N \frac{1}{|r_i - r_j|} + \sum_{A=1}^M \sum_{B>A}^M \frac{Z_A Z_B}{|R_A - R_B|} - \sum_{i=1}^N \sum_{A=1}^M \frac{Z_A}{|r_i - R_A|} \quad (2.2)$$

This Hamiltonian operator contains all the terms describing all possible interactions in an N -electron quantum mechanical system. First two terms are the kinetic energy terms for electrons and nuclei, respectively. M_A in the second term is the ratio of the mass of nucleus to that of an electron, and Z_A is the atomic number of the nucleus A . The ∇_i^2 and ∇_A^2 are Laplacian operators in the coordinates of electron and nucleus, respectively. The third and fourth terms are the Coulomb repulsion terms between electrons and nuclei, respectively. Finally, the last term is the Coulombic interaction between an electron and nucleus. Although, it is written easily by hand, the solution of Schrodinger equation for this Hamiltonian seems impossible. Thus, many approximations were suggested to simplify the solution for this \hat{H}

2.1.1. Born-Oppenheimer Approximation

Born-Oppenheimer approximation, which was developed by Max Born and J. Robert Oppenheimer in 1927 (Born and Oppenheimer, 1927), fundamentally assumes that nuclei are much heavier than the electrons in mass. Through this simple assumption, nuclei can be treated as static, classical particles with respect to electrons. So, the kinetic term of nuclei in Eq. 2.2 can be omitted while the fourth term becomes a constant due to the fixed configuration of nuclei. With remaining three terms, the Hamiltonian takes the form known as electronic Hamiltonian,

$$\hat{H}_e = -\sum_{i=1}^N \frac{\nabla_i^2}{2} + \sum_{i=1}^N \sum_{j>i}^N \frac{1}{|r_i - r_j|} - \sum_{i=1}^N \sum_{A=1}^M \frac{Z_A}{|r_i - R_A|} \quad (2.3)$$

After this simple assumption, the wavefunction which is solution to this Hamiltonian becomes only the function of electron position r_i . The corresponding Schrodinger equation takes the form,

$$\hat{H}_e \Psi_e(\{r_i\}) = E_e \Psi_e(\{r_i\}) \quad (2.4)$$

Under Born-Oppenheimer approximation, solution of Eq. 2.4 seems to be more simple than its most general form. However, although it seems to be a simple form, the electron-

electron interaction term in Eq. 2.3 since the motion of electrons is correlated. Thus, the instantaneous coordinates of each electron should be taken into account which essentially requires 3^N variables for N -electron system. For the solution of Schrodinger equation of N -interacting electrons, different approximations were introduced. The main purpose of those approximations is to map N -electron Schrodinger equation to effective one-electron Schrodinger equation. One of those approximation methods is density functional theory (DFT) in which the electron density is considered to be a central quantity.

2.1.2. Thomas-Fermi Model

The idea that the electronic energy can be expressed in terms of the electron density was first suggested by Thomas and Fermi in 1920s (Thomas, 1927; Fermi, 1927). In the Thomas-Fermi theory, the electron-nucleus and electron-electron interactions are assumed to exist classically and only the kinetic energy of the electrons is approximated as an explicit functional of the electron density. It assumes non-interacting electrons in a homogeneous electron density. The kinetic energy term is written in as a functional of electron density as,

$$T[n] = C_F \int n^{5/3}(r) dr \quad (2.5)$$

where the Fermi coefficient C_F is equal to 2.781 in atomic units. Adding two interaction terms, electron-electron and electron-nucleus, the total energy of the system in terms of electron density takes the form,

$$E[n] = C_F \int n^{5/3}(r) dr - Z \int \frac{n(r)}{r} dr + \frac{1}{2} \int \int \frac{n(r_1)n(r_2)}{|r_1 - r_2|} dr_1 dr_2 \quad (2.6)$$

where the second and third terms are the electron-nucleus and electron-electron interaction terms, respectively. Then, once one knows this total energy functional, it is possible to calculate ground state energy of the system by minimizing the functional, $E[n]$, for all possible electron density, $n(r)$, which should satisfies,

$$N = \int n(r) d^3r \quad (2.7)$$

The main goal of the Thomas-Fermi model is not how well the ground state energy is performed but rather is the illustration that the total energy can be investigated using electron density.

2.1.3. Density Functional Theory

In order to simplify N -electron Schrodinger equation into one-electron like equation, electron density, $n(\mathbf{r})$, is considered in DFT. One the advantages of using electron density over the wavefunction is the reduced dimensionality of the problem. Regardless of the number of total electrons interacting in the system, considering the electron density reduces the dimension from 3^N to 3 because $n(\mathbf{r})$ has always three degrees of freedom. This reduction in total degree of freedom enables DFT to readily be applied to much larger system.

First of all, the electron density is defined as,

$$n(\mathbf{r}) = N \int \dots \int |\Psi(r_1, r_2, \dots, r_N)|^2 dr_1 dr_2 \dots dr_{N-1} \quad (2.8)$$

where $n(\mathbf{r})$ determines the probability of finding any of the N electrons while other $N-1$ electrons are positioned arbitrarily. In addition, $\Psi(r_1, r_2, \dots, r_N)$ is the solution of the Schrodinger equation and is a function of position of each electrons. Now we discuss some models presented in DFT on electron density.

2.1.3.1. Hohenberg-Kohn Theorems

After Thomas-Fermi model was presented, in 1964 Hohenberg and Kohn formulated the DFT as an exact theory of many-body systems which allows one to express the electronic Hamiltonian as a functional of electron density, $n(\mathbf{r})$ (Hohenberg and Kohn, 1964). In this model two main theorems exist: (i) there is a one-to-one correspondence between an external potential $V_{ext}(\mathbf{r})$ and electron density $n(\mathbf{r})$, and (ii) the ground state electron density $n_0(\mathbf{r})$ can be calculated by means of a variational principle. Then, for a given $V_{ext}(\mathbf{r})$ the total energy functional can be written as,

$$E[n] = T[n] + V_{ne}[n] + V_{ee}[n] = \int n(\mathbf{r})V_{ext}(\mathbf{r})d\mathbf{r} + F_{HK}[n] \quad (2.9)$$

where $F_{HK}[n]$ is a universal functional of $n(\mathbf{r})$ and is independent of any external potential, $V_{ext}(\mathbf{r})$. In this theory, once we know the the ground state electron density $n_0(\mathbf{r})$, the external potential $V_{ext}(\mathbf{r})$ can be uniquely determined. In addition, if $F_{HK}[n]$ is a known universal functional of electron density $n(\mathbf{r})$, then for any $V_{ext}(\mathbf{r})$ the exact ground state energy of the system is the global minimum of this functional with exact ground state density, $n_0(\mathbf{r})$.

2.1.3.2. The Kohn-Sham Equations

One year later, in 1965, Kohn and Sham realized a model which transforms DFT into a practical electronic structure theory (Kohn and Sham, 1965). They recognized that the Thomas-Fermi model fails mainly in describing the kinetic energy of the system. The energy functional given in Eq. 2.10 now takes the form,

$$E[n] = \int n(r)V_{ext}(r)dr + F_{HK}[n] = \int n(r)V_{ext}(r)dr + T[n] + E^{Hartree}[n] + E_{xc}[n] \quad (2.10)$$

where the universal functional, $F_{HK}[n]$, is written as the sum of kinetic energy of non-interacting electrons, $T[n]$, Hartree energy, $E^{Hartree}$, and exchange and correlation energy, E_{xc} . Here, the important step is to define an effective potential which is written as,

$$V^{eff} = \frac{\delta\{\int n(r)V_{ext}(r)dr + E^{Hartree}[n] + E_{xc}[n]\}}{\delta n(r)} \quad (2.11)$$

which results in the form,

$$V^{eff} = V_{ext}(r) + \int \frac{n(r')}{|r-r'|}dr' + V_{xc}(r) \quad (2.12)$$

where $V_{xc}(r)$ is the exchange-correlation potential derived from the exchange-correlation energy. Using this form of effective potential, the Schrodinger equation in Kohn-Sham DFT takes the form of one-electron like equation as,

$$\left[-\frac{1}{2}\nabla^2 + V^{eff} \right] \phi_i = E_i\phi_i \quad (2.13)$$

where the eigenfunctions, ϕ_i , are known as the Kohn-Sham one-electron orbitals which result in the electron density,

$$n(r) = \sum_{i=1}^N |\phi_i|^2 \quad (2.14)$$

Due to the form of Eq. 2.14, the effective potential, V^{eff} , depends on the density, $n(r)$. Thus, the Kohn-Sham equation should be solved by the following way: (i) begin with an initial guess of the electron density, (ii) then construct the effective potential, V^{eff} , by the knowledge of electron density, (iii) calculate the corresponding Kohn-Sham orbitals, ϕ_i , and (iv) calculate the new electron density corresponding to these orbitals and compare with the initial one. Once the convergence is achieved, then the total energy can

be calculated in terms of the final electron density. However, although the final electron density is known, the exchange-correlation energy is still missing.

2.1.3.3. The Types of Exchange-Correlation Functionals

The exchange and correlation energy of a many-electron system is supposed to be a key quantity in DFT. Exchange energy is generally defined in the view of Pauli exclusion principle because in such systems we deal with electrons which are known to be fermions. Due to this principle, when two electrons interact their total wave function will be anti-symmetric which give rise to an exchange energy. However, correlation energy is generally defined as the difference between true total energy of a quantum mechanical system and its Hartree energy.

In order to complete the Khon-Sham equations, one should exactly know the form of E_{xc} . For this reason, some sort of approximations for this term have been developed. We now introduce only the most common types of these functionals which are widely used in DFT based calculations.

Local Density Approximation(LDA) :

Within this approach, the system is divided into infinitesimal volumes each of which contains constant electron density. The exchange-correlation energy for each piece is assumed to be the energy of uniform electron gas of the density. The exchange-correlation energy of LDA can be written as (Ceperley and Alder, 1980),

$$E_{xc}^{LDA}[n] = \int n(r)\epsilon_{xc}^{unif}[n]dr \quad (2.15)$$

where ϵ_{xc}^{unif} is known to be the exchange-correlation energy per electron. LDA is known to be valid for slowly varying electron densities. In addition, it is experienced that LDA works well especially for metallic systems. The cohesive energies of physical systems are known to be overestimated within LDA while lattice constants are underestimated.

Generalized Gradient Approximation(GGA) :

It was realized that the local uniform density is not a suitable approximation for rapidly varying electron densities, thus, the gradient of the electron density, $\nabla n(r)$, should also be included. For the total energy functional in GGA, a general functional of both electron density and its gradient should be included in it (Perdew *et al.*, 1996a),

$$E_{xc}^{GGA}[n] = \int f^{GGA}(n(r), \nabla n(r)) dr \quad (2.16)$$

These functionals are known as semi-local functionals due to their dependence on the gradient of the electron density. It was experienced by many researchers that GGA functionals can yield better results for the geometry and ground state energy calculations when compared with LDA.

2.2. Mechanical Properties of Materials

Mechanical properties of materials have great significance due to giving information about the stability of their structure under applied external forces. This information for a material exactly depends on the structure of the material that is interatomic forces which resist any structural change determine the behavior of the material. The changes in a material and the overall macroscopic behavior are tested in experiments and described in terms of the applied force per unit area (stress) and the displacement per unit distance (strain).

2.2.1. Elastic Constants

One of the most common mechanical stress-strain tests is performed in tension. Tensile test (or tension test) is an important experimental step to predict and analyze the mechanical behavior of a material under applied load. Tensile test is very important in determining the strength of a material, its ductility and the mechanical characteristics of the material in terms of the elastic constants (Young modulus, Poisson ratio, Bulk modulus etc...) These elastic constants for a material can be obtained from the measurements of stress under applied strain in the linear elastic region. When a material is loaded only in the elastic region, it is able to restore its original shape with no permanent change after the applied load is removed. Thus, the elastic property of a material can be emphasized as the reversible future of the deformation process.

When a tensile stress is imposed on a material, for low values of the applied loads stress and strain are related to each other linearly. This low-load region is known as the elastic region for metals and brittle materials. However, for rubber-like materials, which are known to be ductile, the stress-strain relation does not show a linear behavior or it may exist for very very small applied loads. For most of the materials elastic behavior

is observed and the stress-strain are related through the Hooke's Law which relates them linearly.

2.2.1.1. Young Modulus

The relation between applied load (stress) and strain in the elastic region can be expressed by

$$\sigma = E\varepsilon \quad (2.17)$$

where σ is the applied load and ε is the change in the dimension of the material along the direction of the applied load. Here E is known as the constant of proportionality which is also known as 'Young's Modulus'. This constant can take different forms depending on the direction and type of the applied load. The Young's modulus or the modulus of elasticity has a SI unit of GPa. As given in Eq.2.17, the slope of a linear segment of stress-strain relation will correspond to E. This modulus, can also be thought as stiffness or the resistance of the material to elastic deformation. In fact when elastic modulus is considered on the atomic scale, the strain can be thought as the small changes in the interatomic spacing and also the stretching of interatomic bonds. Then, the measure of the modulus of elasticity will give the material's resistance to separation of adjacent atoms. Values of the modulus of elasticity are different for different types of materials. The reason is exactly due to the different types of atomic bonding in materials.

2.2.1.2. Poisson Ratio

Poisson ratio is another important elastic constant which describes the behavior of a material to applied load along the unloaded directions. One may define this quantity as the the ratio of transverse contraction strain to longitudinal extension strain in the direction of stretching load that is;

$$\nu = -\frac{\varepsilon_{trans.}}{\varepsilon_{long.}} \quad (2.18)$$

As given in the definition of Poisson ratio, it is an important quantity for materials to identify the compressive(tensile) strains along unloaded directions when the material is stretched(compressed) uniaxially. For most of the materials, the strains along unloaded

directions will have opposite sign with respect to loaded direction, thus, the minus sign is included in the formula to have a positive value for Poisson ratio. Generally, most of the materials become narrower when they are stretched uniaxially. The reason is that, most materials resist to a change in their volume (naturally result of their bulk modulus) more than they resist to a change in shape (result of their shear modulus). Structurally, the reason of the having positive Poisson ratio is the realignment of interatomic bonds upon deformation.

As we mentioned not the all of them but most of materials have positive Poisson ratio that means materials with negative Poisson ratio exist in real world which occur naturally or are hand-made. In contrast to positive Poisson ratio materials, materials with negative Poisson ratio tend to extend in a direction when stretched along perpendicular directions. These materials are known as the 'Auxetics'. With all the auxetic materials discovered so far, the underlying mechanism is explained by the intrinsic geometry of the material. These materials can have better physical properties when compared to those for positive Poisson ratio materials.

2.2.2. Elastic Constants in 2D Limit

In previous sections we defined two important elastic constants, E and ν , for bulk materials. When dimensional reduction is achieved, these elastic constant should be re-defined for in case of two dimensional (2D) materials. In this section, we define shortly these two constants and present our methodology for the calculations of them at the atomic scale.

2.2.2.1. In-plane Stiffness

The word, modulus of elasticity, can be renamed as in-plane stiffness, C , when 2D limit is assumed. In the 2D limit, since materials have no periodic boundary condition along the out-of-plane direction, modulus of elasticity (in-plane stiffness) should be related by the in-plane stress and strain. Thus, the Eq. 2.18 should be rewritten in the constraint form as;

$$\sigma_{xx} = C_{xx}\varepsilon_{xx} \quad (2.19)$$

$$\sigma_{yy} = C_{yy}\varepsilon_{yy}$$

where the directions xx and yy indicate special directions in the 2D crystal structure. For example, in a hexagonal crystal structure these directions may demonstrate zigzag and armchair directions. For isotropic materials, values of C in any direction will have the same value. This occurs because of the interatomic bonding symmetry of the crystal structure. However, for anisotropic 2D materials, the observation of in-plane stiffness along different directions will give different results. This means that the material's resistance to applied load will not be unique along all directions which may have advantages in its applications in nanotechnology.

The calculation of C in the atomic limit can be done through the relation of strain energy and applied strain. Strain energy in a material is defined as the change in total energy of the crystal with applied strain. Since we calculate these elastic constants in the linear elastic region, the strain energy should obey the equation;

$$E_S = c_1\varepsilon_{xx}^2 + c_2\varepsilon_{yy}^2 + c_3\varepsilon_{xy}^2 \quad (2.20)$$

where E_S is strain energy which is defined as the total energy difference between strained and relaxed geometries. Once the coefficients c_i are calculated, the in-plane stiffness along any special direction can be calculated by the formula;

$$C_x = (1/A_0)(2c_2 - c_3^2/2c_1) \quad (2.21)$$

$$C_y = (1/A_0)(2c_1 - c_3^2/2c_2)$$

where A_0 is the strain-free area of the crystal structure.

Calculation of in-plane stiffness is also possible from the knowledge of elastic parameters which are calculated by elasticity tensor. As we mentioned in-plane stiffness represents the relation between stress and strain in the linear elastic region. The elasticity tensor which relates the applied load (stress) to the strain tensor has dimension of 6×6

given by the form;

$$\begin{bmatrix} C_{1111} & C_{1122} & C_{1133} & C_{1123} & C_{1131} & C_{1112} \\ C_{2211} & C_{2222} & C_{2233} & C_{2223} & C_{2231} & C_{2212} \\ C_{3311} & C_{3322} & C_{3333} & C_{3323} & C_{3331} & C_{3312} \\ C_{2311} & C_{2322} & C_{2333} & C_{2323} & C_{2331} & C_{2312} \\ C_{3111} & C_{3122} & C_{3133} & C_{3123} & C_{3131} & C_{3112} \\ C_{1211} & C_{1222} & C_{1233} & C_{1223} & C_{1231} & C_{1212} \end{bmatrix} \quad (2.22)$$

where C_{ijkl} 's are elastic constants which have some symmetry properties such as; $C_{ijkl} = C_{jikl}$, $C_{ijkl} = C_{ijlk}$, and $C_{ijkl} = C_{klij}$. With all these symmetry considerations, the number of independent constants reduces to 21 in this 36-element tensor. However, this number 21 is the maximum number of independent elements. Depending on the symmetry of crystal structure, it changes between 3 and 21.

For isotropic materials, the form of the elasticity tensor takes the form in Voigt notation as;

$$\begin{bmatrix} C_{11} & C_{12} & C_{12} & 0 & 0 & 0 \\ C_{12} & C_{11} & C_{12} & 0 & 0 & 0 \\ C_{12} & C_{12} & C_{11} & 0 & 0 & 0 \\ 0 & 0 & 0 & C_{33} & 0 & 0 \\ 0 & 0 & 0 & 0 & C_{33} & 0 \\ 0 & 0 & 0 & 0 & 0 & C_{33} \end{bmatrix} \quad (2.23)$$

where C_{33} is related to C_{11} and C_{12} by the relation; $C_{33} = \frac{C_{11}-C_{12}}{2}$. This notation allows one to relate mechanical constants each other through these elastic constants. For example, once the elements C_{ij} are known the Young modulus and Poisson ratio can be related to each other by the formula;

$$C_{11} = \frac{E(1-\nu)}{(1+\nu)(1-2\nu)} \quad (2.24)$$

$$C_{12} = \frac{E\nu}{(1+\nu)(1-2\nu)}$$

where E is the modulus of elasticity (Young modulus) and ν is the Poisson ratio. Three dimensional modulus of elasticity, E, can be related to its 2D counterpart, C, by considering the effective thickness of a 2D monolayer material. The effective thickness, h_e , is generally assumed to be the thickness of the layer itself plus the interlayer spacing in its bulk form. Then the in-plane stiffness and E are related by the formula;

$$C = Eh_e \quad (2.25)$$

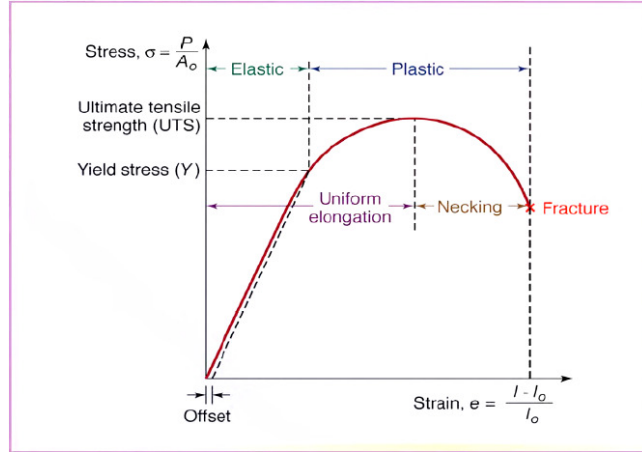


Figure 2.1. A general stress-strain curve demonstrating elastic and plastic regions for a material including defects or dislocations which are the generators of plastic region.

By using the Eqs. 2.24 and 2.25, one may able to rewrite C in terms of elastic constants C_{ij} as;

$$C = h_e C_{11} \left[1 - \left(\frac{C_{11}}{C_{12}} \right)^2 \right] \quad (2.26)$$

This elasticity tensor can be directly calculated by using density functional theory (DFT) based first principles calculations as an output. Thus, it is possible to calculate the in-plane stiffness in two different ways as mentioned here.

As in the case of C , it is also possible to calculate Poisson ratio in terms of the elastic constants found from the elasticity tensor. Using the elements C_{ij} one can calculate the Poisson ratio by the formula;

$$\nu = \frac{C_{12}}{C_{11}} \quad (2.27)$$

When the case of anisotropic materials is considered, the elastic constant in Eq. 2.27 can be changed to find the direction-dependent Poisson ratio of the material. For example if one uses C_{22} in Eq. 2.27, then the Poisson ratio along the direction-2 can be calculated.

Up to now we have defined the elastic mechanical constants and summarized the calculation methods by using DFT-based calculations. In the next section, we explain other mechanical parameters such as ultimate strength by defining the stress-strain relation curve.

2.2.3. Stress-Strain Relation

The stress-strain curve demonstrates the relationship between the magnitude of applied load and the resulting strain on a material. As we discussed in previous sections, for most of the materials this curve has a linear-elastic region in which the deformations in the material are reversible. However, this is true for the harmonic region in which the energy of the system is a quadratic function of the applied load. For higher values of stress, this total energy-strain relation can take different forms and non-reversible deformations can occur in the material. In order to figure out these behaviors, one should apply loads up to high values at which the material fractures.

A stress-strain curve can display different types of regions such as linear-elastic, uniform plastic or nonuniform plastic regions depending on the type of the material. Generally the term plastic region or plastic deformation is associated with metal crystal structures because it is mostly caused by dislocations. Thus, for a 2D monolayer crystal structure it is meaningful to name the plastic region as non-linear elastic region. At non-linear elastic region, the applied loads are high and the deformations are non-reversible. This occurs because at high values of applied load, some atoms in the structure may move to new places resulting in structural phase change. This region is important at the point that other mechanical properties of the material such as its brittleness or ductility, ultimate strength, and fracture point can be found from the stress-strain curve.

Firstly, from the slope of the curve of linear-elastic region one may determine the brittleness of a material if it suddenly breaks after linear-elastic region. This type of materials do not experience a plastic or non-linear elastic deformation. In contrast, a ductile material could experience plastic deformation before it fractures. Such materials experience structural changes before they break. In addition, these materials can resist to higher values of applied load when compared with brittle materials.

In the case of a perfect 2D monolayer materials (with no defects or dislocations), we can not talk about a plastic deformation which is driven by defects or dislocations. Instead, for every 2D material one can define non-linear elastic region in which non-reversible structural deformations occur before the fracture of the structure. When the applied load is increased, there will exist a maximum stress point which is defined as the ultimate strength of the material and the strain value for this point is known as the ultimate strain. In addition, a fracture strain can be defined as the strain value at which the material breaks.

In the case of our methodology, we check these mechanical behaviors by applying

high values of strain on the crystal structure. This can be done uniaxially and biaxially to determine the degree of anisotropy in the material. In order to get true stress takes place in the structure, we divide the total stress by the effective thickness, h_e , of the monolayer crystal. Ultimate strength is an important output for a material to know its ability be performed in applications. At the atomic scale, all of these mechanical constants and parameters are associated with type of interatomic bonding in the crystal structure. Thus, monolayer materials such as graphene which has strong C-C bonds, will have very high values of ultimate strength.

In 2D ultra-thin materials, stress-strain curve can demonstrate general, expected features and the material can seem to be structurally undeformed before it fractures. However, it is important to check the dynamical stability of the material especially for the strain values which are smaller than the ultimate strain. This is needed because a material, for example graphene, can preserve its crystal structure whether reversible or non-reversible deformations occur. However, this does not mean that it is still dynamically stable. The phonon instability can occur before the material reaches the ultimate strength point. This means, the crystal structure is not deformed but it is not dynamically stable any more. At some finite wave vectors, there will exist acoustic phonon modes with imaginary eigenvalues. For 2D monolayer materials, this acoustic phonon branch is generally the flexural one which describes the out-of-plane motion of individual atoms. This can be an expected feature because 2D monolayer materials have no boundary condition along the out-of-plane direction.

2.3. Theory of Phonons

The dynamical stability of materials whether under tensile test or at equilibrium can be checked by the calculation of the materials' phonon-band dispersion through Brillouin Zone. As a theory, matter is known to be composed of atoms vibrating around a certain equilibrium position which is determined by positions of neighboring atoms obeying the Hooke's Law. Due to this law, restoring forces that the atoms feel when they are displaced from their equilibrium position occur to describe these vibrations.

In this section of the thesis, we present the formalism for the calculation of phonon-band dispersion in harmonic approximation where the magnitude of the restoring force is related linearly to the magnitude of displacement. Thus, in order to determine the phonon-band dispersion of a material, the variation of restoring forces with displacements of atoms in a crystal should be known.

Apart from the general theory of phonons, here we present our methodology used in DFT calculations. As mentioned above, to get the phonon dispersions for a material, one should obtain the force constants as a matrix by displacing atoms. In order to achieve this, the small displacement method is used. In this methodology, firstly we need to consider a sufficiently large supercell for the crystal and then each of the atoms in the supercell should be displaced along the cartesian coordinates. The amount of displacement should be taken to be suitable for which the harmonic motion is satisfied. In addition, the use of symmetries in the crystal can reduce the number of displacements. For each of these displacements, the resulting Hellmann-Feynman forces are calculated and the dynamical matrix is constructed. Let us start with the potential energy function of the crystal at low temperature given by,

$$U_{harm} = E_{eq} + \frac{1}{2} \sum_{l s \alpha, l' t \beta} \Phi_{l s \alpha, l' t \beta} u_{l s \alpha} u_{l' t \beta} \quad (2.28)$$

where E_{eq} is the energy of the crystal at equilibrium positions of the ions while $u_{l s}$ denotes the displacement of the atom s in the unit cell l along cartesian directions α or β . The term $\Phi_{l s \alpha, l' t \beta}$ represents the force-constant matrix which is the second derivative of the harmonic potential energy with respect to the displacements. When the harmonic energy given in Eq. 2.28 is differentiated, one can find the relation between the forces on each atom, $F_{l s}$, and the displacements, $u_{l s}$, which is expected to be related linearly as,

$$F_{l s \alpha} = - \sum_{l' t \beta} \Phi_{l s \alpha, l' t \beta} u_{l' t \beta} \quad (2.29)$$

Once we know the force constant matrix, $\Phi_{l s \alpha, l' t \beta}$, then we can define the dynamical matrix as,

$$D_{s \alpha, t \beta} = \frac{1}{\sqrt{M_s M_t}} \sum_l e^{i \mathbf{q} \cdot (\mathbf{R}_{l' t \beta} - \mathbf{R}_{l s \alpha})} \Phi_{l s \alpha, l' t \beta} \quad (2.30)$$

where M_s and M_t are the masses of the s^{th} and t^{th} atoms. The term on the exponential function, $\mathbf{R}_{l' t \beta} - \mathbf{R}_{l s \alpha}$, represents the distortion of the atoms in the cartesian components α and β .

Once this matrix is found, one may able to solve the eigenvalue equation of the matrix. The eigenvalues of dynamical matrix give the phonon frequencies of each phonon branch for the crystal at any wave vector, \mathbf{q} . The total number of phonon branches is nothing but the total number of degree of freedom for the crystal. The size of the dynamical matrix is also determined by the number of these phonon branches. For a crystal structure containing N -atoms in its primitive unitcell, there will be found $3N$ phonon branches

of which are acoustic and $3N - 3$ are optical branches. The acoustic branches describe the motion of the individual atoms that move in-phase. For an optical phonon branch, however, the atoms move out-of-phase. Throughout this thesis, we have used the PHON code (Alfè, 2009), a free software, to calculate the phonon dispersion of a material. This code uses the Hellmann-Feynman forces calculated by the software Vienna *Ab-initio* Simulation Package (VASP) (Kresse and Furthmuller, 1996a) which is based on DFT.

2.3.1. Raman Spectrum

Raman spectroscopy is an experimental tool which provides information about atomic vibrations in a material that can be used to characterize the sample. In addition, the chemical structure, phase, and crystallinity of the material can be identified. In the Raman technique, a monochromatic light is incident on the sample and the scattered light is detected by the experimental setup. During the experiment, both elastic and inelastic scattering of light is detected. The majority of light scatters with the same frequency as the incoming light which is known as Rayleigh or elastic scattering. Only very small amount of the scattered light in energy, $10^{-5}\%$ of the incident light intensity, is shifted due to the interactions between the incident electromagnetic waves and the vibrational energy levels of the atoms in the material. The process leading to this inelastic scattering is termed the Raman effect. Raman scattering can occur with a change in vibrational, rotational or electronic energy of atoms in the sample. Chemists are concerned primarily with the vibrational Raman effect to characterize the structure, phase, and composition of the material. The energy difference between the incident photon and the Raman scattered photon is equal to the energy of a vibration of the scattering atoms. A plot of such energy difference figures out the Raman spectrum for the material.

In the view of quantum mechanical description, the vibrating molecule is excited to a virtual state. In Rayleigh scattering, the vibrating molecule returns to its ground state with no loss of energy. The intensity of such scattering is very high when compared to that of Raman scattering. In the plot of Raman spectrum, the Rayleigh intensities occur at zero frequency difference since the incident light is scattered with its original frequency. However, in Raman scattering the vibrating molecule returns to an excited state which is known as Stokes Raman scattering. If the vibrating molecule is initially in an excited state and returns to its ground state after scattering, this process is known as the Anti-Stokes Raman scattering. Although, Stokes and Anti-Stokes Raman scattering have the same intensities, scientists analyze and report the Stokes one since it exist with positive

energies in the Raman spectrum.

2.3.1.1. Theory of Raman Activity

In order to calculate the Raman activity of a vibrational mode, we should start by fundamental explanation of the intensity. Intensity of an output from a physical source is ratio of the average power to the area where the scattering rate is observed.

$$I = \frac{P}{A} \quad (2.31)$$

where P is the average Power radiated from the source and A is the area. As we mentioned in the previous section, in a Raman spectroscopy experiment an incident light interacts with vibrating atoms in the sample and scatters inelastically in Raman effect. As we know from classical electrodynamics, an oscillating dipole radiates with total average power P (watts) given by

$$P = \frac{4\pi^3\nu_0^4|\mu|^2}{3\epsilon_0c^3} \quad (2.32)$$

Then quantum mechanically the intensity of a transition from state $|\nu\rangle$ to $\langle\nu'|\nu\rangle$,

$$I = \frac{4\pi^3\nu_0^4}{3A\epsilon_0c^3} \langle\nu'|\mu^2|\nu\rangle \quad (2.33)$$

where ν_0 is the frequency of the incident light, c is the velocity of light, and μ is the electric dipole moment of the oscillating dipole which is related to incident electric field by,

$$\mu = \alpha E \quad (2.34)$$

with α being the polarizability of the matter. Here the induced dipole moment in the oscillating molecule is caused by the incident oscillating electric field E . For an incident light of frequency ν_0 , the electric field component oscillates in the form,

$$E = E_0 \cos(2\pi\nu_0 t) \quad (2.35)$$

where E_0 is the amplitude of the oscillating E-field. For a vibrational mode in material, the polarizability, α , should be written in a Taylor expansion of the normal mode describing the motion of the individual atoms in that state. The polarizability is written up to first order term as,

$$\alpha = \alpha_0 + \left. \frac{\partial \alpha}{\partial Q_k} \right|_0 Q_k \quad (2.36)$$

Here the Q_k is the normal mode describing the whole motion of individual atoms participating the k^{th} vibrational mode. Since the motion of the atoms in the vibrational mode is considered in harmonic approximation (all atoms are assumed to be harmonic oscillator), the solution of the normal mode Q_k is given as,

$$Q_k = Q_0 \cos(2\pi\nu_k t) \quad (2.37)$$

where ν_k is the frequency of the k^{th} normal mode. Using the form of E and α in Eq. 2.34 we have,

$$\mu = \alpha_0 E_0 \cos(2\pi\nu_0 t) + E_0 Q_0 \left(\left. \frac{\partial \alpha}{\partial Q_k} \right|_0 \right) \{ \cos[2\pi(\nu_0 - \nu_k)t] + \cos[2\pi(\nu_0 + \nu_k)t] \} \quad (2.38)$$

In this form of induced electric dipole we all three scattering terms; the elastic or Rayleigh scattering term which contains $\cos(2\pi\nu_0 t)$, the Stokes Raman scattering term containing $\cos[2\pi(\nu_0 - \nu_k)t]$ and the last term is the Anti-Stokes one having $\cos[2\pi(\nu_0 + \nu_k)t]$ term. Since the Stokes Raman intensity is reported experimentally, we will deal only with this term in our calculations. Using the Stokes Raman scattering term of induced dipole moment in Eq. 2.33, we have the intensity for Stokes Raman scattering,

$$I_{SR} = \frac{4\pi^3 \nu_0^4 E_0^2}{3A\epsilon_0 c^3} \langle \nu' | \left(\left. \frac{\partial \alpha}{\partial Q_k} \right|_0 \right)^2 \cos^2[2\pi(\nu_0 - \nu_k)t] | \nu \rangle \quad (2.39)$$

where we can write $I_0 = \frac{1}{2} E_0^2 \epsilon_0 c$ is the intensity of the incident light. In addition, the time average of the cosine term will give $\frac{1}{2}$. Finally, we left with the Stokes Raman scattering intensity of the form,

$$I_{SR} = \frac{8\pi^3 \nu_0^4 I_0}{3A\epsilon_0^2 c^4} \left| \langle \nu' | \left(\left. \frac{\partial \alpha}{\partial Q_k} \right|_0 \right) | \nu \rangle \right|^2 \quad (2.40)$$

Here, the initial and final states can be thought as the polarization vectors of incident light and scattered radiation. As can be seen in Eq. 2.40, the intensity of Stokes Raman scattering is proportional to the change of polarizability with respect to the normal mode of a vibration. We will call this term as the Raman activity which is given by, $\left| \langle \nu' | \left(\left. \frac{\partial \alpha}{\partial Q_k} \right|_0 \right) | \nu \rangle \right|^2$ where the term $\left(\left. \frac{\partial \alpha}{\partial Q_k} \right|_0 \right)$ is a 3×3 Raman tensor given by,

$$\begin{bmatrix} \frac{\partial \alpha_{11}}{\partial Q_k} & \frac{\partial \alpha_{12}}{\partial Q_k} & \frac{\partial \alpha_{13}}{\partial Q_k} \\ \frac{\partial \alpha_{21}}{\partial Q_k} & \frac{\partial \alpha_{22}}{\partial Q_k} & \frac{\partial \alpha_{23}}{\partial Q_k} \\ \frac{\partial \alpha_{31}}{\partial Q_k} & \frac{\partial \alpha_{32}}{\partial Q_k} & \frac{\partial \alpha_{33}}{\partial Q_k} \end{bmatrix} \quad (2.41)$$

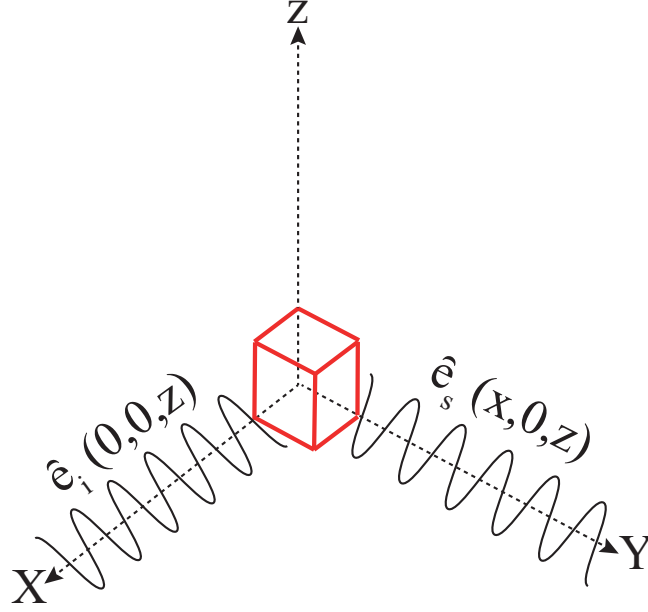


Figure 2.2. A typical experimental setup for the Raman scattering process. \hat{e}_i and \hat{e}_s represent the polarization vectors of incident light and scattered radiation.

for the k^{th} vibrational mode. Since this term includes the change of polarizability with respect to the normal mode, it is a vibrational mode-dependent property. Generally, it can be written with the knowledge of group theory for every vibrational mode.

In our calculation methodology within DFT, we are not able to directly calculate the polarizability or its change with respect to the normal mode using the package VASP. Instead, we can calculate the dielectric tensor for the material and its change with respect to the vibrations. Thus, the change in dielectric tensor can be related to the change in polarizability by the formula,

$$\frac{\partial \alpha_{ij}}{\partial Q_k} = \left(\frac{V}{4\pi} \right) \frac{\partial \epsilon_{ij}}{\partial Q_k} \quad (2.42)$$

For a vibrational mode to be a Raman active mode, the Raman tensor should be a non-zero tensor to give a non-zero intensity. If we have a non-zero Raman tensor for a vibrational mode, then we can also calculate its direction-dependent activity by changing the experimental setup. Changes in the polarization state of the incident light affects the nature and information content of the scattered radiation. However, this is true for the term itself, $\hat{e}_s \left(\frac{\partial \alpha}{\partial Q_k} \Big|_0 \right) \hat{e}_i$ where \hat{e}_s and \hat{e}_i stand for the polarization vectors of scattered radiation and incident light, respectively.

When we include the bra-ket in the notation, it means an average over all angles

of orientation of the sample with respect to the laboratory frame is taken into account. Thus, the Raman activity term can be written in terms of Raman invariants which are independent of the setup of the experiment. Especially for the systems including randomly oriented molecules, this angular averaging should be carried out to find the intensity of Raman scattering. Now let us assume that the incident light is polarized in z -direction and propagating along z -axis as shown in Fig. 2.3.1.1. The scattered radiation is detected along y -direction and possibly polarized in x - and z -directions which can be shown by the relation given in Eq. 2.34.

$$\mu_z = \alpha_{zz} E_{0z} \quad (2.43)$$

$$\mu_x = \alpha_{xz} E_{0z}$$

Thus, two possible terms will appear in the form of scattered intensity given by in Eq. 2.40, $\langle \tilde{\alpha}_{zz}^2 \rangle$ and $\langle \tilde{\alpha}_{xz}^2 \rangle$ where $\tilde{\alpha}$ denotes the derivative of the polarizability with respect to the normal mode, Q_k . Having these two terms means that with their summation one can calculate the total intensity of the scattered radiation or the partial intensities as parallel and perpendicular to the incident light. The resulting averaging for these two terms will be given in terms of the Raman invariants as,

$$\tilde{\alpha}_s \equiv \frac{1}{3}(\tilde{\alpha}_{xx} + \tilde{\alpha}_{yy} + \tilde{\alpha}_{zz}) \quad (2.44)$$

$$\beta \equiv \frac{1}{2}\{(\tilde{\alpha}_{xx} - \tilde{\alpha}_{yy})^2 + (\tilde{\alpha}_{yy} - \tilde{\alpha}_{zz})^2 + (\tilde{\alpha}_{zz} - \tilde{\alpha}_{xx})^2 + 6[(\tilde{\alpha}_{xy})^2 + (\tilde{\alpha}_{yz})^2 + (\tilde{\alpha}_{xz})^2]\} \quad (2.45)$$

where $\tilde{\alpha}_s$ and β represents the isotropic and anisotropic parts of the derivative of polarizability tensor, respectively. The importance of representing the intensity in terms of these two variables is being invariant to a change in the sample orientation. Thus, using these identities can help us to write the scattered intensity independent of the experimental setup. Finally, using these forms of isotropic and anisotropic polarizability derivative tensors, the Raman activity can be written as,

$$R_A = 45\tilde{\alpha}^2 + 7\beta^2 \quad (2.46)$$

When a detailed mathematical calculation is performed, it can be seen that although the experimental setup given in Fig. 2.3.1.1 is changed, the total averaged Raman activity remains the same with the form given in Eq. 8.4. However, the only thing that

changes under the change of experimental setup is the ratio of perpendicular Raman activity to parallel Raman activity which is known as the depolarization ratio given by,

$$\rho = \frac{I_{\perp}}{I_{\parallel}} \quad (2.47)$$

As we mentioned, the total intensity of Raman scattering along perpendicular and parallel polarization directions is invariant under experimental setup when orientational averaging is considered for the sample being analyzed.

2.4. Computational Details

For the first-principles calculations, we employed the plane-wave basis projector augmented wave (PAW) method in the framework of density-functional theory (DFT). The generalized gradient approximation (GGA) in the Perdew- Burke-Ernzerhof (PBE) form (Perdew *et al.*, 1996b) was employed for the exchange-correlation potential as implemented in the Vienna *ab-initio* Simulation Package (VASP) (Kresse and Furthmuller, 1996a,b). The van der Waals (vdW) correction to the GGA functional was included by using the DFT-D2 method of Grimme (Grimme, 2006). For calculation of the band gap, effect of spin-orbit coupling (SOC) on top of GGA was considered. More accurate calculations for electronic band gap were performed using the Heyd-Scuseria-Ernzerhof (HSE) screened-nonlocal-exchange functional of the generalized Kohn-Sham scheme (Heyd *et al.*, 2003). The charge transfer analysis was performed by using Bader technique. (Henkelman *et al.*, 2006)

For the electronic and geometric relaxations of the monolayer crystals, the total energy was minimized until the energy convergence becomes less than 10^{-5} eV in the structural relaxation and the convergence criteria for the total Hellmann-Feynman forces on the unitcell was taken to be 10^{-4} eV/Å. To prevent possible interactions between periodic images of single layers, enough large vacuum spacing was considered. The minimum energy was obtained by varying the lattice constant and the pressure was reduced below 1 kbar. A Γ -centered k-point mesh scheme was adapted for the Brillouin zone (BZ) sampling for the primitive unit cells. The broadening for the density of state (DOS) calculations was taken to be 0.05 eV.

In order to investigate the dynamical stability of monolayers, the vibrational spectra of the structures were simulated. Phonon spectra were calculated by using the small displacement method as implemented in the PHON code (Alfe, 2009). For the calculation

of force constant matrix, supercells were considered for each monolayer crystal. Each individual atom was displaced from its equilibrium position by an amount 0.04 \AA in the harmonic region.

Our results on the mechanical, electronic, and vibrational properties of novel 2D monolayer materials are presented in the following chapters. Firstly, we give our results on the mechanical properties of pentagonal monolayer crystals of graphene, boron nitride, and silver azide. Secondly, prediction of new doped holey graphene structures and their electronic and mechanical properties are presented. Next, mechanical characteristics of monolayer PTMC (GaS and GaSe) are presented in terms of their elastic constants and non-elastic parameters. Finally, as an in-plane anisotropic monolayer material, mechanical properties of ReS_2 and effect of hydrogenation on its mechanical properties are discussed. In the next chapter, tunable electronic properties of a heterobilayer structure of magnesium hydroxide ($\text{Mg}(\text{OH})_2$) and WS_2 are presented. The effect of an external electric field on the energy-band structure is investigated. Finally, vibrational properties of novel 2D monolayer materials from different structure families are discussed in terms of their Raman spectra and the effect of in-plane biaxial strain on their Raman spectra are given.

CHAPTER 3

MECHANICAL PROPERTIES OF MONOLAYERS OF PENTAGONAL CRYSTAL STRUCTURE

In the last decade, graphene, one atom thick form of carbon atoms arranged in a honeycomb structure, has become one of the most exciting topics of materials research due to its exceptional properties (Novoselov *et al.*, 2004). Besides graphene (Novoselov *et al.*, 2005), there exists many other forms of pure carbon in nature such as graphite, diamond, C₆₀ fullerene (Kroto *et al.*, 1985), nanotube (Iijima and Ichihashi, 1993), carbon nanocone (Charlier and Rignanes, 2001), nanochain (Jin *et al.*, 2009) and graphdiyne (Li *et al.*, 2014) which are the well known bulk and low dimensional forms of carbon element. In addition to these, stability and unique mechanical properties of a new carbon allotrope, p-graphene, are reported by Zhang *et al.* recently (Zhang *et al.*, 2015). It is shown that while the unique pentagonal crystal symmetry provides a dynamical stability (for temperatures up to 1000 K), the buckled nature of the p-graphene leads to a negative value for its Poisson's ratio.

Metal azides, consisting of a metal atom (Na, K, Rb, Cs, Ag, Cu or Tl) and the azide molecule (N₃), are another group of compounds which may find applications in monolayer crystal technology. Their electronic structure, chemical bonding, vibrational and optical properties have been investigated (Gordienko and Poplavnoi, 2005; Jain *et al.*, 2013; Gordienko *et al.*, 1996; Gordienko and Poplavnoi, 2004; Zhu and Xiao, 2007, 2008, 2010; Colton and Rabalais, 1976; Schmidt *et al.*, 2007; Hou *et al.*, 2011). Due to its large chemical energy stored in its bulk phases, AgN₃ is one of the intensely studied members of this family. Gordienko *et al.* (Gordienko and Poplavnoi, 2005) have studied the electronic band structure of AgN₃ by using density functional theory (DFT) calculations. Jain *et al.* (Jain *et al.*, 2013) calculated the energy band gap of AgN₃ as 2.95 eV. Using a pseudoatomic orbital basis, the electronic structure of AgN₃ was also reported (Gordienko *et al.*, 1996). Change of structural and vibrational properties of AgN₃ under applied pressure was studied by using DFT and generalized gradient approximation (GGA) (Zhu and Xiao, 2007). Moreover, Schmidt *et al.* (Schmidt *et al.*, 2007) reported the crystal structure and chemical bonding of the high temperature phase of AgN₃ by using X-ray powder diffraction. In this study it was pointed out that the high temperature-AgN₃ phase contains buckled layers with silver atom connecting to the azide groups in pentagonal form in the direction parallel to [001]. The phase transitions and structures of AgN₃ at

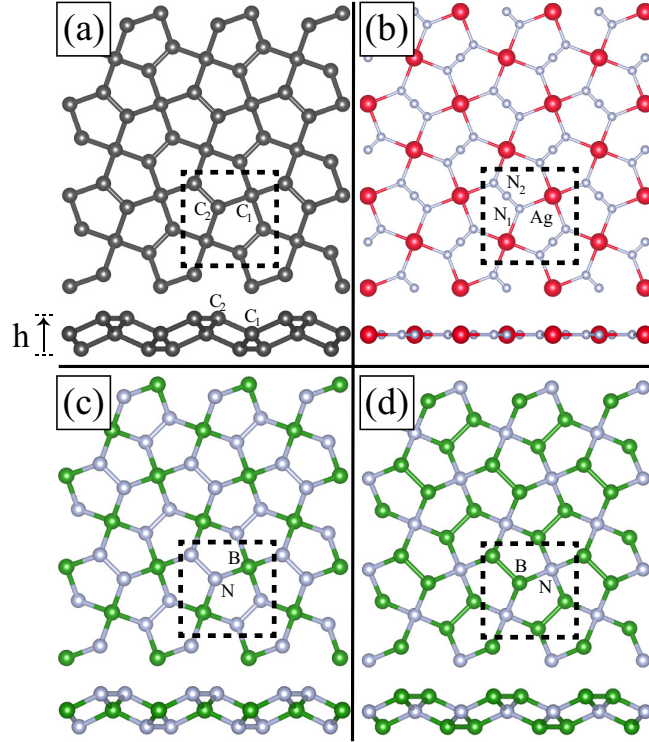


Figure 3.1. Top view and side view of pentagonal (a) graphene (b) AgN_3 , (c) B_2N_4 , (d) B_4N_2 .

different pressure values were also reported by Hou *et al.* (Hou *et al.*, 2011)

In this chapter we investigate the structural, electronic and mechanical properties of pentagonal monolayers of carbon (p-graphene), two phases of boron nitride (p- B_2N_4 and p- B_4N_2) and silver azide (p- AgN_3). The mechanical properties of these pentagonal structures are examined under uniaxial strain and in terms of the in-plane stiffness and the Poisson's ratio values. Their vibrational spectra are also calculated. The paper is organized as follows: Structural properties of four different pentagonal structures are presented in Sec. 3.1. The electronic and magnetic properties of optimized structures are investigated in Sec. 3.2. In Sec. 3.3 mechanical properties and dynamical stability of the pentagonal structures are investigated. Finally we present our conclusions in Sec.3.4.

The cohesive energy of a unit cell was calculated using the formula $E_c = \sum n_a E_a - E_{str}$, where E_a denotes the energy of a single isolated atom and n_a denotes the number of atoms contained in the unit cell. E_{str} denotes the total energy of the monolayer structure. Summation is used for the structure containing different types of atoms in its simulation cell. Calculated cohesive energies are listed in Table 3.

Table 3.1. Geometry of pentagonal structures, calculated lattice parameter a , the distance between atoms d_{XY} , buckling of the monolayer h , total magnetic moment μ , the amount of charge lost or gained by the atoms $\Delta\rho$, the total cohesive energy of a primitive unitcell E_c , the energy band gap of the structure E_g , work function Φ , Poisson's ratio ν and in-plane stiffness C .

	Geometry	a (Å)	d_{XY} (Å)	h (Å)	μ (μ_B)	$\Delta\rho$ (e)	E_c (eV)	E_g (eV)	Φ (eV)	ν	C (eV/Å ²)
p-Graphene	<i>buckled</i>	3.64	1.34 (C ₁ -C ₁) 1.55 (C ₁ -C ₂)	1.21	0	0.3	42.40	2.21	6.01	-0.08	16.71
p-AgN ₃	<i>planar</i>	6.01	1.19 (N-N) 2.33 (Ag-N)	-	0	2.1	31.45	1.33	3.43	0.90	0.37
p-B ₂ N ₄	<i>buckled</i>	3.62	1.34 (N-N) 1.55 (B-N)	1.26	0	4.2	34.49	-	5.19	-0.02	3.62
p-B ₄ N ₂	<i>buckled</i>	3.79	1.59 (B-B) 1.57 (N-B)	1.23	1.95	4.3	33.58	-	3.88	-0.19	7.59

3.1. Structural Properties

Firstly geometrical relaxations of structures were performed by considering their square-shaped primitive unitcells with the lattice vectors $a_1=a(1,0,0)$ and $a_2=a(0,1,0)$ for all structures (see Fig. 3). In the structure of p-graphene the 4-coordinated carbon atoms were denoted by C₁ while the 3-coordinated ones were denoted by C₂. The geometrical calculations show that the bond length of C₁-C₂ is 1.55 Å while C₂-C₂ bond length is 1.34 Å. The lattice constant is $a=3.64$ Å within GGA approximation and it is consistent with the value calculated by Zhang *et al.* (Zhang *et al.*, 2015) The buckling of the layer is 1.21 Å which is also consistent with the value calculated by Zhang *et al.* (Zhang *et al.*, 2015) Bader charge analysis indicates that 0.3 e amount of charge is donated from C₁ and two C₂ atoms to other two C₂ atoms. The calculated cohesive energy is 42.40 eV for p-graphene monolayer.

For p-AgN₃ geometry relaxation 8-atomic primitive unitcell was considered. As seen in Fig. 3(b) 2-coordinated N atoms are denoted by N₁ while 3-coordinated ones are denoted by N₂. The geometry relaxation within the GGA approximation gives the lattice constant value as $a=6.02$ Å. The Ag-N₁ bond length is 2.33 Å while the N₁-N₂ bond length is 1.19 Å. The bond angle between the Ag-N₁-Ag atoms is 132.5 degrees and it is 90 degrees for the N₁-Ag-N₁ bonds. The relaxed geometry of AgN₃ monolayer structure is planar similar to some other two dimensional structures such as hexagonal graphene and h-BN. Bader charge analysis shows that an amount of 0.7 e charge from each Ag atom was donated to the N atoms but dominantly to the central ones. The final charge on the Ag, N₁ and N₂ atoms and N₁ atom are 10.3 e , 5.2 e and 5.3 e respectively. The total

cohesive energy of p-AgN₃ is 31.45 eV as listed in Table 3.

Optimized lattice constant of the p-B₂N₄ is found to be $a=3.62$ Å. The N-N and B-N bond lengths are 1.34 Å and 1.55 Å, respectively. The buckling of p-B₂N₄ is 1.26 Å which is close to that of p-graphene. The Bader charge analysis demonstrates that B atoms have final charge of 0.9 e so that an amount of 2.1 e charge was transferred to the N atoms from each B atom. The cohesive energy of p-B₂N₄ monolayer is calculated as 34.49 eV.

The p-B₄N₂ has a lattice constant of $a=3.79$ Å which is greater than that of p-B₂N₄. This time the B-N bond length is 1.57 Å while the B-B bond length is 1.59 Å. The buckling of p-B₄N₂ is 1.23 Å which is close to that of the p-B₂N₄ structure. Results of Bader charge analysis indicates that an amount of 2.2 e charge was depleted to each N atom from the B atoms. Finally the cohesive energy of p-B₄N₂ is 33.58 eV.

3.2. Electronic Properties

In this section the electronic band dispersion and magnetic ground state of p-graphene, p-AgN₃, p-B₂N₄ and p-B₄N₂ are investigated comprehensively. As seen in Table 3, the p-graphene has an indirect band gap of 2.21 eV. As shown in Fig. 3.2(a) the valence band maximum (VBM) of the p-graphene is located in between the Γ and the X (high symmetry) points while the conduction band minima (CBM) is in between the M and the Γ points. It also appears that the both spin up and spin down states are degenerate throughout the Brillouin Zone and thus the structure does not exhibit any spin polarization in its ground state. In the 6-atomic primitive unitcell of the p-graphene while two of the 4-coordinated C atoms have no excess electrons, four 3-coordinated C atoms pair their electrons in p_z orbitals and therefore the p-graphene has a nonmagnetic ground state.

The p-AgN₃ has an indirect band gap of 1.33 eV as seen in Table 3. In Fig. 3.2(b) the VBM of the p-AgN₃ is in between the Γ and the X points while the CBM exists in between the M and the Γ points. As it is seen in Fig. 3.2(b) that the p-AgN₃ also does not exhibit any spin.

The p-B₂N₄ is another structure having nonmagnetic ground state. As seen in Fig. 3.2(c), again the spin up and the spin down states are degenerate. Unlike the p-graphene and the p-AgN₃, the p-B₂N₄ displays metallic behavior. The valence band crosses the Fermi level in between all high symmetry points through whole Brillouin Zone.

In all the pentagonal structures considered, only the p-B₄N₂ has a spin polarization in its ground state. The total magnetic moment of p-B₄N₂ is 1.95 μ_B as given in Table

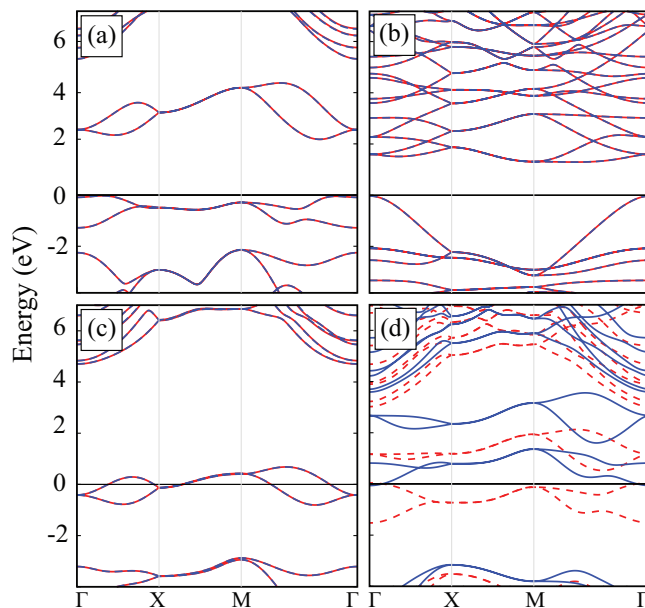


Figure 3.2. Band-structures of pentagonal (a) graphene (b) AgN_3 , (c) B_2N_4 , (d) B_4N_2 where blue lines denote up spins while dashed red lines denote down spins respectively.

3. This value of total magnetic moment arises from the ferromagnetic ordering of B local moments. In the primitive unit cell each B atom has a local magnetic moment of $0.48 \mu_B$ while the each N atom has local moment about $0.02 \mu_B$ which is very small compared to that of B atom. Therefore, the net magnetic moment of $1.95 \mu_B$ for p- B_4N_2 structure is mostly due to local moments of B atoms. In its 6-atomic primitive unit cell both N atoms are 4-coordinated while all the B atoms are 3 coordinated. The spin polarization is localized on the N atoms since they add up their electrons in their p_z orbitals. As given in Fig. 3.2(d) the spin up and spin down states have different dispersions. Only in between the high symmetry points Γ and the X , M and the Γ the spin up and spin down bands cross each other just above the Fermi level. The valence band of spin down states crosses Fermi level while the conduction band of spin up states crosses Fermi level. The band structure metallic for both spins but if spin orbit coupling is included, then there may open a band gap at the points where the up and down spin bands cross.

The charge density difference plots of pentagonal structures are provided in Fig. 3.3. In order to plot these figures we first obtained the total charge density of each material. Then, using the same unit cell and settings we obtained the charge density of each atom separately at their original positions in the compound. After that we summed these individual charge densities and subtracted them from the charge density of the compound.

These figures reveal the modifications in the total charge of the individual atoms when the crystal is formed. The charge density difference plot of p-graphene Fig. 3.3(a) shows that there is a charge depletion in the hollow site of the lattice. This charge is accumulated mostly at the bonding sites between the C atoms. The figure for the AgN₃, Fig. 3.3(b), indicates that there is a charge depletion from the N₂ atoms and a charge accumulation at the region where the N₁-N₂ and N₁-Ag chemical bonds are formed. The hollow site charge depletion is also observed for B₂N₄ in Fig. 3.3(c). Similar to previous cases, there is a charge accumulation at the locations where the B-N chemical bonds are formed. For the case of B₄N₂ in Fig. 3.3(d), there is a charge depletion from the one side of the B atoms and again a charge accumulation at the bonding sites.

For the p-graphene, the charge transfer is from C₁ atoms and 2 of C₂ atoms to other C₂ atoms. For the p-AgN₃, as seen in Fig. 3.3(b) there exists a charge depletion from Ag and N₁ atoms to central N atoms in azide group. For the p-B₂N₄ structure all of the charge given in Table 3 is depleted to the N atoms as depicted by the charge density plot in Fig. 3.3(c). Finally for p-B₄N₂ monolayer again the charge depletion occurs from B atoms to N atoms.

3.3. Elastic Constants

The stiffness can be explained as the rigidity or the flexibility of a material. The parameter which shows the mechanical response of a material to an applied stress is called the Poisson's ratio. It is defined as the ratio of the transverse contraction strain to the longitudinal extension strain in the direction of stretching force. The in-plane stiffness and the Poisson's ratio can be deduced from the relationship between the strain and the total energy. To calculate the mentioned parameters, we apply strain ε_x and ε_y to these materials by changing the lattice constants along x and y directions. The strain range is from -0.02 to 0.02 with a step of 0.01 which gives a data grid of 25 points. At each grid point, the atomic positions are relaxed and the strain energy E_S , which is the energy difference between strained and unstrained structures, is calculated. In the harmonic region the strain energy can be fitted as $E_S = c_1\varepsilon_x^2 + c_2\varepsilon_y^2 + c_3\varepsilon_x\varepsilon_y$. The in-plane stiffness along x and y directions can then be calculated as $C_x = (1/S_0)(2c_1 - c_3^2/2c_2)$ and $C_y = (1/S_0)(2c_2 - c_3^2/2c_1)$ where S_0 is the unstretched area of the supercell. The Poisson's ratio along x and y directions can be obtained by $\nu_x = c_3/2c_2$ and $\nu_y = c_3/2c_1$, respectively. For all pentagonal structures we find that the in-plane stiffness and the Poisson's ratio along x and y directions are equal.

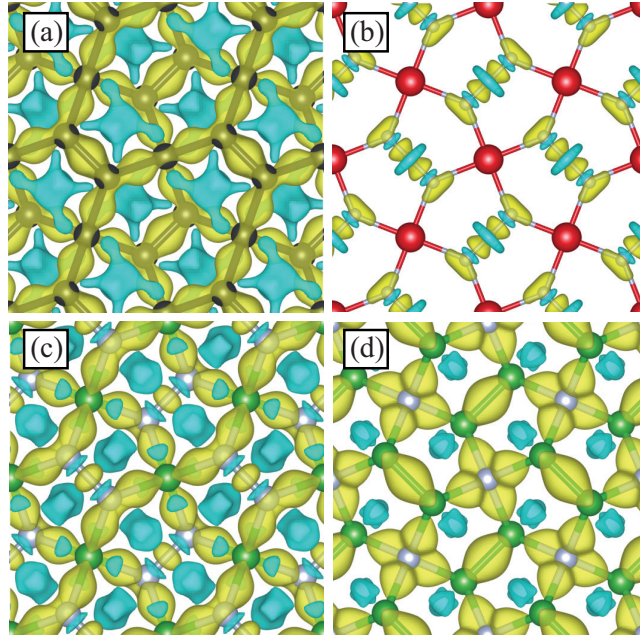


Figure 3.3. Charge density difference of pentagonal (a) graphene, (b) AgN_3 , (c) B_2N_4 and (d) B_4N_2 .

The calculated in-plane stiffness and Poisson's ratio are listed in Table 3. It can be seen that p-graphene has the largest in-plane stiffness of $16.71 \text{ eV}/\text{\AA}^2$, indicating strong bonding between carbon atoms. However, this value is smaller than that of graphene, which has an in-plane stiffness of $20.91 \text{ eV}/\text{\AA}^2$. (Topsakal *et al.*, 2009) This can be attributed to different number of bonds in p-graphene and graphene. In graphene, each C atom is 3-fold coordinated, while in graphyne the average coordination number of C atom is 2.67. P-graphene has fewer number of bonds than graphene, so it has relatively smaller in-plane stiffness. The calculated Poisson's ratio for p-graphene is -0.08 which is consistent with the value calculated by Zhang *et al.* (Zhang *et al.*, 2015)

The p- AgN_3 has a large Poisson's ratio of 0.90, revealing its strong ability to preserve the equilibrium area when strain is applied. The Poisson's ratio for p- B_4N_2 is -0.19, this is consistent with the calculation of in-plane stiffness. P- B_2N_4 has an in-plane stiffness of $3.62 \text{ eV}/\text{\AA}^2$, much smaller than the p-graphene. For p- B_4N_2 , the in-plane stiffness is $7.59 \text{ eV}/\text{\AA}^2$. It is interesting to note that the p-graphene, the p- B_2N_4 and the p- B_4N_2 have negative Poisson's ratio values, contrary to the most of the existing materials. Therefore, they belong to the so-called auxetic structures. When uniaxial tensile strain is applied to these structures, the lattice along the transverse direction expands rather than compresses. Normally, this ratio is positive and most of the solids expand in the trans-

verse direction when they are subjected to a uniaxial compression. The materials with negative Poisson's ratio unfolds when they are stretched. Therefore, they are isotropic in two dimensions for certain lengths and angles. It has been reported that some artificial materials have negative Poisson's ratio and they exhibit excellent mechanical properties (Burns, 1987; Jiang and Park, 2014). In contrast to structure-engineered bulk auxetics, the negative Poisson's ratio is intrinsic in single layers of p-graphene, p-B₂N₄ and p-B₄N₂.

We also consider higher values of strain from 0.04 to 0.40 in uniform expansion, in order to see structural deformations and determine the linear and non-linear elastic regions for each pentagonal structure. For this purpose, we prefer a fully symmetric square lattice with well defined high symmetry points in the BZ. Again the calculations are performed in a 2×2 supercell. Increasing the strength of applied strain, increases the total energy of the structure. The p-graphene has no structural deformation up to the strain value of 40% but the buckling of the layer decreases to 0.66 Å. Under 40% strain, the C₂-C₂ and C₁-C₂ bond lengths are 1.35 Å and 2.15 Å, respectively. P-AgN₃ also does not have any structural deformation up to 40% strain. It remains in the same form but with a higher Ag-N₁ bond length of 3.47 Å while the bond lengths in azide group remain the same. The situation is different for pentagonal structures of B and N, because they both have deformations in their structures at some critical strain values. P-B₂N₄ has not a pentagonal shape structure when 12% strain is applied. Therefore one may say that it is the critical strain value for p-B₂N₄ between linear and non-linear elastic regions. Non-linear elastic region refers to a region in which irreversible structural changes occur in the system and it transforms into a different structure. This critical strain value is slightly greater for p-B₄N₂. After the strain strength of 16%, p-B₄N₂ transforms into a different structure.

As an important feature of mechanical properties we also examine the dynamical stability of pentagonal monolayer structures by performing phonon calculations. Here, the dynamical matrix and the vibrational modes were calculated using the small-displacement method (SDM) (Alfe, 2009) with forces obtained from VASP. As shown in Fig. 3.3, while pentagonal structures of graphene and B₂N₄ have real vibrational eigenfrequencies in the whole Brillouin zone, p-AgN₃ and p-B₄N₂ have some phonon branches with zero-frequency modes at several points in the Brillouin zone. This is an indication of irreversible deformations that can be induced by those vibrational modes. It appears that although the total energy calculations yield optimized atomic structures of p-AgN₃ and p-B₄N₂ these structures are dynamically unstable. Our calculations also reveal that p-graphene and p-B₂N₄ not only possess dynamically stable crystal structures but also have

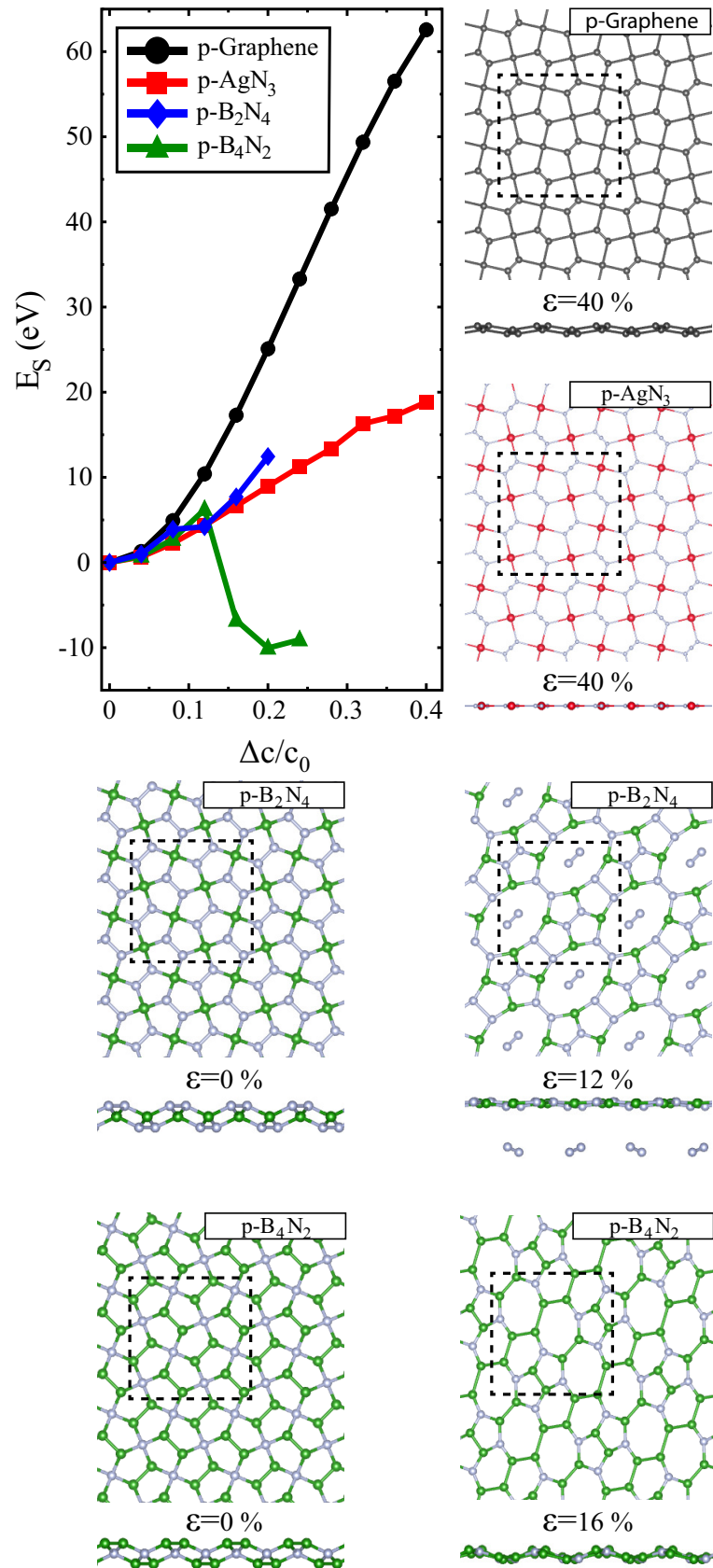


Figure 3.4. Energy variation of the pentagonal structures under applied strain and the corresponding atomic configurations at given strain strengths.

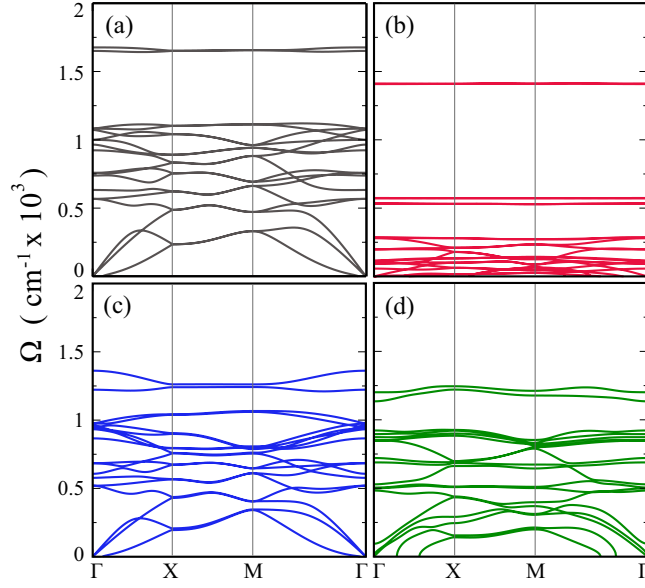


Figure 3.5. Phonon modes of pentagonal (a) graphene (b) AgN_3 , (c) B_2N_4 , (d) B_4N_2 .

quite high-frequency phonon modes indicating strong bond formation in these materials.

3.4. Conclusions

Motivated by the unique properties of the recently reported p-graphene we have investigated the structural, mechanical and electronic properties of three novel pentagonal structures as well as p-graphene. Our calculations demonstrate that pentagonal structures of graphene and BN have buckled geometries while p- AgN_3 has a planar geometry. Calculated band structures show that although hexagonal graphene is a zero-band gap semiconductor, the band dispersion of p-graphene displays an indirect-band-gap semiconductor behavior. Also the band dispersion of p- AgN_3 displays semiconducting behavior with an indirect band gap. However, pentagonal structures of BN are metallic while hexagonal BN monolayer is a wide-band-gap semiconductor. For all of the pentagonal structures investigated in this study only p- B_4N_2 has a magnetic ground state while the other structures have nonmagnetic ground states. We have also studied the mechanical properties of these structures and calculated their in-plane stiffness and corresponding Poisson's ratios. The stiffest monolayer is found to be the p-graphene among the four structures. p-graphene, p- B_2N_4 and p- B_4N_2 all have negative Poisson's ratio while the p- AgN_3 has a positive Poisson's ratio. Also the uniform strain calculations indicate that p-graphene and p- AgN_3

do not show any irreversible structural deformations for up to large strain values while $p\text{-B}_2\text{N}_4$ and $p\text{-B}_4\text{N}_2$ deform into different phases at some certain strain strengths.

CHAPTER 4

PREDICTION OF NOVEL 2D MONOLAYERS OF HOLEY GRAPHENE CRYSTALS

The lack of a band gap is the major obstacle for the use of graphene in electronic applications such as field-effect transistors (Wang *et al.*, 2009), and electrodes in solar cells (Xue *et al.*, 2012; Osella *et al.*, 2012). Thus, tuning its electrical properties through opening of a band gap is of great technological importance (Wang *et al.*, 2009; Berger *et al.*, 2006; Wei *et al.*, 2009). Nitrogen doping has been widely studied as one of the most feasible methods to modulate the electronic and other properties of graphene and its derivatives (Dai, 2013; Zhang *et al.*, 2013; Dai *et al.*, 2012; Gong *et al.*, 2009; Zhao *et al.*, 2011).

A series of covalent organic frame-works (COFs) (Xiang and Cao, 2013; Colson and Dichtel, 2013; Colson *et al.*, 2011; Feng *et al.*, 2012) have been designed to form large graphene-like honeycomb networks. In 2005, Yaghi *et al.* demonstrated the utility of the topological design principle in the synthesis of porous organic frameworks which are connected with covalent bonds, which are the first successful examples of these COFs (El-Kaderi *et al.*, 2007). Since COFs are composed of light-weight elements linked by strong covalent bonds, they have low mass densities and possess high thermal stability. The successful realization of COFs with molecular graphene-type building blocks would provide covalent frameworks that could be functionalized into light-weight materials optimized for gas storage, photonic, and catalytic applications (El-Kaderi *et al.*, 2007; Han *et al.*, 2008).

N-doped graphene-like honeycomb structures are important examples of COF materials. In a recent study by Mahmood *et al.* (Mahmood *et al.*, 2015) the design and preparation of a two dimensional holey crystal, C_2N , with uniform holes and nitrogen atoms was reported. The structure and band gap of C_2N were studied by using both experimental techniques and DFT-based calculations. This new structure is layered like graphite with a different interlayer distance and is highly crystalline. It exhibits a direct band gap which was determined as 1.96 eV by using ultraviolet visible spectroscopy, while a slightly smaller band gap of 1.70 eV is obtained from density functional theory (DFT) calculations. In another study, Sahin investigated the structural and phononic characteristics of the C_2N structure (Sahin, 2015). The formation of heterostructures of holey graphenes and the resulting Moiré patterns were investigated by Kang *et al.* (Kang *et al.*, 2015). Very

recently Zhang *et al.* investigated the structural and electronic properties of few-layer C_2N by considering different stacking orders and number of layers (Zhang *et al.*, 2015). In the study by Xu *et al.* energy barriers for the adsorption of H_2 , CO_2 and CO molecules on C_2N monolayer were calculated for a possible H_2 dissociation (Xu *et al.*, 2015).

Motivated by the recent experiment on synthesis of C_2N monolayer (Mahmood *et al.*, 2015) and by the studies on graphene-like networks composed of COFs, we investigate the structural, electronic and mechanical properties of 2D holey crystals of C_2X ($X=N, P$ or As) stoichiometry. The mechanical properties of these hexagonal structures are examined under uniaxial strain, and the in-plane stiffness and the Poisson ratio values are obtained. In addition, the most probable types of atomic scale disorder, formation of N, P and As defects, are investigated for these holey structures.

The chapter is organized as follows: Discussions about electronic and magnetic properties of these monolayer crystals are given in Sec. 4.2. In Sec. 4.3 the mechanical properties are discussed by examining the in-plane stiffness and the Poisson ratio for each structure. Electronic and geometric properties of defect and H-impurities in C_2X monolayers are discussed in Sec. 4.4. Finally we conclude in Sec. 4.5

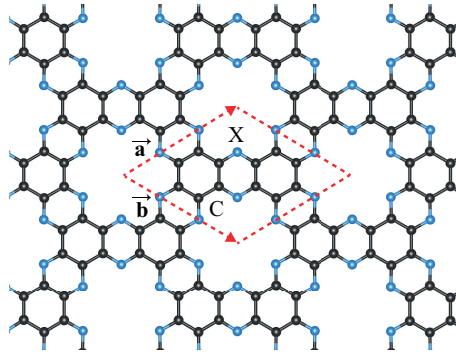


Figure 4.1. Top view of C_2X holey graphene monolayer structure where X represents N, P or As atoms.

The cohesive energy per atom in a primitive unit cell was calculated using the formula;

$$E_{\text{coh}} = [12E_C + 6E_X - E_{C_2X}]/18 \quad (4.1)$$

where E_C and E_X denote the magnetic ground state energies of the single C and X atoms, respectively while E_{C_2X} denotes the total energy of the monolayer C_2X . Calculations on elastic constants were performed by considering a 2×2 supercell containing 72 atoms.

Table 4.1. The calculated ground state properties of C_2X -structures, structural geometry, lattice parameters of primitive unit cell, a (see Fig. 4.1); the distance between C-X atoms, d_{C-X} ; the distance between two carbon atoms, d_{C-C} ; the average charge donated to (+) or from (-) each C atom, $\Delta\rho$; the cohesive energy per atom in primitive unitcell, E_{coh} ; the energy band gap of the structure calculated within, GGA with the inclusion of SOC, E_g^{GGA} ; and HSE06, E_g^{HSE} ; workfunction, Φ ; Poisson's ratio, ν ; and in-plane stiffness C . Calculated parameters for graphene and h-BN are given for comparison. ¹ (Lee *et al.*, 2008) and ² (Berseneva *et al.*, 2013)

	a (Å)	d_{C-X} (Å)	d_{C-C} (Å)	$\Delta\rho$ (e)	E_{coh} (eV)	E_g^{GGA} (eV)	E_g^{HSE} (eV)	Φ (eV)	ν	C (eV/Å ²)
C ₂ N	8.33	1.34	1.47	-0.6	7.64	1.66(d)	2.47(d)	5.23	0.26	9.27
C ₂ P	9.33	1.76	1.42	+0.6	6.84	0.22(i)	0.94(d)	4.90	0.21	6.69
C ₂ As	9.72	1.92	1.41	+0.3	5.78	0.43(d)	1.16(d)	4.89	0.21	5.83
Graphene	2.46	-	1.42	0.0	7.97	-	-	4.51	0.16 ¹	21.25 ¹
h-BN	2.51	1.45 (B-N)	-	+2.1	7.10	4.48(d)	5.56(d) ²	5.80	0.22	17.12

4.1. Structural Properties

Generic forms of the monolayer structures, C₂N, C₂P and C₂As, display honeycomb symmetry as shown in Fig. 4.1. All calculated parameters for their relaxed geometries are listed in Table 4.1. In the primitive unit cell there are 12 C atoms and 6 X atoms, X being N, P or As. The C₂N crystal has a planar two dimensional structure with a lattice constant of 8.33 Å which is consistent with the value reported by Mahmood *et al.* (Mahmood *et al.*, 2015) The calculated C-C bond length is 1.47 Å while the C-N bonds are 1.34 Å with the C-N-C bond angle being 118 degrees. This bond angle is the largest one of all three structures. This means that the hole between the benzene rings is nearly a perfect hexagon in C₂N. Bader charge analysis shows that an average 0.6 e of charge depletion per atom occurs from C atoms to the neighboring N atoms. The cohesive energy per atom is highest for the C₂N structure with a value of 7.64 eV, as calculated using Eq. (4.1).

Optimized lattice constant of the C₂P monolayer crystal is calculated to be 9.33 Å. The C-C bond length is 1.42 Å as in graphene hexagons and the C-P bond length is 1.76 Å. The C-P-C bonds have a narrower angle than that of the C-N-C bonds with a value of 108 degrees. According the Bader charge analysis, opposite to the C₂N case an average of 0.6 e charge is transferred to each C atom from the P atoms. The cohesive energy per atom, 6.84, eV is less than that of C₂N.

For the C₂As monolayer structure the lattice constant is 9.72 Å with a correspond-

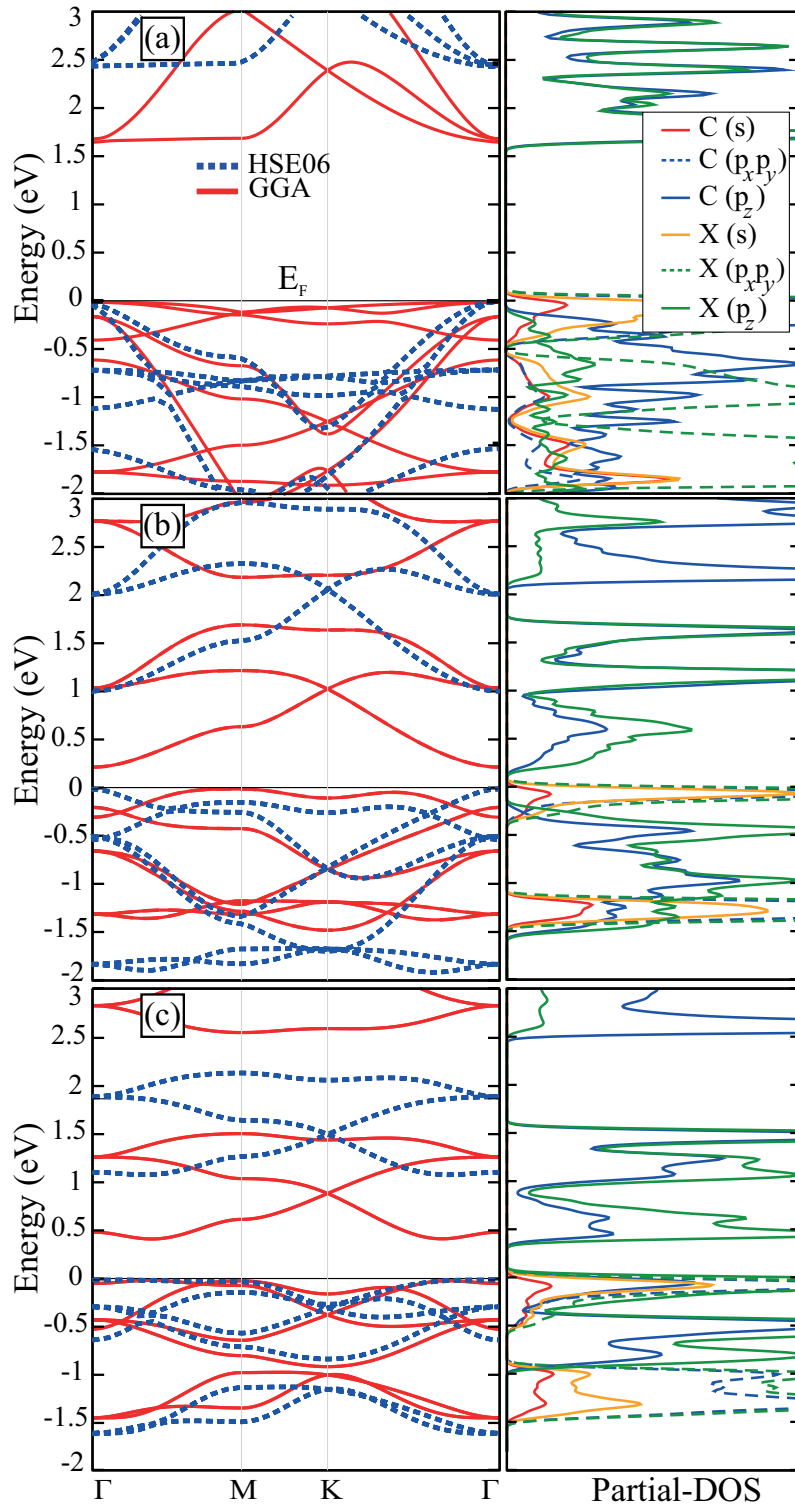


Figure 4.2. Band-structures (left-panel) and corresponding partial density of states (right-panel) of (a) C_2N (b) C_2P , and (c) C_2As where red curves are for bands calculated within GGA approximation while dashed blue curves are for bands calculated within HSE06 on top of GGA. The Fermi energy (E_F) level is set to the valence band maximum.

ing C-C bond length of 1.41 Å which is nearly the same as the C-C bond in C₂P. The longest bond length between a C atom and its X neighbor is found for the C-As bond with a value of 1.92 Å. The angle between two C-As bonds, 108 degrees, is smaller than that of the C-N bonds. We found that the charge transfer occurs in this structure from As atoms to each C atom with a value of 0.3 *e*. The charge transfer occurs from P and As atoms to the C rings for C₂P and C₂As, respectively. However, it occurs from C rings to the N atoms in C₂N.

4.2. Electronic And Magnetic Properties

The calculated lattice constant and electronic band gap of C₂N are in agreement with the values reported by Mahmood *et al.* (Mahmood *et al.*, 2015) C₂N monolayer has a direct band gap of 1.66 eV and 2.47 eV in GGA and HSE06 levels, respectively as seen in Fig. 4.2(a). The overall dispersion characteristic of the bands are not affected by the inclusion of HSE06. The valence band maximum (VBM) and conduction band minimum (CBM) of the C₂N monolayer lies at the Γ point of the Brillouin zone. Relatively large value of the C₂N energy band gap makes it a suitable semiconductor for various device applications. It also appears from the energy band structure that spin up and spin down states are degenerate throughout the Brillouin Zone and therefore the structure does not exhibit any spin polarization in its ground state. Due to the pairing of p_z electrons of 3-coordinated C atoms and 2-coordinated N atoms, the structure has a nonmagnetic ground state.

The electronic band dispersion for the C₂P monolayer crystal indicates that it has an indirect band gap of 0.22 eV and a direct gap of 0.94 eV in GGA and HSE06 levels, respectively. Since the VBM of C₂P monolayer consists of localized states, these states are affected by the HSE06 functional and the VBM point of the band structure moves to the Γ point as shown in Fig. 4.2(b). Like the C₂N monolayer, C₂P has also a nonmagnetic ground state.

In Table I, the workfunctions of the monolayer holey graphenes are also shown. It is seen that the workfunction values of these compounds are smaller than that of the h-BN and larger than the value for graphene. Comparing the workfunction values of the monolayers a decreasing trend can be seen from nitrogenated one to the arsenicated one. This result can be explained by the decreasing ionization energy of the elements in the periodic table from top to bottom rows.

The C₂As monolayer crystal is a semiconductor with a direct band gap of 0.43

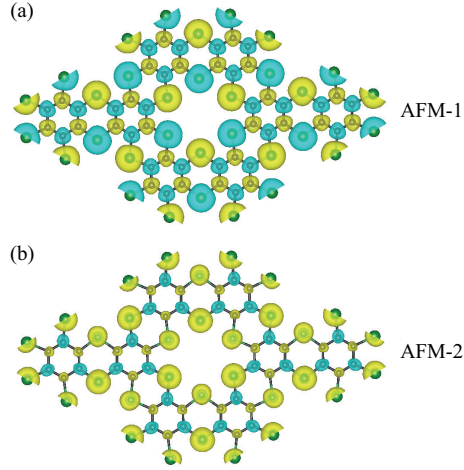


Figure 4.3. Charge density difference, $\rho_{up}-\rho_{down}$, of C_2As monolayer structure for (a) fully anti-ferromagnetic (AFM-1) order and (b) anti-ferromagnetic order in the benzene ring (AFM-2) where green/yellow color is for minority/majority spin states. The plotted isosurface values are $10^{-3} e/\text{\AA}^3$ and $10^{-5} e/\text{\AA}^3$ for (a) and (b) respectively.

eV and 1.16 eV in GGA and HSE06 levels, respectively. Similar to the case of C_2N , the inclusion of HSE06 functional increases the energy gap and does not change the dispersion characteristic of the band structure (see Fig. 4.2(c)). Both the VBM and the CBM of C_2As lie between the Γ and the M points. Interestingly, there is an isolated Dirac point in the conduction band of C_2As which can be populated using doping or a gate potential. The net magnetic moment for this structure is zero like for the other two monolayers. But the ground state is obtained for anti-ferromagnetic (AFM-1) ordering given in Fig. 4.3(a) in which all the neighboring C and As atoms have equal but opposite local magnetic moments in their sublattices. In the AFM-2 magnetic ordering, the C atoms in a ring, have opposite magnetic moments while the As atoms have ferromagnetically ordered moments as seen in Fig. 4.3(b). The net magnetic moments of the two configurations, AFM-1 and AFM-2, are zero with an energy difference of 50 meV, AFM-1 being the ground state.

4.3. Mechanical Properties

The elastic properties of homogeneous and isotropic materials can be represented by two independent constants, the in-plane stiffness C and the Poisson ratio ν . The stiffness parameter is a measure of the rigidity or the flexibility of a material. The mechanical

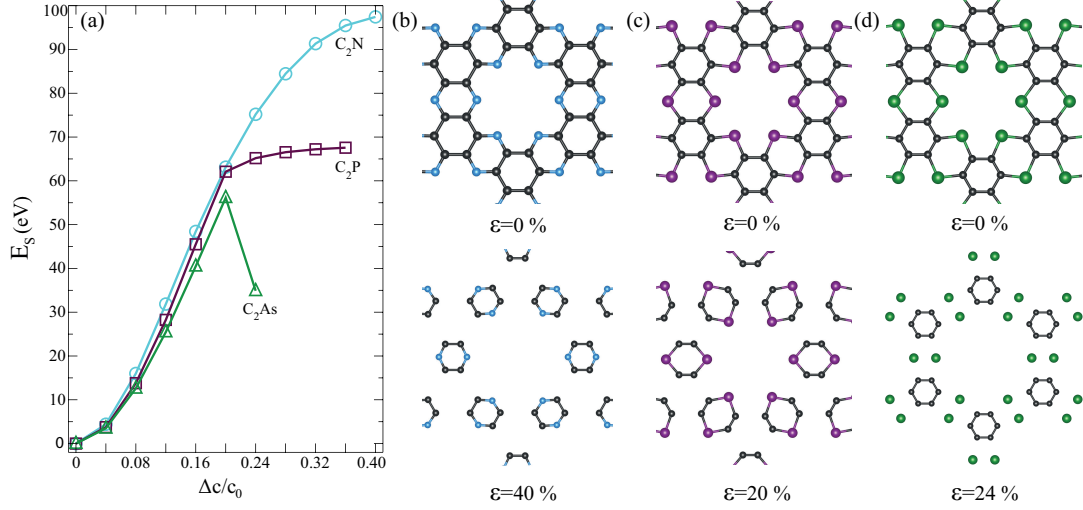


Figure 4.4. (a) Change of total energy of the three holey graphene monolayers under applied strain. Structural changes under applied strain of (b) C_2N , (c) C_2P and (d) C_2As .

response of a material to an applied stress is called the Poisson ratio. It is also defined as the ratio of the transverse contraction strain to the longitudinal extension strain in the direction of the stretching force, that is $\nu = -\epsilon_{trans}/\epsilon_{axial}$.

To calculate the elastic constants of C_2N , C_2P and C_2As monolayers, a 2×2 supercell containing 72 atoms is considered. The strains ϵ_x and ϵ_y are applied to the monolayer crystals by varying the lattice constants along the x and y directions. The strain parameters ϵ_x and ϵ_y are varied between ± 0.02 with a step size of 0.01. For this purpose three different sets of data are calculated; (i) $\epsilon_y=0$ and ϵ_x varying, (ii) $\epsilon_x=0$ and ϵ_y varying and (iii) $\epsilon_x=\epsilon_y$. At each configuration, the atomic positions are fully relaxed and the strain energy, E_S , is calculated by subtracting the total energy of the strained system from the equilibrium total energy. The calculated data is fitted to the equation $E_S = c_1\epsilon_x^2 + c_2\epsilon_y^2 + c_3\epsilon_x\epsilon_y$, so that the coefficients c_i are determined. The in-plane stiffness C can then be calculated from $C = (1/A_0)(2c - c_3^2/2c)$ where we let $c_1=c_2=c$ due to isotropy of the unit cell and A_0 is the unstretched area of the 2×2 supercell. The Poisson ratio is obtained as $\nu = c_3/2c$. Due to the symmetry of the honeycomb lattice, the in-plane stiffness and the Poisson ratio are the same along the x and y directions.

As indicated in Table 4.1, the calculated in-plane stiffness for C_2N is 9.27 eV/\AA^2 which has the highest value among the three monolayer structures. This value indicates a strong bonding between the C and N atoms. Although it is the highest value, it is still smaller compared to that of graphene and h-BN (Lee *et al.*, 2008). The calculated Poisson

ratio for the C_2N monolayer is 0.26 which is in the range for usual two dimensional materials. This means that when the material is compressed in one direction, it will expand in the other direction as well. The in-plane stiffness value is for C_2P is calculated (6.69 eV/\AA^2) with a corresponding Poisson ratio of 0.21, which means that the C_2P crystal is less responsive than C_2N under compression. The lowest in-plane stiffness for the C_2As monolayer is 5.83 eV/\AA^2 with the corresponding Poisson ratio of 0.21 which is equal to that of the C_2P crystal. All the holey monolayers have Poisson ratios which are larger than that of graphene and close to that of h-BN.

We next consider the behavior of the monolayer structures under higher values of uniform strain ranging from 0.04 to 0.40. For this purpose the calculations are performed in a 2×2 supercell. The change of strain energy of all the monolayers under applied biaxial strain is given in Fig. 4.4(a). Although C_2N is the stiffest crystal, structural deformations start to form beyond 12% strain which is small compared to those of C_2P and C_2As . By structural deformation we mean that the N atoms connecting the C pairs start to form C_4N_2 isolated hexagonal rings. The distance between two neighboring C atoms in different hexagonal rings become 1.79 \AA at 12% strain. This distance increases up to 3.10 \AA at 40% strain. The deformation path seems to be the same for the C_2P monolayer structure. Up to a strain value of 20%, P atoms are still bonded to the hexagonal C rings and there is no drastic change in the structure of the monolayer. However beyond 20% strain hexagonal rings are formed composed of 4-C and 2-P atoms as in the case of C_2N . The C-C bond lengths in C pairs are approximately 1.30 \AA at 20% strain and there exist C-C pairs connected by P atoms as shown in Fig. 4.4(c). Among the monolayer structures considered, only in the C_2As crystal the hexagonal C rings preserve their form under large strains. The bond angle of C-As-C bond gets larger as the applied strain is increased. As given in Fig. 4.4(d), at 24% strain this angle becomes 158 degrees and there is no longer bonding between the C and As atoms. Compared with the other two structures, C_2As has the smallest in-plane stiffness value and it is the softest material among the three monolayers. The C_2X monolayer structures can be viewed as an ordered phase of 6-C rings linked by the X atoms. It seems that the linker atoms N and P have stronger bonds to their C neighbors so that the structure dissociates into isolated rings by breaking the C-C bonds under high strain. For As, however, the C-C bonds must be stronger than the C-As bonds so that the crystal yields at the linker sites.

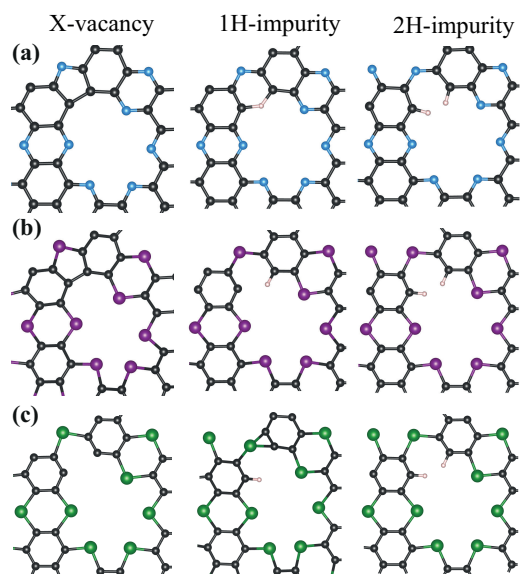


Figure 4.5. Optimized X-vacancy and their H substituted structures of (a) C_2N , (b) C_2P , (c) C_2As respectively.

4.4. Effect Of Defects

Considering the synthesis procedure of the mentioned holey crystals in which the ingradient molecules are self-assembled, the atomic scale disorders like vacant N, P and As sites are the most probable disorders in C_2N , C_2P and C_2As monolayers, respectively. The existence of H-impurities at these vacant-sites are also possible since the C_2N holey structure is synthesized as a result of the interactions of hexaaminobenzene and hexaketocyclohexane molecules which contain H atoms in their composition. In this section, we investigate the effects of these vacant sites and substitutional H-impurities on the geometric and the electronic properties of the monolayer holey structures.

Optimized geometries of the defected structures are shown in Fig. 4.5. For the N-defected C_2N and P-defected C_2P holey crystals (Figs. 4.5(a) and (b)), removal of a single N or P atom results in a bond formation between the two C atoms at the vacant site. However, in the case of As-defected C_2As the optimized geometric structure does not lead to an additional bonding (see Fig. 4.5(c)). Geometry optimizations indicate that for X-vacant structures only the C_2N retains its planar geometry while the other two structures get buckled. Our Bader analysis shows that charge depletion of $1.1 e$ per atom occurs from the C atoms to the neighboring N atoms in N-defected C_2N . For P-defected C_2P , an average of $0.6 e$ charge is transferred to each C atom except for the two C atoms

at the vacant sites since these C atoms keep approximately their initial charges. For As-defected C_2As the charge is depleted to the C atoms with a value of $0.3 e$ per atom on the average. We found that the N-defected C_2N has a nonmagnetic ground state while P-defected C_2P and As-defected C_2As have magnetic ground states with a net moment of $1 \mu_B$. Total DOS calculations indicate that X-missing structures of C_2N and C_2P become metallic monolayers while the As-defected C_2As is still a semiconductor with a lower band gap energy than its perfect form (see Fig. 4.6(c)). Calculated cohesive energies per atom in the supercells demonstrate that for all three structures the highest E_{coh} occur for X-missing structures of C_2N and C_2P while for the C_2As monolayer most energetic case is 1H-impurity case as seen in Table 4.2.

Table 4.2. The calculated ground state properties of defected C_2X -structures, structural geometry, lattice parameters of 2×2 supercell, a and b , the net magnetic moment of the structure, μ , and the cohesive energy per atom in supercell E_{coh} .

	Geometry	a (Å)	b (Å)	μ (μ_B)	E_{coh} (eV)
N-vacant- C_2N	planar	16.44	16.44	0	6.77
P-vacant- C_2P	buckled	17.66	17.67	1	6.02
As-vacant- C_2As	buckled	19.27	19.27	1	5.61
1H-imp.- C_2N	planar	16.63	16.63	0	6.71
1H-imp.- C_2P	buckled	18.37	18.15	0	5.97
1H-imp.- C_2As	buckled	18.37	19.04	0	5.65
2H-imp.- C_2N	planar	16.79	16.79	1	6.67
2H-imp.- C_2P	planar	18.71	18.71	1	5.93
2H-imp.- C_2As	planar	19.46	19.45	1	5.58

As seen in Fig. 4.5(a), the C_2N structure having a single H substitution at the N-vacant site preserves the geometry of C_2N monolayer. The geometries of other two monolayers with 1H-impurity get buckled as seen in Fig. 4.5. The result of the Bader analysis for all three monolayers for 1H-impurity case show that $0.1 e$ of charge is transferred to the C atom at the vacant site from H atoms. The inclusion of single H-impurity gives rise to a non-magnetic ground state for all C_2X monolayers as in their bare cases. For 1H-impurity structures the total DOS calculations indicate that all three monolayers preserve their semiconducting character but with lower values of band gap energies (see Fig. 4.6).

In our study, inclusion of 2H-impurities at the X-vacant sites is also considered. In all three defected structures each H atom binds to a single C atom as expected (see Fig.

4.5). Addition of the second H atom to the vacancy sites restores the planar geometry of all three monolayers. In this case, the charge is donated to each C atom at the vacant site from the H atoms such that the final charges on C atoms are the same as their values in the perfect crystals. 2H impurities result in a magnetic ground state for all three monolayers with a $1 \mu_B$ of net magnetic moment. The total DOS calculations demonstrate that inclusion 2H-impurities in C_2X structures preserves the semiconducting behaviors of the three monolayers with lower band gap energies (see Fig. 4.6). The corresponding cohesive energies per atom are also given in Table 4.2 which indicate that the C_2N monolayer has the highest E_{coh} than that of C_2P and C_2As monolayers.

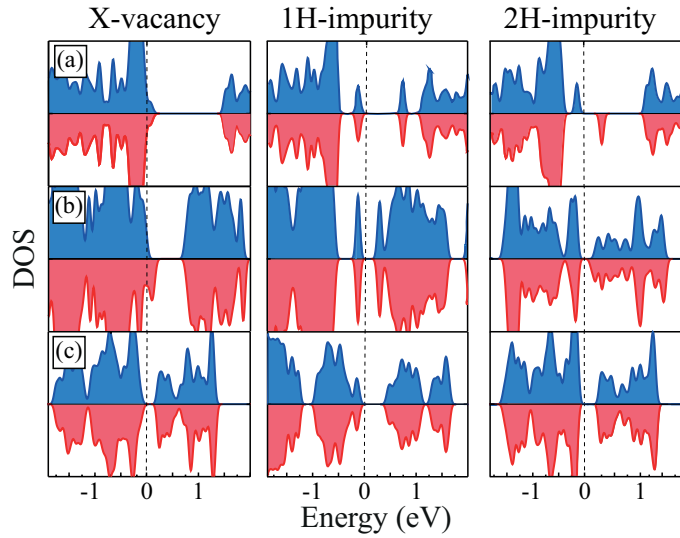


Figure 4.6. Total DOS for defected and H-impurity structures of (a) C_2N , (b) C_2P , and (c) C_2As respectively.

4.5. Conclusion

Motivated by recent experiments on the C_2N monolayer and graphene-like COF networks, we investigated structural, mechanical and electronic properties of two other monolayer structures, C_2P and C_2As . We found that C_2N has the highest E_{coh} among the three monolayers and the calculated values of E_{coh} are comparable with that of graphene and h-BN. Moreover, it is calculated that, the workfunction values of the monolayers are decreasing from C_2N to C_2As which is consistent with the trend in ionization energy of each element. Energy-band structure calculations show that the holey monolayers are

direct band gap semiconductors. Our calculations on mechanical constants suggest that the stiffest material is the C_2N structure with the highest Poisson ratio among the three monolayers. Moreover, the vacancy defects of N and P atoms in holey structures lead to metallic ground states while the substitutional H-impurities do not change their semiconducting character but can create net magnetization on the monolayer. Finally, we point out that holey graphene monolayers are new two dimensional materials that are mechanically stable and they are flexible semiconductors which may be favorable for applications in optoelectronics.

CHAPTER 5

FLEXIBLE MONOLAYERS OF GA-MONOCHALCOGENIDES (GAS AND GASE)

GaS and GaSe structures are layered semiconductors in their bulk form possessing direct or indirect gap character depending on the type of chalcogenide atom. They consist of weakly bound atomic thin layers in which there are two sheets of Ga layers sandwiched between chalcogenide layers (in order of X-Ga-Ga-X, where X=S or Se). The intralayer bonding of PTMCs has strong covalent character while the interlayer interaction has weak vdW character. Bulk GaSe crystal was reported to be a direct-gap semiconductor with band gap of 2.0 eV while bulk GaS was found to be an indirect-gap semiconductor with a band gap of 2.4 eV (Tatsuyam.C *et al.*, 1970; Yamamoto *et al.*, 2001). In recent years large area ultrathin layers of GaS and GaSe crystals were successfully synthesized on SiO₂/Si substrates by using micromechanical cleavage technique (Late *et al.*, 2012; Ho *et al.*, 2006; Aono *et al.*, 1993; Hu *et al.*, 2012). Chen *et al.* studied theoretically the electronic and magnetic properties of substitutionally doped monolayer GaS and found that the N atom is the most promising candidate for *p*-type doping among non-metal and transition metal dopants. They also investigated the electronic and magnetic properties of native defects in GaS monolayer and found a half-metallic behavior for Ga vacancy (Chen *et al.*, 2015a,b). Li *et al.* studied the interlayer orientations and stackings of 2D bilayer GaSe crystals and reported that the rotational energy barriers increase as the size of the system increases (Li *et al.*, 2015). Moreover, Zhou *et al.* studied the second harmonic generation in layered GaSe crystals and found that the strongest second-harmonic generation intensity is observed for GaSe among all 2D crystals (Zhou *et al.*, 2015).

Although the electronic, magnetic and optical properties of monolayer GaS and GaSe crystals have been studied extensively, their mechanical properties are still unknown. Therefore, we comparative study of the mechanical properties of single layer crystal structures of GaS, GaSe, graphene and MoS₂ in terms of their elastic constants. In addition, the effect of charging the system on the mechanical properties of monolayer GaS and GaSe are investigated.

The chapter is organized as follows: Structural and electronic properties of monolayers of graphene, MoS₂, GaS and GaSe are presented in Sec. 5.1. In Sec. 5.2, the mechanical properties of these monolayers and the effect of charging on their elastic constants are discussed in detail. Finally, we conclude in Sec. 5.3.

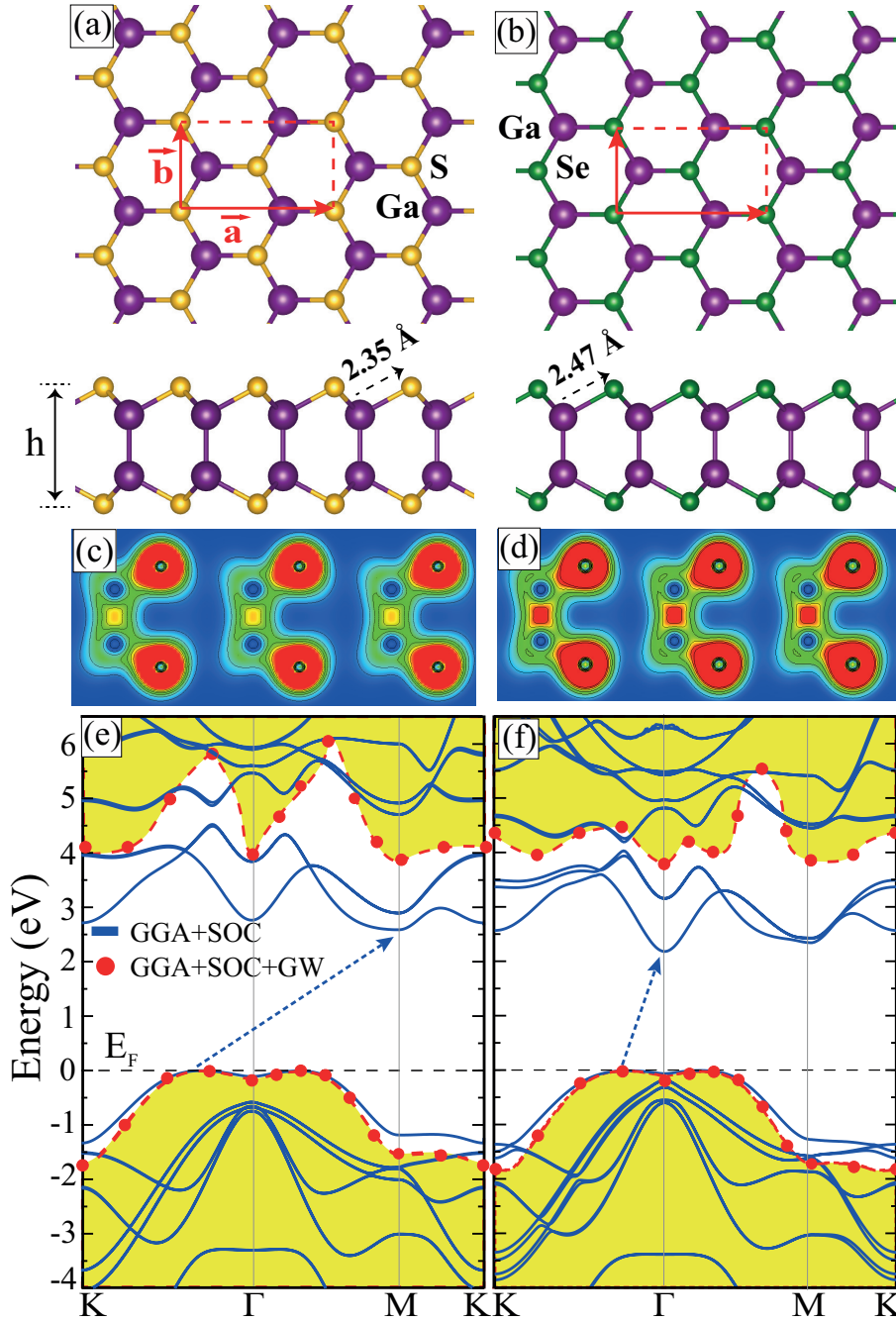


Figure 5.1. Top and side view of monolayer (a) GaS and (b) GaSe. Red dashed lines represent the rectangular unit cell and a and b are the lattice vectors. h is the thickness of the monolayer GaS and GaSe crystals. The charge distribution on the individual atoms for monolayer (c) GaS and (d) GaSe are shown in side view. Increasing charge density is shown by a color scheme from blue to red with linear scaling between zero (blue) and $6.7 e/\text{\AA}^3$ (red). (e) and (f) show the calculated energy-band structure within GGA+SOC and GGA+SOC+GW approximations for monolayer GaS and GaSe, respectively. The Fermi energy (E_F) level is set to the valence band maximum. The red dashed lines indicate the GW band structure while blue lines indicate the indirect GGA+SOC band structure.

Table 5.1. The calculated ground state properties of monolayer graphene, MoS₂, GaS and GaSe crystals: proper thickness h_p , magnetic state, the amount of charge received by the a chalcogenide atom $\Delta\rho$, calculated energy band gap within GGA (E_g^{GGA}), SOC (E_g^{SOC}), GW (E_g^{GW}), and workfunction Φ , in-plane stiffness C, Poisson ratio ν , ultimate strength σ_U , ultimate strain ε_U , and fracture strain ε_F .¹ (Shi *et al.*, 2013)

	h_p (Å)	Magnetic State	$\Delta\rho$ (e)	E_g^{GGA} (eV)	E_g^{SOC} (eV)	E_g^{GW} (eV)	Φ (eV)	C (N/m)	ν -	σ_U (GPa)	ε_U (%)	ε_F (%)
Graphene	3.35	NM	-	-	-	-	4.40	330	0.19	96	20	26
MoS ₂	6.15	NM	0.5	1.64	1.56	2.80 ¹	5.88	122	0.26	26	22	24
GaS	7.76	NM	0.8	2.59	2.59	3.88	6.10	91	0.26	12	24	29
GaSe	7.96	NM	0.6	2.21	2.18	3.68	5.59	77	0.25	10	23	30

The optical band gaps of monolayer GaS and GaSe were calculated by solving the Bethe-Salpeter equation (BSE) on top of the GW (G_0W_0) calculation including the spin-orbit coupling (SOC). For these calculations $6 \times 6 \times 1$ Γ centered \mathbf{k} -point sampling was used and 160 bands were included in our calculations. The cutoff energy for the plane-waves was chosen to be 400 eV.

5.1. Structural and electronic properties

Monolayers of GaS and GaSe crystals consist of 4-atom-layers in the order X-Ga-Ga-X (see Figs. 5.1(a) and 5.1(b)) where X stands for S or Se atoms. The calculated lattice parameters are 3.58 and 3.75 Å for monolayers of GaS and GaSe structures, respectively. These results are compatible with the calculated Ga-X bond lengths i.e. 2.35 and 2.47 Å for the Ga-S and Ga-Se bonds, respectively (2.41 Å for Mo-S bond in monolayer MoS₂). The thickness of the monolayers were calculated to be 4.66 and 4.82 Å for GaS and GaSe, respectively. In both monolayers charge donation occurs from Ga to chalcogenide atoms. In monolayer GaS each Ga atom donates 0.8 e to each S atom which indicates the strongly ionic character of the Ga-S bond see Fig. 5.1(c). As seen in Fig. 5.1(d), the amount of charge depletion from Ga to Se atoms decreases to 0.6 e per atom in monolayer GaSe which indicates the mostly covalent character of the Ga-Se bond. This because of the charge depletion between Ga atoms which is seen by small red area in Fig. 5.1(d). The work function values were calculated as 6.10 and 5.59 eV for GaS and GaSe, respectively. The work function of monolayer MoS₂ is smaller than that of monolayer GaS with the value of 5.88 eV. Monolayer GaSe has a work function of 5.59 eV which is lower than that

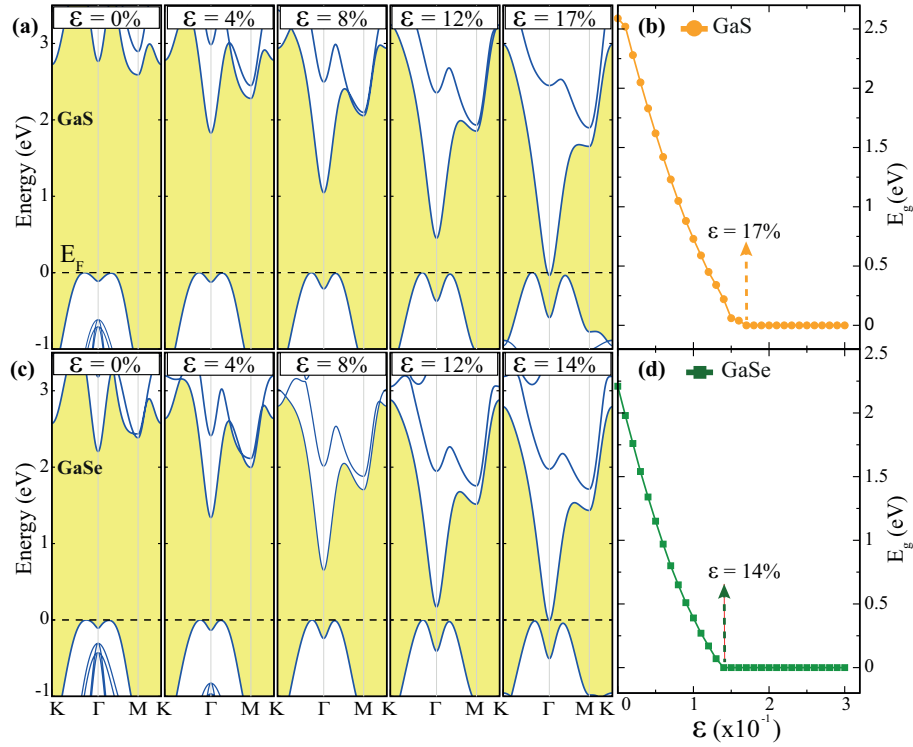


Figure 5.2. Calculated energy-band structures within GGA for different applied strain values for monolayer (a) GaS and (c) GaSe. The Fermi energy (E_F) level is set to the VBM of each structure. The change in the band gap with applied strain for monolayer (b) GaS and (d) GaSe.

of GaS due to the higher ionizations energy of S atom as compared to the Se atom. For both of the monolayers, work functions decrease upon charging the structures. When $0.1 e$ per primitive cell is added, extra charges accumulate to p_z orbitals of chalcogenide atoms. Thus, work function shows a rapid decreasing since it is calculated from the surface of the material. However, when $0.1 e$ per primitive cell is added, now the extra charges are depleted to inside the monolayers. Therefore, the work function shows a decreasing with small amount of energy difference. In addition, charging the structures expands the lattice and thus, the lattice constant tend to increase upon charging. The cohesive energy decreases for larger structures. Therefore, the cohesive energies show decreasing trend upon charging the system.

Although they exhibit different semiconducting characters in their bulk forms, monolayers of GaS and GaSe are indirect bandgap semiconductors. Their valence band maximum (VBM) lies between the K and Γ points in the Brillouin Zone (BZ). However, it is important to note that the valence band edge in between Γ and M points differs only

by 6 meV energy than VBM of the monolayers. The conduction band minimum (CBM) resides at the M point in monolayer GaS while it resides at the Γ point in monolayer GaSe (see Figs. 5.1(e) and (f)). The calculated GGA+SOC band gaps are 2.59 and 2.18 eV for monolayer GaS and GaSe, respectively. These values of the band gap will increase when we perform GW calculation within SOC. Our calculated GW band gaps are 3.88 and 3.68 eV for monolayer GaS and GaSe, respectively.

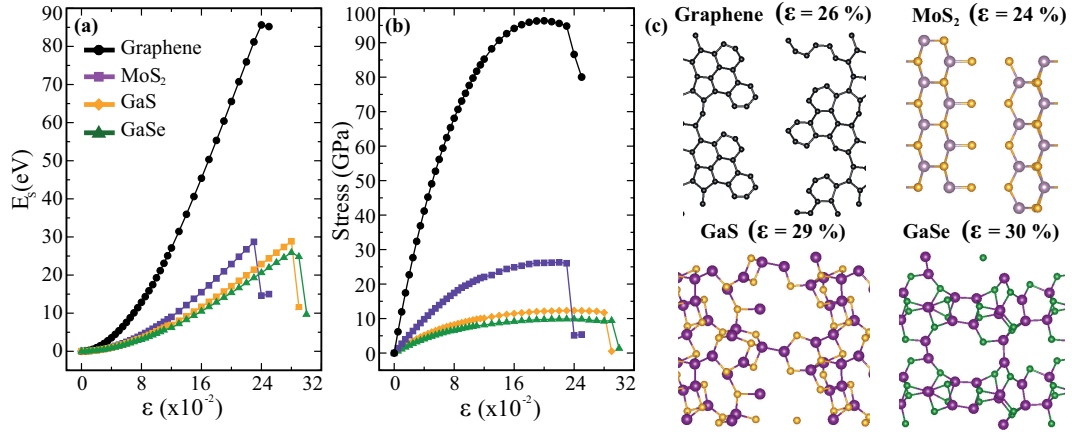


Figure 5.3. (a) The change of strain energy and (b) the created stress in the different monolayer materials under applied biaxial strain. (c) The geometries of each monolayer crystals at fracture strain values.

Before the detailed investigation of the mechanical characteristics of monolayer GaS and GaSe, we show how the electronic structure responds against applied biaxial strain. In order to investigate the response of the electronic band structure of the monolayers to applied biaxial strain, we considered the BZ of the rectangular unit cell shown in Fig. 5.2. As seen in Figs. 5.2(b) and (d), the band gap of the two monolayers decreases monotonously with increasing applied strain. Electronic band structure of GaS displays metallic behavior firstly at $\epsilon=17\%$. The indirect-gap character of GaS is not affected by the applied strain only the value of the gap decreases. As the applied strain increases, the energy difference between two valence band edges also increases. Similar shift in VBM of hexagonal Aluminium Nitride (h-AlN) was reported by Bacaksiz *et al.* (Bacaksiz *et al.*, 2015). The VBM of GaS consists of p_z orbitals of the Ga and S atoms. Thus, the out-of-plane orbitals are not affected by the applied in-plane strain. Differing from the atomic orbital character of VBM, CBM consists of both p_z orbital of S atom and p_x, p_y orbitals of Ga atom. The in-plane orbitals of Ga atom are strongly affected by the in-plane strain and thus, the energy of CBM decreases (see Fig. 5.2(a)). The same behavior of band struc-

ture can be seen in monolayer GaSe under applied biaxial strain. The metallic behavior of GaSe is first seen at $\varepsilon=14\%$ which is smaller than that of GaS. Although we reported the critical strain values for semiconductor-metal transition, it should be noted that these values depend also on the value of the band gap. If one considers the GW gaps or band gaps calculated within HSE06, critical strain values may be found to be higher. Since the VBM of GaSe consists of p_z orbitals of Ga and Se atoms, it is also unaffected by the applied strain. Only a small energy difference occurs between the valence band edges at K- Γ and Γ -M (6 meV). However, CBM of GaSe consists of s orbital of Ga and p_z and s orbitals of Se atoms.

5.2. Linear and Non-Linear Elastic Properties

The elastic properties of homogeneous and isotropic materials can be represented by two independent constants, the in-plane stiffness C and the Poisson ratio ν . To examine the brittleness or ductility of materials, the fracture strain values must be obtained from the stress-strain curve. In the following we mind a comparative investigation of the mechanical properties of monolayer GaS, GaSe, graphene and MoS₂ crystals in terms of these elastic constants.

For the determination of the elastic constants of the four different monolayer structures, the rectangular unit cell shown in Fig. 5.1(a) was first optimized and then a 2×2 supercell (containing 32 atoms) was considered. The strains ε_x and ε_y were applied to the monolayer crystals by varying the lattice constants along the x and y directions. The strain parameters ε_x and ε_y were varied between ± 0.02 with a step size of 0.01. For this purpose three different sets of data were calculated; (i) $\varepsilon_y=0$ and ε_x varying, (ii) $\varepsilon_x=0$ and ε_y varying and (iii) $\varepsilon_x=\varepsilon_y$ varying. At each configuration, the atomic positions were fully relaxed and the strain energy, E_S , was calculated by subtracting the total energy of the strained system from the equilibrium total energy. The calculated data was fitted to the equation $E_S = c_1\varepsilon_x^2 + c_2\varepsilon_y^2 + c_3\varepsilon_x\varepsilon_y$, and the coefficients c_i were determined.

5.2.1. In-plane Stiffness

The in-plane stiffness, C , is a measure of the rigidity or the flexibility of a material and depends on the geometry of the considered structure. Graphene is known to be the stiffest material among the 2D monolayers. The value of C can be calculated by the

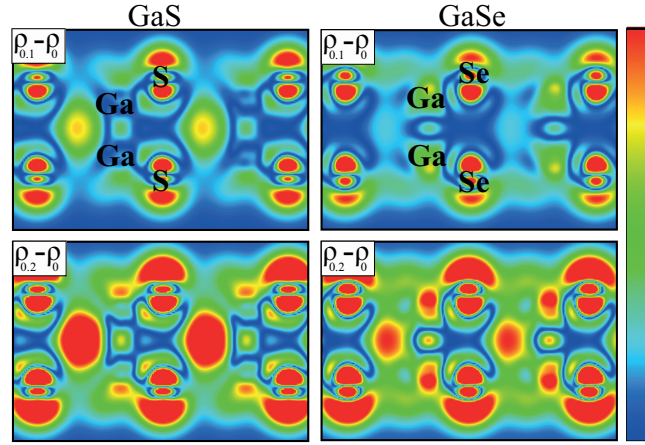


Figure 5.4. Total charge density difference between the bare and 0.1 charged ($\rho_{0.1}-\rho_0$), and 0.2 charged ($\rho_{0.2}-\rho_0$) cases for monolayer GaS and GaSe. Increasing charge density is shown by a color scheme from blue to red with linear scaling between zero (blue) and maximum charge (red).

formula $C = (1/A_0)(2c - c_3^2/2c)$ where we let $c_1=c_2=c$ due to the isotropy of the unit cell and A_0 is the strain-free area of the supercell. To understand the flexibility of monolayer GaS and GaSe, it is meaningful to compare their in-plane stiffness with that of well known 2D materials, as graphene and MoS₂. Our calculated in-plane stiffness values are 91 and 77 N/m for GaS and GaSe, respectively which are close to the value for MoS₂ (122 N/m), but lower than that of graphene (330 N/m). Our results for graphene and MoS₂ are consistent with the reported experimental values (Bertolazzi *et al.*, 2011b; Lee *et al.*, 2008). Although monolayer GaS and GaSe have much lower in-plane stiffness values than graphene, they are stiffer than silicene and germanene (Sahin *et al.*, 2009). The difference in the in-plane stiffness values between two Ga-chalcogenides can be explained through the lattice constants and cohesive energies of two monolayers. The lattice constant of GaS is smaller than that of GaSe and parallel to ionizations energies of chalcogenide atoms, the cohesive energy per atom is higher for GaS (these two parameters, lattice constant and cohesive energy, are also in good agreement). However, when we compare the two monolayers with the same chalcogenide atom, S, monolayer MoS₂ is stiffer than monolayer GaS. This can be understood when the total charge densities are analyzed; the electrons are mostly localized on the S atom in GaS while they are shared between Mo and S atoms in monolayer MoS₂ which indicates the more covalent bond characters in MoS₂.

As seen in Figs. 5.5(a) and (b), in-plane stiffness decreases with increasing lattice constant and the cohesive energy per atom. This is expected because a smaller lattice

constant means a smaller bond length between the individual atoms which indicates a higher in-plane stiffness. In contrast, as seen in Fig. 5.5(c), in-plane stiffness decreases with increasing work function. The work function of a material is proportional to the ionization energy of individual atoms in the material. So higher ionization energy means higher work function which correlates with the higher in-plane stiffness.

In order to tune the elastic properties of monolayer GaS and GaSe crystals, extra electrons were added to the monolayers. We considered two different amounts of charges, 0.1 and 0.2 e/cell , respectively. For monolayer GaS, we find that the in-plane stiffness decreases to 58 and 56 N/m for 0.1 and 0.2 e/cell charging. In the case of monolayer GaSe, the trend in the in-plane stiffness is the same. The 0.1 and 0.2 e/cell -charged cases decrease the value of C to 54 and 46 N/m, respectively.

As shown in Fig. 5.4 when 0.1 e/cell is added, the extra charges are depleted to the p_z orbitals of S and Se atoms in both monolayers. Therefore, following the increase in Ga-X bond lengths, the in-plane stiffness shows a sharp decrease with 0.1 e charging. However, GaS and GaSe have a different behavior for further charging. Our charge density difference analysis shown in Fig. 5.4 reveals that for 0.2 e/cell charged GaS, the additional charges are donated to both in-plane and out-of-plane orbitals (see Fig. 5.4) However, in the case of monolayer GaSe additional charges are accumulated mostly to out-of-plane orbitals of the Se atoms. Therefore, in-plane-located extra charges of GaS makes it stiffer than GaSe even at 0.2 e charging and decrease in in-plane stiffness of GaS is less than GaSe.

5.2.2. Poisson Ratio

The mechanical response of a material to an applied stress is called the Poisson ratio. It is also defined as the ratio of the transverse contraction strain to the longitudinal extension strain in the direction of the stretching force, that is $\nu = -\varepsilon_{trans}/\varepsilon_{axial}$. The Poisson ratio was obtained as $\nu = c_3/2c$. Due to the symmetry of the honeycomb lattice, the elastic constants were found to be the same along the x and y directions. Calculated Poisson ratio values for GaS and GaSe are 0.26 and 0.25, respectively, which are nearly the same as that of monolayer MoS₂ (0.26) but larger than that of graphene (0.19). This means that GaS and GaSe crystals are more sensitive to applied uniaxial strain. Indeed, for the same applied uniaxial strain, a longer is found contraction in the perpendicular direction to the applied strain direction.

In connection with the value of C in the absence of charging, the Poisson ratio

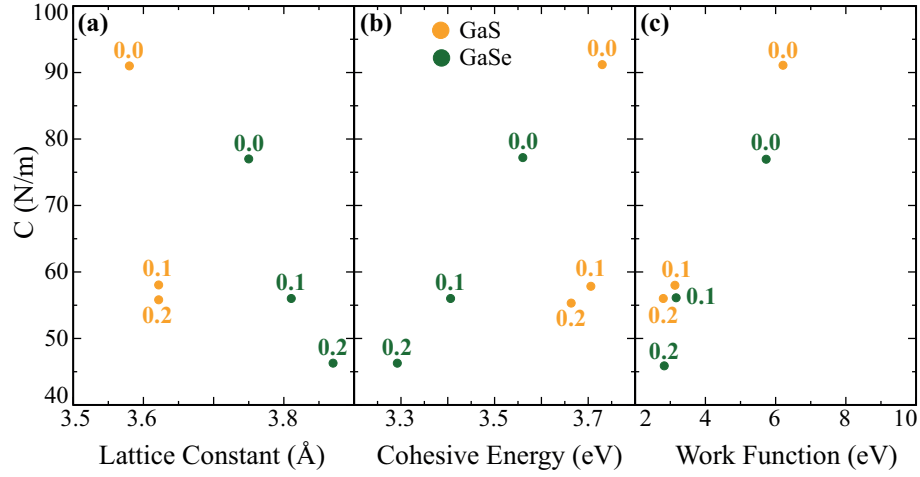


Figure 5.5. In-plane stiffness values: (a) lattice constant, (b) cohesive energy per atom, and (c) work function of monolayer GaS and GaSe crystals. The number near the symbols gives the amount of added charge per unit cell.

of the monolayer is also strongly affected. When the monolayer GaS is charged, it becomes more flexible as mentioned and the corresponding Poisson ratio value increases. This situation is expected because a flexible material can contract much smaller in the transverse direction when stretched along the axial direction. We found ν to be 0.43 and 0.39 for GaS and 0.36 and 0.33 for GaSe under 0.1 and 0.2 e /cell charging, respectively. Opposite to the trends in C , the Poisson ratio value first increases under charging by 0.1 e /cell and then decreases under charging by 0.2 e /cell. But in both cases the Poisson ratio is higher than those for bare monolayers. When the structures are charged, monolayers become more flexible which indicates more extension of the lattices under small uniaxial strains. Thus, the Poisson ratio values demonstrate a rapid increase because of the lattice expansion under charging.

5.2.3. Ultimate Strength

The ultimate strength is the maximum value of stress that a material can resist before the fracture point. This value can be directly investigated from the maximum point of the stress-strain curve of a material. For this purpose, large biaxial strain was applied to the monolayers up to the value of $\varepsilon=0.40$. As seen in Fig. 5.3(b), monolayer GaS and GaSe have much lower ultimate strength values than that of graphene and monolayer

MoS₂. Our results indicate that monolayer GaS has $\sigma_U=12$ GPa which is higher than that of monolayer GaSe which is calculated to be 10 GPa as given in Table 5.1. The very high value of σ_U for graphene is due to the very strong sp^2 C-C bonds. Although, these two monolayers have lower σ_U , they can resist higher values of applied biaxial strain than graphene and MoS₂. The calculated ultimate strains for GaS and GaSe are $\varepsilon_U=0.24$ and $\varepsilon_U=0.23$, respectively. They are calculated to be $\varepsilon_U=0.20$ and $\varepsilon_U=0.22$ for graphene and MoS₂, respectively. These values indicate that Gas and GaSe crystals are more ductile than graphene. In addition, monolayers of GaS and GaSe crystals have high values of fracture strain as seen in Fig. 5.3(b). ε_F values were calculated as 0.29 and 0.30 for GaS and GaSe which are larger than that of graphene (0.26) and monolayer MoS₂ (0.24).

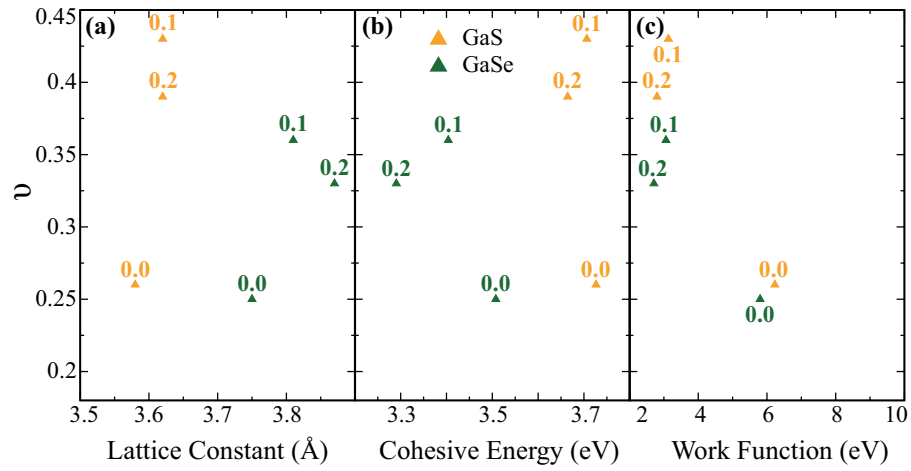


Figure 5.6. Poisson ratio values: (a) lattice constant, (b) cohesive energy per atom, and (c) work function of monolayer GaS and GaSe crystals. The numbers above the symbols refer to the amount of added charge per unit cell.

5.2.4. Dynamical Instability

The stress-strain relation can be used for extracting many mechanical parameters for a material. In order to calculate these mechanical constants and to determine the mechanical characteristics, we plot the theoretical stress-strain relation under applied biaxial strain. To compute the stress-strain relationship, a series of incremental tensile strains are applied to the monolayers. The maximum stress point of a stress-strain curve is critical for determining the fracture strain point of the material. Beyond that point, the structure

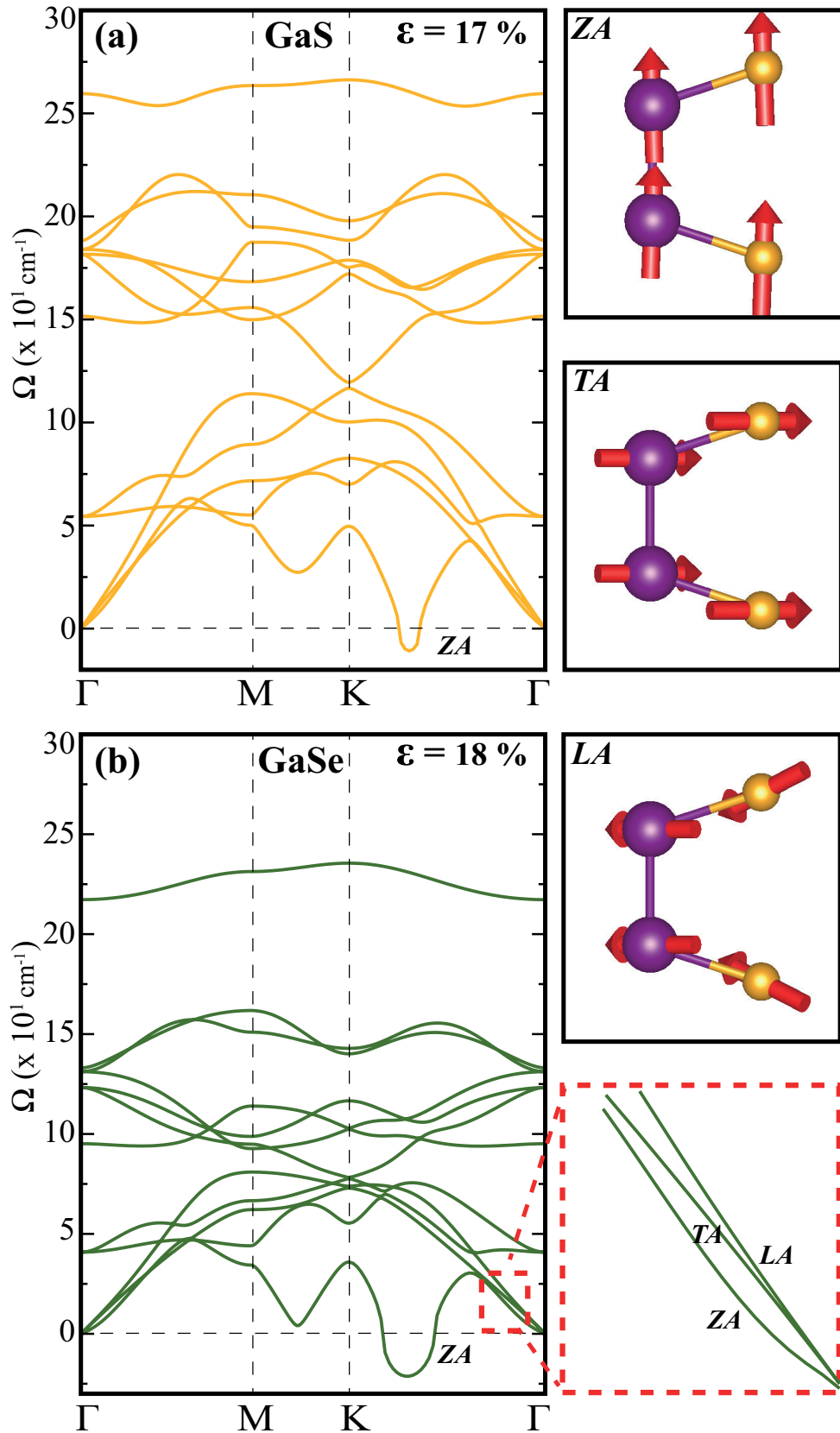


Figure 5.7. Phonon-band dispersions for monolayer (a) GaS at 17% and (b) GaSe 18% biaxial strains. The three acoustic phonon modes are given on the right panel.

becomes elastically unstable by fracture. However, this does not mean that the material remains dynamically stable up to the fracture point at the stress-strain curve. When phonon frequencies were calculated for monolayer GaS and GaSe under biaxial strain, we found that GaS and GaSe crystals are no longer dynamically stable after 17% and 18% biaxial strain values, respectively.

As seen from the Fig. 5.7, both monolayers undergo phonon instability which is dictated by an out-of-plane soft-mode. The instability occurs at the wave vector between the K and the Γ points. When related to the wavelength of this unstable acoustic phonon mode, the wave vector has a value of 0.804 1/\AA . Thus, higher value of the wave vector reveals the smaller value of the wave length for which the material has instability. In addition, we found that increased biaxial strain causes the region of unstable wave vectors to grow significantly before reaching elastically unstable strain point that correspond to the peak of the stress-strain curve. Here the underlying mechanism can be explained through the bond angles (X-Ga-X bond) in the upper and the lower Ga-X layers. As the applied biaxial strain is increased, this bond angle also increases and thus, the upper and lower Ga-X layers become more planar which softens the out-of-plane acoustic (ZA) mode of the monolayer structures. Similar to graphene and other 2D materials, phonon instability, that stems from the out-of-plane soft mode, occurs before the elastic instability in monolayer GaS and GaSe.

5.3. Conclusion

In conclusion, we have investigated the mechanical properties of novel 2D monolayer GaS and GaSe crystals in terms of in-plane stiffness, Poisson ratio and ultimate strength. We compare their values with those of graphene and monolayer MoS₂. Our results revealed that due to the more ionic character of the Ga-S bond as compared to the Ga-Se one, monolayer GaS is a slightly stiffer material than monolayer GaSe. Calculated stress-strain curves for each monolayer crystal indicates that they have smaller critical strength values than graphene and monolayer MoS₂ but higher ultimate strains. In addition, monolayer GaS and GaSe crystals have higher fracture strain values when compared to graphene and monolayer MoS₂ which is a signature of their ductility. By further analysis, decreasing trend in band gap values of monolayer GaS and GaSe crystals were found under biaxial strain at 17% and 14% for GaS and GaSe, respectively. Our results on charging the structures indicate that extra charges are depleted to the out-of-plane orbitals which expands the structures by repulsive interaction resulting in reduction of C values.

Our study reveals that single layer crystals of GaS and GaSe, together with their (i) high flexibility, (ii) high ductility, (iii) strain-dependent electronic behavior and (iv) charge tunable mechanical properties, are very promising materials for nanoscale electromechanical applications.

CHAPTER 6

HYDROGEN-INDUCED STRUCTURAL TRANSITION IN SINGLE LAYER ReS₂

Similar to other TMDs, the bulk forms of Re-dichalcogenides, ReSe₂ and ReS₂, were reported to be in a form of van der Waals layered structure. (Lamfers *et al.*, 1996; Wildervanck and Jellinek, 1971; Alcock and Kjekshus, 1965) Raman bands and their relative intensities depending on the number of layers and the layer-stacking-order were investigated for ReSe₂. (Wolverson *et al.*, 2014) Recently, Yang *et al.* showed that locally induced strain by generation of wrinkles in monolayer ReSe₂ modulates the optical gap, enhances light emission, induces magnetism, and modulates the electrical properties. (Yang *et al.*, 2015) The structural properties of bulk ReS₂ were studied by the X-ray diffraction experiments and the symmetry properties were reported (Wilson and Yoffe, 1969). Monolayer form of ReS₂ was successfully isolated and its unique properties such as a weak band-renormalization, absence of interlayer registry and weak interlayer coupling arising from Peierls distortion of the 1T structure were reported (Tongay *et al.*, 2014). It was also showed by Tongay *et al.* that the monolayer ReS₂ has a direct band gap of 1.55 eV which was confirmed by photoluminescence measurements (Tongay *et al.*, 2014). Pradhan *et al.* investigated the field-effect transistor performance of few-layer ReS₂. (Pradhan *et al.*, 2015) They found that ReS₂ on SiO₂ behaves as an *n*-type semiconductor at low electron densities *n*. For higher values of *n* the resistivity decreases, and a metallic behavior is observed. Yu *et al.* studied electronic properties of ReS₂ depending on applied strain and the number of layers. (Yu *et al.*, 2015) They reported that characteristics of the band structure and its band gap are insensitive to the applied strain. Moreover, the charge carrier mobilities were found to be nearly independent of the number of ReS₂ layers. Vibrational properties, especially the low frequency modes, of ReS₂ were studied to understand coupling of ReS₂ layers. He *et al.* studied the ultra low-frequency Raman spectra of ReS₂ and reported that the layers are coupled and orderly stacked in few layer ReS₂ (He *et al.*, 2016). In addition, the same analysis were reported by Lorchat *et al.* in terms of the calculated force constants between ReS₂ layers (Lorchat *et al.*, 2016). The optical properties of monolayer ReS₂ were also paid much attention due to strong anisotropy in the structure (Zhong *et al.*, 2015; Chenet *et al.*, 2015a; Aslan *et al.*, 2015). Zhong *et al.* (Zhong *et al.*, 2015) reported that the huge excitonic effects dominate the optical spectra of monolayer ReS₂ with an exciton binding energy of about 1 eV.

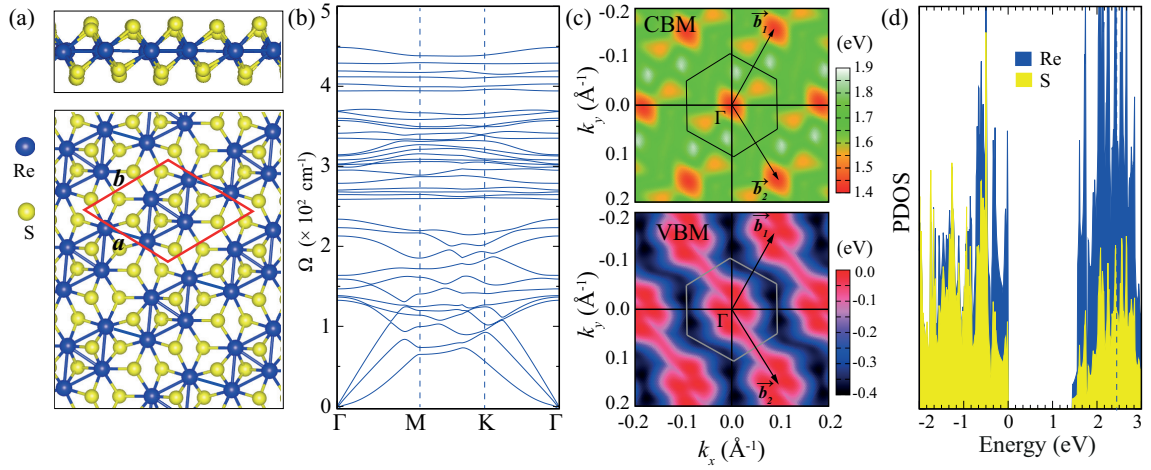


Figure 6.1. For the monolayer ReS_2 ; (a) top and side views of the structure, (b) the phonon-band structure, (c) VBM and CBM surfaces. (d) The corresponding partial density of states.

Tuning the physical properties of 2D materials became an important issue for their versatile use in next generation nanodevice technology. Surface functionalization of 2D monolayers with various types of atoms such as H, F, and Li, is one useful way to achieve that (Şahin *et al.*, 2011; Sahin and Peeters, 2013; Çakır *et al.*, 2014; Nasr Esfahani *et al.*, 2015). Among these atoms, H was widely used in experiments and considered also theoretically. For instance, it was first shown for graphene that hydrogenation of the sample bilaterally tunes the electronic properties significantly. Sofo *et al.* predicted a form of fully saturated hydrocarbon which they named as graphane. (Sofo *et al.*, 2007) They found that the graphane is a dynamically stable material with a comparable binding energy with other hydrocarbons such as benzene and cyclohexane. Following the study of Sofo *et al.*, two years later Elias *et al.* successfully synthesized graphane (Elias *et al.*, 2009) and observed that this new 2D material is an insulator. In addition, the transmission electron microscopy (TEM) measurements revealed that the graphane is a crystalline material and retains the hexagonal lattice. Moreover, it was reported that the reaction of graphene with hydrogen atoms is reversible which means graphene can be restored after annealing the graphane layer. In recent years, the hydrogenation of other novel 2D monolayers, such as TMDs, has come into prominence. Pan *et al.* investigated the electronic and magnetic properties of hydrogenated monolayer VTe_2 and found that the hydrogenated VTe_2 exhibits a transition from semiconductor to metal and further to half-metal under the effect of applied tension (Pan, 2014). Shi *et al.* studied the electronic and magnetic

Table 6.1. For the monolayer ReS_2 and $1\mathbf{T}^{Re_2}\text{-ReS}_2\text{H}_2$ structures; structure, calculated lattice parameters a and b , the average charge donation of a Re atom, $\Delta\rho$, the energy band gap of the structures calculated within; GGA (E_g^{GGA}), SOC on top of GGA (E_g^{SOC}), and the work function Φ .

Structure		a	b	$\Delta\rho$	E_g^{GGA}	E_g^{SOC}	Φ
		(Å)	(Å)	(e)	(eV)	(eV)	(eV)
ReS_2	$\text{Re}_4\text{-cluster}$	6.46	6.38	0.9	1.45(<i>d</i>)	1.34(<i>d</i>)	5.56
$1\mathbf{T}^{Re_2}\text{-ReS}_2\text{H}_2$	$\text{Re}_2\text{-dimer}$	7.46	6.65	0.7	0.60(<i>i</i>)	0.75(<i>i</i>)	2.47

properties of hydrogenated monolayer MoS_2 under applied biaxial strain and found that the ferromagnetic (FM) ground state occurs as the applied strain is increased (Shi *et al.*, 2013).

In this chapter, we investigate the structural phase transition in monolayer ReS_2 by full-surface hydrogenation. The new crystal structure, $1\mathbf{T}^{Re_2}\text{-ReS}_2\text{H}_2$, is found to be dynamically stable and it is an indirect semiconductor. In addition, the effect of hydrogenation on the mechanical properties is investigated. The chapter is organized as follows: Structural and electronic properties of monolayers of ReS_2 , single H-adsorbed ReS_2 , and $1\mathbf{T}^{Re_2}\text{-ReS}_2\text{H}_2$ are presented in Sec. 6.1. Mechanical properties of bare and hydrogenated monolayer crystals in terms of in-plane stiffness, C , effective Young modulus, E , Poisson ratio, ν , and bending rigidity, D are presented in Sec. 6.2. Finally, we conclude in Sec. 6.3.

6.1. Structural and Electronic Properties

6.1.1. Monolayer ReS_2

Differing from most of the TMDs having 1T or 1H phases, monolayer ReS_2 has a distorted crystal form named as 1T' phase (Tongay *et al.*, 2014) which corresponds to point group symmetry C_i . The primitive unitcell of 1T' phase is formed of eight S atoms coordinated around four-atom-cluster of Re (Re_4) as shown in Fig. 6.1(a). Our structural optimization confirms the 1T' phase of the monolayer ReS_2 as the ground state. As given in Table 6.1, the lattice parameters a and b are found to be 6.46 and 6.38 Å, respectively.

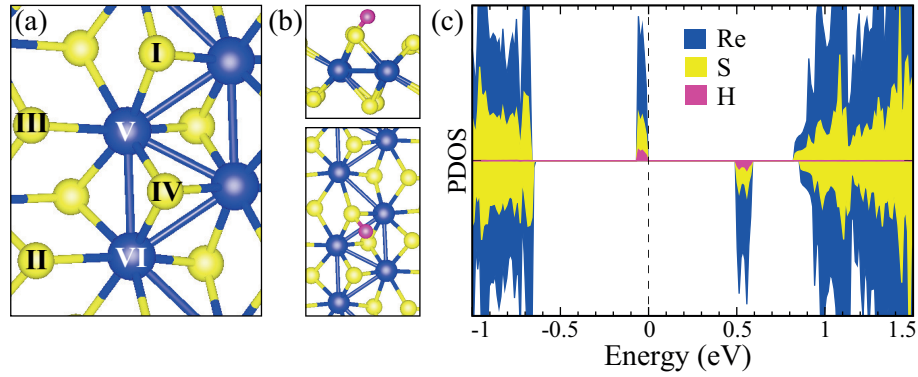


Figure 6.2. (a) Possible adsorption sites for a single H atom, labeled by numbers. (b) Top and side views of single H adsorbed monolayer ReS_2 and (c) the corresponding partial density of states (PDOS).

The Re-Re bond lengths in a Re_4 cluster are 2.81 and 2.71 Å for side and diagonal Re atoms, respectively. In addition, the Re-S bond length varies from 2.36 to 2.51 Å. Bader charge analysis reveals that the bond between Re and S is covalent-type with a charge depletion of 0.5 e from Re to S atom. The phonon analysis confirms that the monolayer ReS_2 is dynamically stable as shown in Fig. 6.1(b).

Electronic properties of the monolayer ReS_2 are also investigated. We find that it possesses a direct band gap of 1.45 eV calculated within GGA+SOC. As given in Fig. 6.1(c), we plot the highest of the valence band (VB) and the lowest of the conduction band (CB) energy levels as surfaces. The valence band maximum (VBM) and conduction band minimum (CBM) appear at the Γ point in BZ. The DOS calculation demonstrates that both VBM and CBM are dominated by the Re states.

6.1.2. Single H-atom Adsorption on Monolayer ReS_2

The adsorption of atoms to the surface of a material is an efficient way to tune their physical properties. For the 2D materials, H atom is widely used for such purposes. In regard to functionalize the monolayer ReS_2 , we first investigate the single H adsorption to the surface of the monolayer. In the unitcell, top of two Re and four S atoms are considered as the possible adsorption sites as shown in Fig. 6.2(a). Among these 6 different sites, the site-I is found to be the energetically favorable one with the bond length of 1.42 Å (see Fig. 6.2(b)). The binding energy of the H atom to the surface is calculated to be

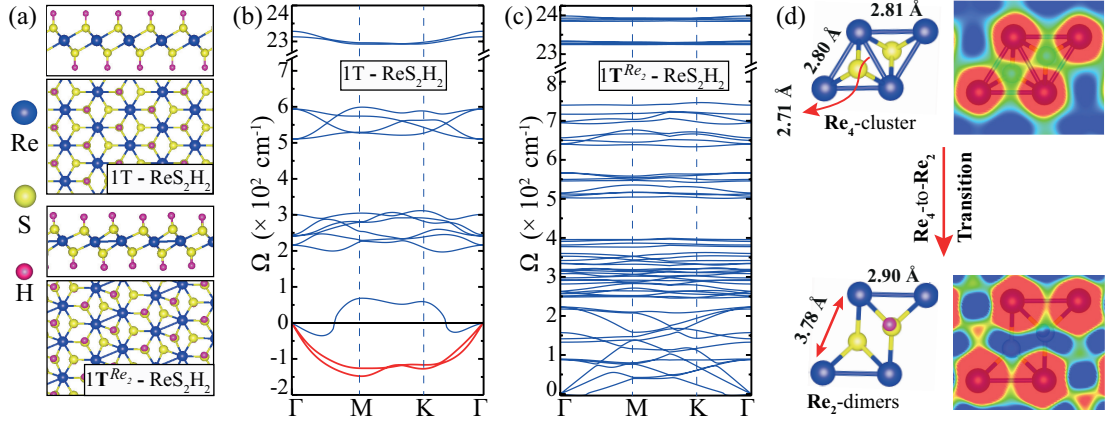


Figure 6.3. (a) Top and side views of monolayers of 1T-ReS₂H₂ (top panel) and 1T^{Re₂}-ReS₂H₂ (bottom panel). Corresponding phonon-band dispersions for (b) 1T ReS₂H₂ and (c) 1T^{Re₂}-ReS₂H₂. (d) The phase transition from Re₄ clusters in bare structure (on the left side) to Re₂ dimers in 1T^{Re₂}-ReS₂H₂ (on the right side) and the corresponding charge densities on the same Re-planes.

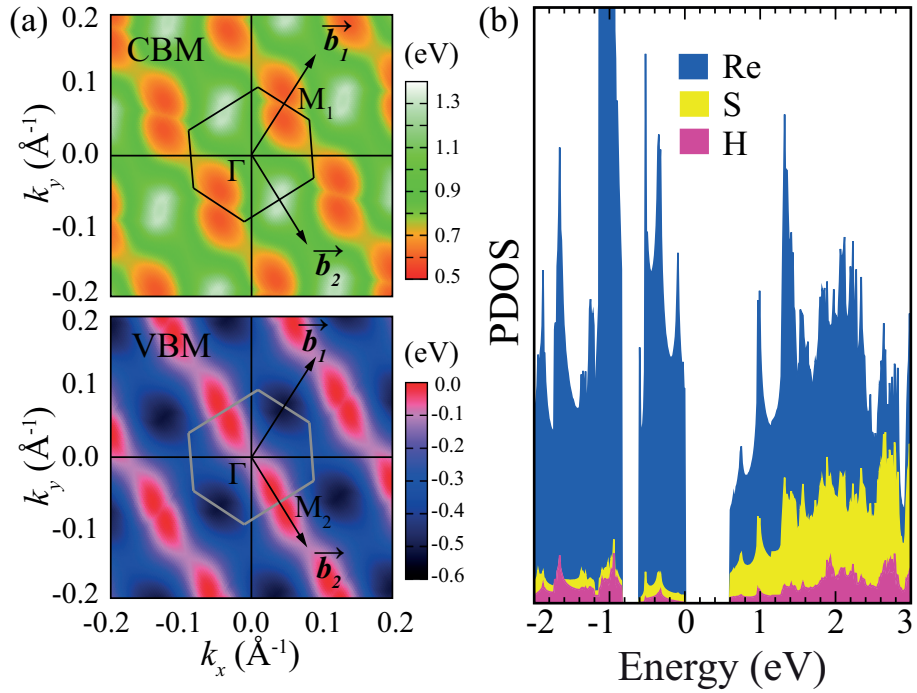


Figure 6.4. For the monolayer 1T^{Re₂}-ReS₂H₂; (a) VBM and CBM surfaces and (b) the corresponding partial density of states.

0.81 eV which is smaller than that of on graphene (0.98 eV) (Sahin and Ciraci, 2012). The single H adsorption leads to mid-gap states which appear at 0.5 eV above the VBM as shown in Fig. 6.2(c). The contributions to those mid-gap states are mainly from the Re atoms and relatively small contributions also exist from the S and H atoms. A net magnetic moment of $1 \mu_B$ appears at the vicinity of the H bonding site.

6.1.3. Full-Hydrogenation of Monolayer ReS₂

Following the analysis of the single H adsorption, we investigate the full-surface hydrogenation of the monolayer ReS₂. The full hydrogenation refers to that all the S sites are occupied by H atoms as shown in Fig. 6.3(a). The H atoms prefer to bind perpendicular to the surface plane instead of being inclined as in single H case. The full hydrogenation expands the lattice such that the parameters a and b increase to 7.46 and 6.65 Å, respectively. The most significant change in the structure is that a Re₄ cluster is broken into two Re₂ dimers as shown in Fig. 6.3(d). In this new structure which we name as $1\mathbf{T}^{Re_2}$ -ReS₂H₂, the Re-Re bond length increases to 2.90 Å, however, the Re-S bonds do not change significantly. The Bader charge analysis shows that each H atom is donated 0.1 e charge. In addition, the calculated phonon-band structure reveals the dynamical stability of monolayer $1\mathbf{T}^{Re_2}$ -ReS₂H₂ as shown in Fig 6.3(c). Although, the crystal structure of monolayer $1\mathbf{T}^{Re_2}$ -ReS₂H₂ resembles the perfect 1T phase, the hydrogenated perfect 1T phase is not dynamically stable (see Fig. 6.3(b)). Thus, it is clearly seen that the formation Re₂ dimers contribute to the dynamical stability of $1\mathbf{T}^{Re_2}$ -ReS₂H₂.

The hydrogenation also modifies the electronic properties significantly. In Fig 6.4(a), the surface plots of the VBM and CBM are shown and it is found that the $1\mathbf{T}^{Re_2}$ -ReS₂H₂ is an indirect semiconductor. Its band gap is 0.75 eV which is approximately half of that of monolayer ReS₂. The band extrema points do not appear at the ordinary symmetry points. The VBM of the monolayer resides between Γ and M₂ points along b_2 vector while the CBM lies between Γ and M₁ points along b_1 vector. As seen from the partial density of states (PDOS) in Fig. 6.4(b), the domination of Re states at the VBM and CBM persists.

In addition, for further examination of the stability of the monolayer ReS₂ and $1\mathbf{T}^{Re_2}$ -ReS₂H₂ structures, we perform molecular dynamics (MD) simulations under gradually increasing temperature. We consider two sets of calculations; in the first set, the temperature of each structure is increased from 0 to 800 K in a time interval of 0-16 ps,

Table 6.2. Elastic parameters along \perp - (perpendicular to Re_4 chains) and \parallel -directions (parallel to Re_4 chains) for the monolayers of ReS_2 and $1\mathbf{T}^{\text{Re}_2}\text{-ReS}_2\text{H}_2$ structures; calculated in-plane stiffness C_{\perp} and C_{\parallel} , Poisson ratio ν_{\perp} and ν_{\parallel} , effective Young modulus E_{\perp} and E_{\parallel} .

	C_{\perp} (J/m^2)	C_{\parallel} (J/m^2)	ν_{\perp} -	ν_{\parallel} -	E_{\perp} (GPa)	E_{\parallel} (GPa)
ReS_2	166	159	0.19	0.19	497	477
$1\mathbf{T}^{\text{Re}_2}\text{-ReS}_2\text{H}_2$	128	97	0.38	0.29	329	250

and we find that both structures remain stable as shown in Figs. 6.5(a) and (c). In the second set, the temperatures are increased from 700 to 1500 K in the time interval of 0-20 ps for each structure. For the second case, the monolayer ReS_2 remains stable (see Fig. 6.5(b)) while $1\mathbf{T}^{\text{Re}_2}\text{-ReS}_2\text{H}_2$ dissociate after 2 ps at around 1000 K by firstly releasing the hydrogen atoms (see Fig. 6.5(d)). The corresponding structures are shown in the lower panel of Fig. 6.5.

6.2. Linear Elastic Properties of Monolayer ReS_2 and $1\mathbf{T}^{\text{Re}_2}\text{-ReS}_2\text{H}_2$ Crystals

The elastic properties of two dimensional homogeneous monolayer materials can be represented by two independent constants, the in-plane stiffness, C , and the Poisson ratio, ν . In addition, the effective Young modulus, E , can be defined for a 2D monolayer material in terms of its proper thickness, h_p , and C to simulate its bulk behavior. In this part of the study, we analyze and discuss the mechanical properties of both of the monolayers, ReS_2 and $1\mathbf{T}^{\text{Re}_2}\text{-ReS}_2\text{H}_2$, in terms of the elastic parameters.

The elastic constants of the monolayer ReS_2 and $1\mathbf{T}^{\text{Re}_2}\text{-ReS}_2\text{H}_2$ are determined by using the energy-strain relation. 48- and 80-atom supercells are constructed for monolayer ReS_2 and $1\mathbf{T}^{\text{Re}_2}\text{-ReS}_2\text{H}_2$, respectively. The supercell vectors are stretched and compressed along the \perp and \parallel directions, respectively. The \perp is defined as the perpendicular direction to Re_4 chains and \parallel is taken to be parallel to Re_4 chains. However, in the case of $1\mathbf{T}^{\text{Re}_2}\text{-ReS}_2\text{H}_2$, these two directions are defined the same as for Re_2 dimers. The strain parameters ε_{\perp} and ε_{\parallel} are varied between ± 0.02 with a step size of 0.01. Then, three different sets of data are calculated; (i) $\varepsilon_{\parallel}=0$ and ε_{\perp} varying, (ii) $\varepsilon_{\perp}=0$ and ε_{\parallel} varying and (iii) $\varepsilon_{\perp}=\varepsilon_{\parallel}$ varying. At each configuration, the atomic positions are fully relaxed

and the strain energy, E_S , is calculated by subtracting the total energy of the equilibrium state from the strained structure. Then, the calculated data is fitted to the equation; $E_S = c_1\varepsilon_{\perp}^2 + c_2\varepsilon_{\parallel}^2 + c_3\varepsilon_{\perp}\varepsilon_{\parallel}$ (Nye, 1985), and the coefficients c_i are determined.

The in-plane stiffness, C , is a measure of the rigidity of a material under applied load. Direction-dependent C can be calculated by two formulas; $C_{\perp} = (1/A_0)(2c_1 - c_3^2/2c_2)$ (Kang *et al.*, 2015) and $C_{\parallel} = (1/A_0)(2c_2 - c_3^2/2c_1)$ (Kang *et al.*, 2015) where $c_1 \neq c_2$ due to the anisotropy of the unit cell and A_0 is the strain-free area of the supercell. The rigidity of monolayer ReS_2 and $\mathbf{1T}^{\text{Re}_2}\text{-ReS}_2\text{H}_2$, may clearly be understood by comparing their in-plane stiffness with that of other 2D materials. Our calculated values of C are 166 and 159 N/m for C_{\perp} and C_{\parallel} (see Table 6.2), respectively for monolayer ReS_2 which are slightly different indicating very small anisotropy between these two directions. When compared with that of graphene (330 N/m (Sahin *et al.*, 2009) and monolayer h-BN (267 N/m (Sahin *et al.*, 2009), monolayer ReS_2 has a smaller C . However, due to its non-planar structure, it is meaningful to compare C of monolayer ReS_2 with that of other TMDs and other non-planar monolayers. ReS_2 is a stiff material when compared other monolayer TMDs such as MoS_2 (124 N/m) (Kang *et al.*, 2015), MoSe_2 (101 N/m) (Kandemir *et al.*, 2016) WS_2 (135 N/m) (Guzman and Strachan, 2014), and WSe_2 (112 N/m) (Guzman and Strachan, 2014) are considered. In addition, it is much stiffer than monolayers of GaS (91 N/m) (Yagmurcukardes *et al.*, 2016) and GaSe (77 N/m) (Yagmurcukardes *et al.*, 2016), non-planar monolayers of post-transition metal chalcogenide family. The rigidity of the monolayer occurs due to the covalent bonding between Re atoms in Re_4 clusters.

By the same methodology, C is calculated for monolayer $\mathbf{1T}^{\text{Re}_2}\text{-ReS}_2\text{H}_2$ and we find that C_{\perp} and C_{\parallel} decreases to 128 and 97 N/m, respectively. As reported for graphene (243 N/m) (Topsakal *et al.*, 2009), hydrogenation reduces the value of C . In our case, the reduction in C is due to the existing of Re_2 dimers instead of Re_4 clusters in monolayer $\mathbf{1T}^{\text{Re}_2}\text{-ReS}_2\text{H}_2$. Thus, the monolayer ReS_2 becomes more flexible material upon full hydrogenation.

The Young modulus, E , is an intrinsic property of a material and generally, it is defined as the ratio of stress to the applied strain in the harmonic regime. For 2D monolayer materials an effective Young modulus can be defined in terms of h_p and C to picture out the bulk behavior of that monolayer. We calculate E by the following formula; $E=C/h_p$, where h_p is calculated from the optimized bulk structure of the monolayer.

The proper thickness of monolayer ReS_2 is calculated to be 5.95 Å and the corresponding E values are 497 and 477 GPa for E_{\perp} and E_{\parallel} , respectively. These values are

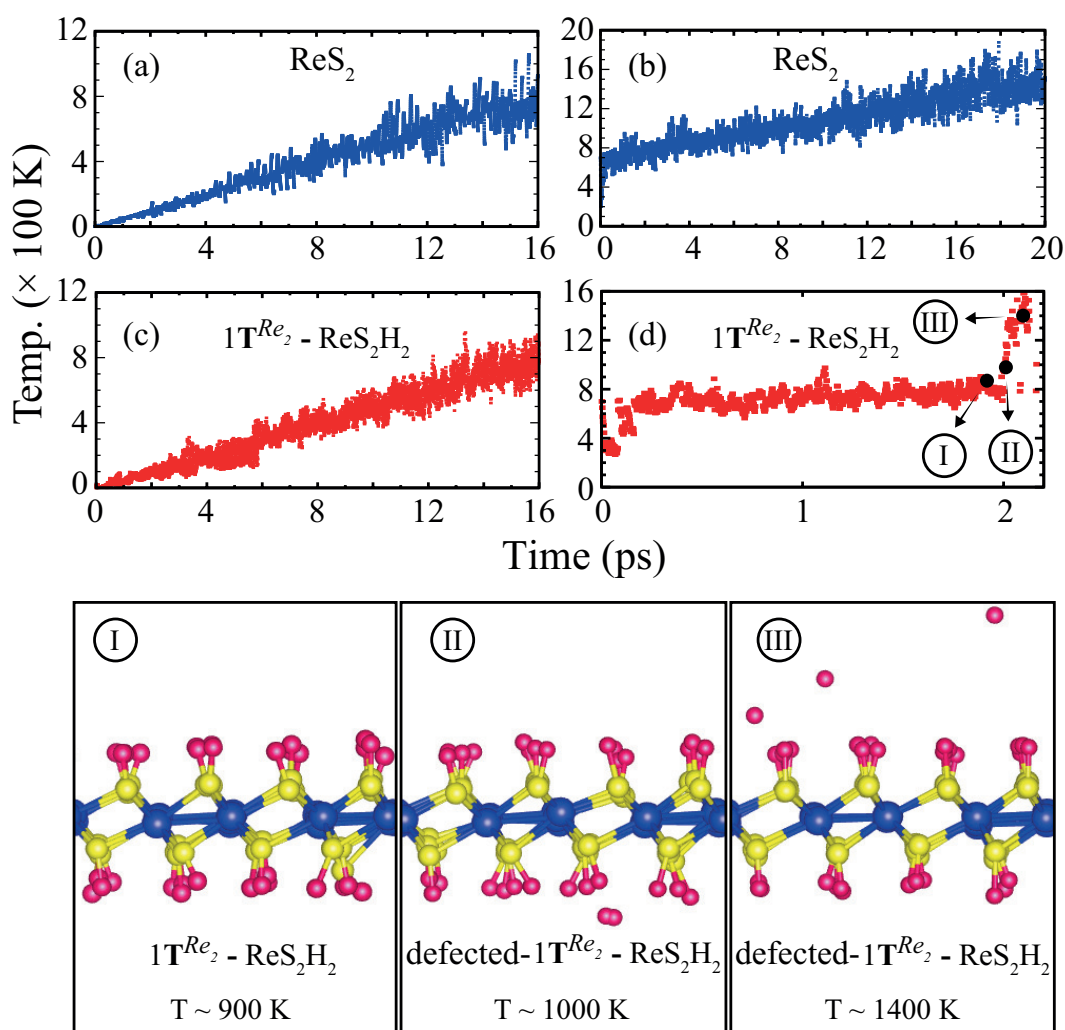


Figure 6.5. Time vs. temperature diagrams of the MD simulations. Two sets of calculations are given. (a) and (c) show the first set in which the temperature increases from 0 to 800 K for the monolayer ReS_2 and $1\text{T}^{\text{Re}_2} - \text{ReS}_2\text{H}_2$, respectively. (b) and (d) show the second set in which the temperature increases from 700 to 1500 K for the monolayer ReS_2 and $1\text{T}^{\text{Re}_2} - \text{ReS}_2\text{H}_2$, respectively. (b) indicates that the monolayer ReS_2 remains stable even at 1500 K. In (d), the dissociation of the $1\text{T}^{\text{Re}_2} - \text{ReS}_2\text{H}_2$ appears as a sudden increase in the system temperature at ~ 2 ps. In lower panel, the structural forms of the $1\text{T}^{\text{Re}_2} - \text{ReS}_2\text{H}_2$ are shown before and after dissociation.

about half of that of graphite (988 GPa). In addition, these values are higher than twice of that of monolayer MoS₂ (202 GPa) (Kang *et al.*, 2015). Since the values of C is reduced by full hydrogenation in monolayer ReS₂, we expect the same trend for E since they are related to each other by a factor of h_p . Our geometry optimizations for the bulk form of **1T^{Re2}-ReS₂H₂** demonstrate that the interlayer distance decreases due to the H-H interactions at the surface of **1T^{Re2}-ReS₂H₂** layers. Thus, h_p decreases to 5.12 Å and the corresponding E values become 329 and 250 GPa for E_{\perp} and E_{\parallel} , respectively.

The Poisson ratio is defined as the ratio of the transverse contraction strain to the longitudinal extension strain in the direction of the stretching force, that is $\nu = -\varepsilon_{trans}/\varepsilon_{axial}$. By using the parameters c_i , the Poisson ratio values along two perpendicular directions are calculated by the following formulas; $\nu_{\perp} = c_3/2c_2$ (Kang *et al.*, 2015) and $\nu_{\parallel} = c_3/2c_1$ (Kang *et al.*, 2015). ν_{\perp} and ν_{\parallel} are found to be the same with a value of 0.19 for monolayer ReS₂. This value is smaller than the values reported for other monolayer TMDs (0.25 for MoS₂, 0.22 for WS₂, and 0.23 for MoSe₂) (Guzman and Strachan, 2014). Generally, stiffer materials are known to possess small Poisson ratio value. Thus, reduction in C by full hydrogenation, results in the increase of ν_{\perp} (0.38) and ν_{\parallel} (0.29) for monolayer **1T^{Re2}-ReS₂H₂**. This increase in ν values demonstrates that under same longitudinal extension, the response of monolayer **1T^{Re2}-ReS₂H₂** will be bigger than that of monolayer ReS₂.

In addition to in-plane mechanical constants, the bending rigidity which demonstrates the behavior of a monolayer material under bending deformation is of fundamental significance for applications in flexible device technology (Kudin *et al.*, 2001). Here, the calculated bending rigidities are 9.9 and 18.2 eV for monolayer ReS₂ and **1T^{Re2}-ReS₂H₂**, respectively along \perp direction while 9.5 and 13.8 eV are found for \parallel direction for monolayer ReS₂ and **1T^{Re2}-ReS₂H₂**, respectively. The calculated values for monolayer ReS₂ are slightly greater than those of other monolayer TMDs such as MoS₂(6.72 eV) (Lai *et al.*, 2016), MoSe₂(6.48 eV) (Lai *et al.*, 2016), WS₂(7.60 eV) (Lai *et al.*, 2016), and WSe₂(7.21 eV) (Lai *et al.*, 2016). In addition, our results indicate that although the in-plane stiffness decreases upon full hydrogenation, the bending rigidity increases due to the increase in the thickness of monolayer ReS₂ with hydrogenation.

6.3. Conclusion

In this study, we investigated the stability of the structure (**1T^{Re2}-ReS₂H₂**) formed upon full hydrogenation of monolayer ReS₂. Firstly, we found that single H atom can

be adsorbed to the surface of monolayer ReS_2 with a considerable binding energy (0.81 eV). Following the analysis of single H adsorption, we showed that full hydrogenation of monolayer ReS_2 results in a dynamically stable crystal structure, $\mathbf{1T}^{\text{Re}_2}\text{-ReS}_2\text{H}_2$, formed by Re_2 dimers. Our *ab-initio* MD simulations demonstrated that the $\mathbf{1T}^{\text{Re}_2}\text{-ReS}_2\text{H}_2$ remains stable up to moderate temperatures, however, the hydrogen atoms dissociate at around 1000 K. Electronic-band structure calculations revealed that monolayer ReS_2 turns into an indirect-gap semiconductor upon full hydrogenation with a decreasing band gap. In addition, the analysis of elastic parameters, C , E , and ν , demonstrated that; (i) monolayer ReS_2 is a stiff material, (ii) it is not highly anisotropic in terms of elastic constants along the considered directions, and (iii) it becomes a more flexible material upon full hydrogenation. Overall, we concluded that monolayer ReS_2 can exhibit a different, dynamically stable structure upon full hydrogenation which is a flexible material suitable for nanoscale mechanical applications.

CHAPTER 7

Mg(OH)₂-WS₂ HETEROBILAYER: ELECTRIC FIELD TUNABLE BANDGAP CROSSOVER

Beyond being novel atomic-thick materials, lateral and vertical heterostructures of novel 2D monolayer crystals have received considerable attention. As constituents of possible heterostructures TMDs are very promising. Those new members of 2D monolayer materials have tunable electronic properties from metallic to wide-gap semiconducting (Wilson and Yoffe, 1969; Ataca *et al.*, 2012) and excellent mechanical properties (Castellanos-Gomez *et al.*, 2012). Moreover, TMDs can be used in various fields such as nanoelectronics (Radisavljevic *et al.*, 2011; Li *et al.*, 2012; Popov *et al.*, 2012), photonics (Eda *et al.*, 2011; Mak *et al.*, 2013), and for transistors (Wang *et al.*, 2012), catalysis (Drescher *et al.*, 2012), hydrogen storage (Seayad and Antonelli, 2004), and Li-ion battery applications (Chang and Chen, 2011). Among TMDs, WS₂ has been studied intensively. It is an indirect-gap semiconductor in its bulk form while it shows a transition to direct-gap character in its monolayer form (Boker *et al.*, 2001; Klein *et al.*, 2001; Thomalla and Tributsch, 2006). It was shown by Ramasubramaniam that the optoelectronic properties of WS₂ and MoX₂ (X=S or Se) monolayers are tunable through quantum confinement of carriers within the monolayers (Ramasubramaniam, 2012). Shi *et al.* showed that the electron effective mass decreases as the applied strain increases, and monolayer WS₂ possesses the lightest charge carriers among the TMDs (Shi *et al.*, 2013). In addition, strong excitonic features of WS₂, including neutral and redshifted charged excitons were observed by Mak *et al.* (Mak *et al.*, 2013) Due to these interesting electronic and optical properties, one may go a step further and construct 2D heterostructures incorporating monolayer WS₂ with other 2D monolayer with the potential to achieve enhanced functionalities.

Recently synthesized monolayer of Mg(OH)₂, a member of alkaline-earth hydroxides (AEH), with formula X(OH)₂ where X = Mg or Ca, are candidate materials for constructing such heterostructures. Magnesium and calcium hydroxides are multifunctional materials which have many important applications in industry, technology, solid-state electronics, and in photovoltaic devices (Estrela *et al.*, 1998; Ghali *et al.*, 2004; Cao *et al.*, 2012). Recently, we studied Ca(OH)₂ monolayer crystals and found that the number of layers of Ca(OH)₂ does not affect the electronic, structural, and magnetic properties qualitatively while the intrinsic mechanical stiffness of each layer becomes slightly larger

as the structure changes from monolayer to bilayer. Very recently, Torun *et al.* (Torun *et al.*, 2016) investigated the electronic and optical properties of the heterobilayer structure GaS-Ca(OH)₂ and found that it is a type-II heterojunction where spatially separated charge carriers can be formed. The optical spectra of different stacking types exhibit distinct properties. Like Ca(OH)₂, Mg(OH)₂ has a layered structure in its bulk form possessing the trigonal symmetry of the space group $\bar{P}3m1$ (brucite) (Desgranges *et al.*, 1996; Catti *et al.*, 1995). Mg(OH)₂ itself is a wide-gap insulator with a band gap of 7.6 eV found experimentally for the bulk structure (Murakami *et al.*, 2011). They reported properties of C-doped Mg(OH)₂ films and found that the material becomes transparent in the visible region and electrically conducting which are favorable properties for applications in photovoltaic devices (Murakami *et al.*, 2011). Huang *et al.* (Huang *et al.*, 2011) found experimentally a spectral peak near the band edge corresponding to strongly localized excitons with an exciton binding energy of 0.53 eV. This indicates a strong localization of the hole and electron to the oxygen p_x and p_y states. Most recently, successful synthesis of Mg(OH)₂ monolayers on MoS₂ and their optical properties were reported by Suslu *et al.* (Suslu *et al.*, 2016)

Here, we predict an electric field dependence of the electronic properties of the Mg(OH)₂-WS₂ heterobilayer structure. Our results reveal that monolayer crystal of Mg(OH)₂ combined with TMDs may lead to the emergence of novel multifunctional nanoscale optoelectronic devices.

The chapter is organized as follows: Structural and electronic properties of monolayers of Mg(OH)₂ and WS₂ are presented in Sec. 7.1 while the structural properties of the Mg(OH)₂-WS₂ heterobilayer are presented in Sec. 7.2. The effect of an external electric field on the electronic properties of the heterobilayer structure is given in Sec. 7.3. Finally, we conclude in Sec. 7.4.

The binding energy per unit cell was calculated by using the following formula: $E_{\text{bind}} = E_{\text{WS}_2} + E_{\text{Mg(OH)}_2} - E_{\text{hetero}}$, where E_{WS_2} and $E_{\text{Mg(OH)}_2}$ denote the total energies of WS₂ and Mg(OH)₂ monolayers, respectively, while E_{hetero} denotes the total energy of the heterobilayer structure.

7.1. Single layer Mg(OH)₂ and WS₂

Monolayer Mg(OH)₂ consists of hydroxyl (OH) groups bonded to Mg atoms. As seen in Fig. 7.1, the layer of Mg atoms is sandwiched between the OH groups in which O and H atoms are strongly bonded to each other. The calculated lattice parameters

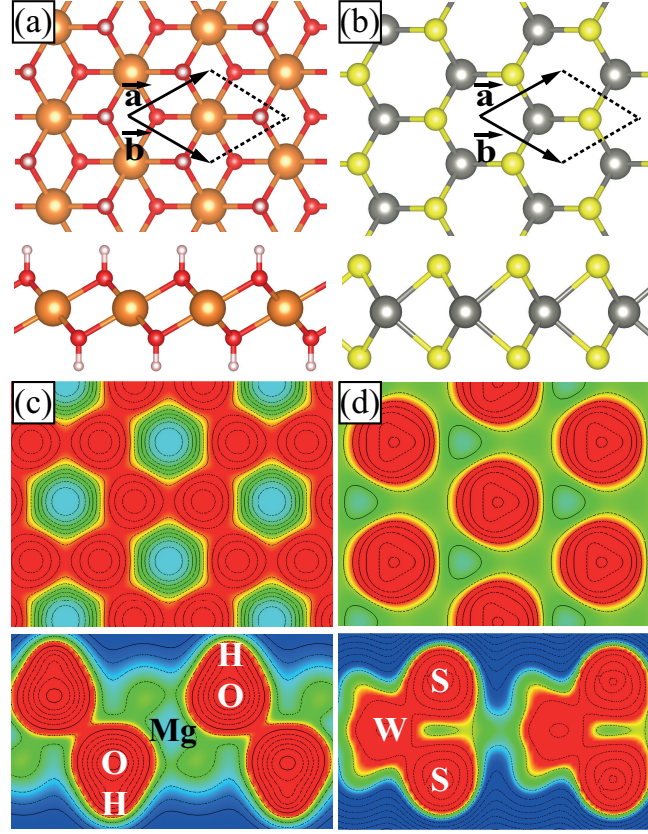


Figure 7.1. Top and side view of monolayers of (a) $\text{Mg}(\text{OH})_2$ and (b) WS_2 . The charge distribution on the individual atoms are shown in top and side views of (c) $\text{Mg}(\text{OH})_2$ and (d) WS_2 . Increasing charge density is shown by a color scheme from blue to red with the formula $F(N)=1 \times 1000^{N/step}$ where step size taken to be 10 and N ranges from -1 to 2.

Table 7.1. The calculated ground state properties of monolayer and their heterobilayer structures: structure, lattice parameters of primitive unit cell, a and b (see Fig. 7.1), the distance between the individual atoms contained in each monolayer d_{X-Y} , magnetic state, the total amount of charge received by the O or S atoms $\Delta\rho$, the energy band gap of the structure calculated within GGA (E_g^{GGA}), SOC (E_g^{SOC}) and HSE06 (E_g^{HSE}), and workfunction Φ determined from $\text{Mg}(\text{OH})_2$ side.

	Geometry	a (Å)	b (Å)	$d_{\text{Mg-O}}$ (Å)	$d_{\text{O-H}}$ (Å)	$d_{\text{W-S}}$ (Å)	μ	$\Delta\rho$ (e)	E_g^{GGA} (eV)	E_g^{SOC} (eV)	E_g^{HSE} (eV)	Φ (eV)
$\text{Mg}(\text{OH})_2$	1T	3.13	3.13	2.09	0.96	-	NM	2.9	3.25	3.22	4.75	4.15
WS_2	1H	3.18	3.18	-	-	2.41	NM	1.1	1.86	1.54	2.30	5.29
Heterobilayer	1T	3.16	3.16	2.10	0.96	2.41	NM	-	1.05	0.97	2.24	4.34

for monolayer $\text{Mg}(\text{OH})_2$ are $a=b=3.13 \text{ \AA}$. The thickness of monolayer $\text{Mg}(\text{OH})_2$ is 4.01 \AA . The bond length of Mg-O and O-H bonds are calculated to be 2.09 \AA and 0.96 \AA , respectively. Bader charge analysis shows that ionic bond character is present in the $\text{Mg}(\text{OH})_2$ monolayer. In the structure each H atom donates $0.6 e$ to neighboring O atom and each Mg donates $0.85 e$ per O atom.

Generic forms of monolayer structures of TMDs display honeycomb lattice symmetry with the 1H phase for the dichalcogenides of Mo and W atoms. The calculated lattice parameters for the 1H phase of WS_2 monolayer are $a=b=3.18 \text{ \AA}$ which is very close to that of $\text{Mg}(\text{OH})_2$ monolayer. The W-S bond length in WS_2 is calculated to be 2.42 \AA . The thickness of the layer is 3.13 \AA which is thinner than monolayer $\text{Mg}(\text{OH})_2$. In the monolayer WS_2 $0.55 e$ of charge accumulation occurs from a W atom to each of the S atoms and the corresponding bonding character is covalent.

The calculated band structures within HSE06 correction are shown in Fig. 7.2. Monolayer $\text{Mg}(\text{OH})_2$ is found to be a direct band gap semiconductor with a band gap of 4.75 eV . Both the valence band maximum (VBM) and the conduction band minimum (CBM) reside at the Γ point in the Brillouin zone (BZ). The states in the VBM of the $\text{Mg}(\text{OH})_2$ monolayer are composed of p_x and p_y orbitals of the O atoms.

Similar to the monolayer $\text{Mg}(\text{OH})_2$, monolayer WS_2 is also a direct band gap semiconductor but with a lower band gap of 2.30 eV . As in other TMDs, both the VBM and CBM of single layer WS_2 lie at the K point in the BZ. As seen in Fig. 7.2(b), spin-orbit interaction at the VBM states is much stronger since the states are composed of d_{x^2} and d_{z^2} orbitals of W atoms. There is an energy splitting of 430 meV at VBM which is much larger than that of monolayer $\text{Mg}(\text{OH})_2$ which is calculated to be 25 meV .

7.2. Heterobilayer

The calculated lattice constants of $\text{Mg}(\text{OH})_2$ and WS_2 monolayers are very close to each other and therefore it is possible to construct a heterostructure of these monolayers where we may assume a primitive unit cell containing 8 atoms in total. We considered three different high-symmetry stacking configurations of the monolayers (see Fig. 7.3). We found that two of the stacking configurations have binding energies very close to each other but the one with the W atoms residing on top of an interface OH group is the ground state with a binding energy of 147 meV . We also performed energy-band structure calculation for the stacking configuration given in Fig. 7.3(c). The energy-band structures of two configurations have exactly the same properties. Thus in this paper we only studied

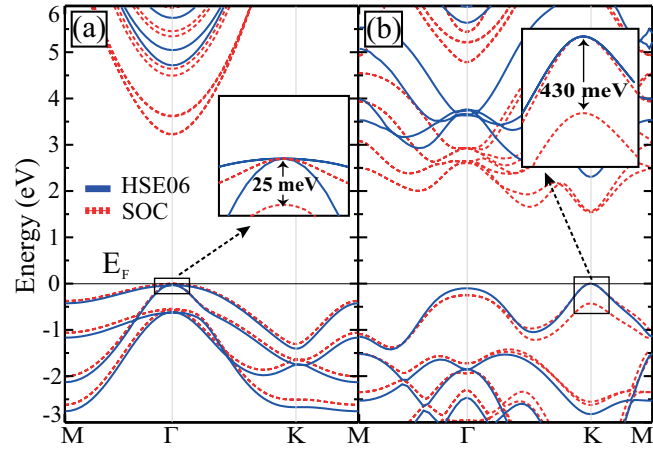


Figure 7.2. Calculated energy-band structure of monolayer (a) $\text{Mg}(\text{OH})_2$ and (b) WS_2 . The Fermi energy (E_F) level is set to the valence band maximum.

the electronic properties of the ground state configuration (see Fig. 7.3(b)). For the lowest energy stacking configuration the interlayer distance is calculated to be 2.09 \AA and the individual atomic bond lengths remain the same as in their isolated layers. The analysis for the charge transfers between the individual layers demonstrate that there is no depletion from one layer to the other for all the stacking geometries shown in Fig. 7.3. This result is expected due to the weak vdW interaction between the individual layers.

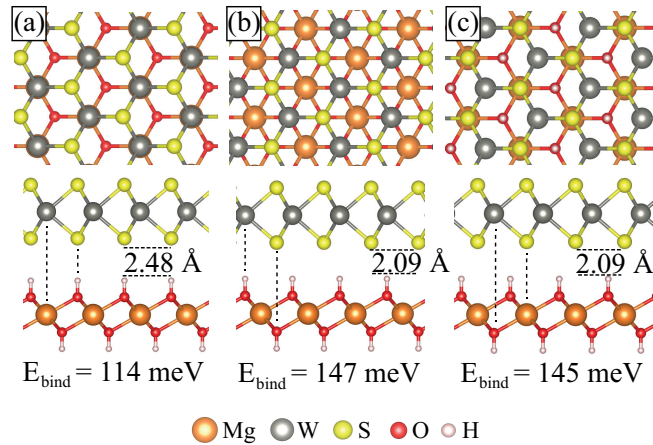


Figure 7.3. Different possible stacking configurations for the heterobilayer structure. (a) W atom on top of Mg atom, (b) W atom on top of upper OH group, and (c) W atom on top of lower OH group.

The calculated energy-band structure for the heterobilayer displays a semicon-

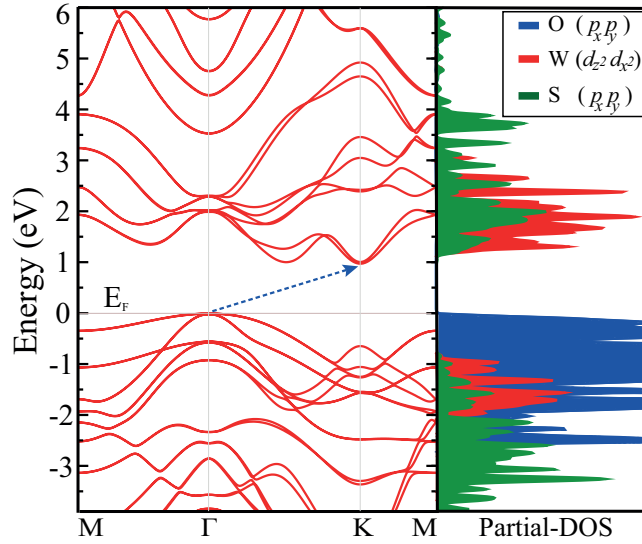


Figure 7.4. The band structure (left) and the corresponding partial density of states (PDOS) (right) of the heterobilayer structure calculated within SOC. The Fermi energy (E_F) level is set to the valence band maximum.

ducting character with an indirect band gap of 2.24 eV. As seen in Fig. 7.4, the VBM of the heterobilayer that originates from the $\text{Mg}(\text{OH})_2$ layer lies at the Γ point while the CBM of the structure which arises from the WS_2 layer lies at the K point. Calculated energy-band diagram of the heterostructure also indicates the weak interlayer interaction. As seen in Fig. 7.4, the partial DOS (PDOS) indicates that the VBM of heterobilayer exclusively consists of p_x and p_y orbitals of the O atoms while the CBM is characterized by the orbitals of W and S atoms. This also demonstrates the type-II nature of the heterojunction: the two band edges originate from different individual layers and consequently the excited electrons and holes are confined in different layers which leads to the formation of spatially indirect excitons.

7.3. Effect of External Electric Field

Applying an external electric field is one of the common method to modify or tune the physical properties of materials. In the field of 2D materials, a perpendicular electric field can lead to doping and in the case of bilayers it can induce charge transfer between layers. Castro *et al.* reported that the electronic band gap of a graphene bilayer structure can be controlled externally by applying a gate bias. They showed that the band

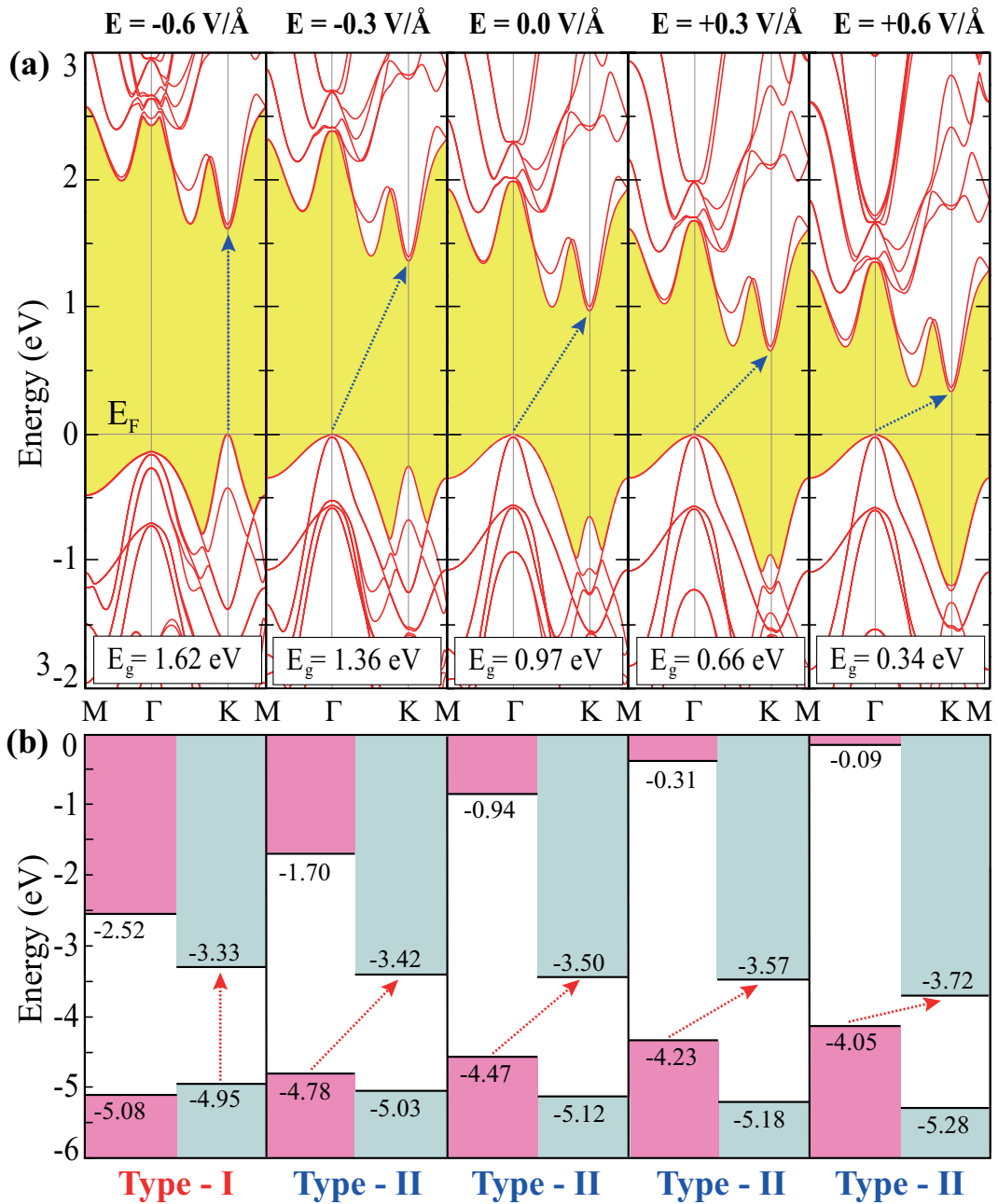


Figure 7.5. (a) The effect of an external out-of-plane electric field on the band structure of the heterobilayer and (b) the corresponding band alignments (vacuum levels are set to zero). The band gap regions are highlighted in yellow while the CBM and VBM are highlighted in pink and gray for Mg(OH)₂ and WS₂, respectively.

gap changes from zero to midinfrared energies for field values ≤ 1 V/nm (Castro *et al.*, 2007). Chu *et al.* showed a continuous bandgap tuning in bilayer MoS₂ with applied gate voltage (Chu *et al.*, 2015). Here we present our results for the effect of a perpendicular electric field on the electronic and optical properties of the heterobilayer.

As seen in Fig. 7.5(a), the heterostructure is an indirect band gap semiconductor when there is no external electric field, in which the VBM is at Γ but the CBM is at the K point. Applying a positive electric field decreases the band gap (from 0.97 eV to 0.34 eV for $E = +0.6$ V/Å). The reason for such decreasing band gap is the shift of the band edges at the Γ and the K points. Increasing the value of the positive electric field shifts the VBM of Mg(OH)₂ up in energy while it shifts the CBM of WS₂ down resulting in a decrease of the energy gap. The indirect character of the energy gap is not affected by the field. However, changing the direction of the applied electric field widens the band gap and ultimately leads to an indirect-to-direct band-gap-crossover as seen in Fig. 7.5(a).

When the strength of the electric field is -0.6 V/Å, it is clearly seen that both VBM and CBM of the heterobilayer reside at the K high symmetry point in the BZ. Thus, a transition from staggered gap to a straddling gap (type-I heterojunction) occurred as shown in Fig. 7.5(b). In fact, the critical electric field value for which this indirect-to-direct band-gap-crossover occurs is calculated to be 0.51 V/Å. At this critical value of the applied electric field, the valence band edge energy of the bands at the Γ and K points become degenerate. As seen in Fig. 7.5(a), the bands at the valence band edge of the K point, which originate from the WS₂ layer, shift up while the bands at the Γ point which originate from the Mg(OH)₂ layer shift down when making the external electric field more negative. Due to these opposite shifts of the VBM of the individual layers (see Fig. 7.5(b)) a transition from indirect-to-direct gap is predicted at a certain value of the applied field. After the transition to type-I heterojunction both type of charge carriers are confined to the WS₂ layer which is desirable for applications in optoelectronic devices and for semiconductor laser applications. It is also important to point out that including quasiparticle energies might slightly change the band gap and the electric field value for which the indirect-to-direct band-gap-crossover occurs. However, the overall tunability characteristic of the heterobilayer using electric field would remain the same.

7.4. Conclusion

We investigated the structural, electronic and optical properties of the monolayers Mg(OH)₂ and WS₂ and its heterobilayer structure. In addition the effect of an applied

out-of-plane electric field on the electronic and optical properties of the heterobilayer were investigated. We found that both $\text{Mg}(\text{OH})_2$ and WS_2 are direct-gap semiconductors while the $\text{Mg}(\text{OH})_2$ - WS_2 heterobilayer structure is an indirect-gap semiconductor. Our results demonstrated that both the band gap and the energy-band dispersion of the heterobilayer structure can be tuned by the application of an external perpendicular electric field. At an applied electric field of -0.51 V/\AA a transition from a staggered to a straddling gap heterojunction occurs which can be used for optoelectronic and semiconductor laser applications. It appears that heterobilayers of TMDs and AEHs may find applications in various nanoscale optoelectronic devices.

CHAPTER 8

STRAIN-DEPENDENT VIBRATIONAL PROPERTIES OF NOVEL TWO DIMENSIONAL SINGLE LAYER CRYSTALS

Raman spectroscopy (Raman, 1928) is a powerful characterization technique which crop information about the nature of the material medium entities by monitoring the characteristic vibrational energy levels of the structure. It is also very useful due to providing non-destructive analysis and requiring minimum sample preparation. Development of the experimental techniques in recent years allow us to make more accurate and reliable Raman measurements as compared to the past decades. Raman measurement can reveal information about substrate-free layer-number identification of layered materials, (Qiao *et al.*, 2015) the strength of the interlayer coupling in layered materials (Tan *et al.*, 2011) and interface coupling in van der Waals heterostructures (Wu *et al.*, 2015, 2014). Absolute and relative intensities of the Raman peaks lead to the determination of different-phase distributions in a material. (Colomban, 2003; Gouadec and Colomban, 2007; Havel *et al.*, 2004) Raman spectroscopy can also gives information about electronic structure, thickness, and can be used to probe strain, stability, stoichiometry, and stacking orders of 2D materials (Zhang *et al.*, 2015).

The strain can alter materials electronic and vibrational properties. (Guinea *et al.*, 2009; He *et al.*, 2013) Nonetheless, Raman peak positions and intensities are significantly affected in the presence of strain. (Ni *et al.*, 2008; Huang *et al.*, 2010) Although Raman spectroscopy has been widely studied in literature, (Ferrari and Basko, 2013; Berkdemir *et al.*, 2013; Chenet *et al.*, 2015b; Frostig *et al.*, 2015) detailed theoretical investigation of the strain effects on Raman peak positions and intensities for the 2D materials are still waiting revisits. Here, we theoretically investigate the strain dependencies of the vibrational properties of diverse 2D materials in terms of Raman activity and intensity of the vibrational modes.

The vibrational properties of all monolayer crystals were calculated in terms of the off-resonant Raman activities of phonon modes at the Γ point. For this purpose, the vibrational phonon modes at the Γ point were calculated using finite-difference method as implemented in VASP. Each atom in the primitive unitcell was initially distorted 0.01 Å and the corresponding dynamical matrix was constructed. Then, the vibrational modes

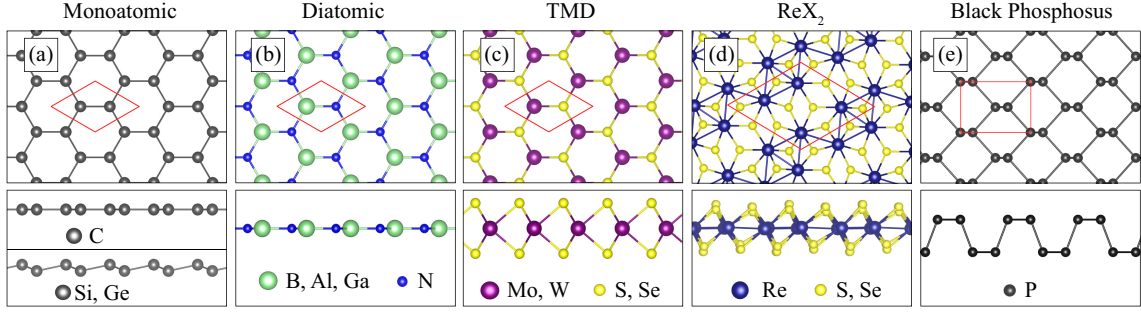


Figure 8.1. Top and side view of typical single-layer structures; (a) mono-atomic, (b) diatomic, (c) TMDs, (d) anisotropic single-layer structures, and (e) black phosphorus. Color code of atoms given in corresponding figure. Primitive cells are indicated with red solid lines.

Table 8.1. For the single-layer crystal structures; the structure, planar (PL), low-buckled (LB), or puckered (P), calculated lattice parameters a and b , the point group of the single-layer, total number of Raman active phonon modes, the in-plane static (low-frequency) dielectric constant, ϵ , and the energy-band gap of the structures calculated within SOC on top of GGA (E_g^{SOC}). Note : * The average in-plane static dielectric constant taken for anisotropic materials. ¹ (Gmitra *et al.*, 2009), ² (Tabert and Nicol, 2013), ³ (Liu *et al.*, 2011), ⁴ (Kim, Hsu, Jia, Kim, Shi, Dresselhaus, Palacios, and Kong, Kim *et al.*), ⁵ (Hüser *et al.*, 2013), and ⁶ (Ramasubramaniam, 2012).

	Structure	a (Å)	b (Å)	Point Group	Raman Active Modes	ϵ_{cal}	ϵ_{rep}	E_g^{SOC} (eV)
Graphene	PL	2.47	2.47	D_{3h}	2	23.31		$(24 \times 10^{-6})^1$
Si	LB	3.85	3.85	D_{3d}	3	8.01		0.001-0.01 ²
Ge	LB	4.01	4.01	D_{3d}	3	9.04		0.02-0.1 ³
h -BN	PL	2.51	2.51	D_{3h}	2	1.5	2-4 ⁴	4.68(d)
h -AlN	PL	3.13	3.13	D_{3h}	2	1.46		3.61(i)
h -GaN	PL	3.27	3.27	D_{3h}	2	1.71		2.37(i)
MoS ₂	1H	3.19	3.19	D_{3h}	5	4.46	4.2-7.6 ⁵	1.56(d)
MoSe ₂	1H	3.32	3.32	D_{3h}	5	5.02	4.74 ⁶	1.33(d)
WS ₂	1H	3.18	3.18	D_{3h}	5	4.12	4.13 ⁶	1.53(d)
WSe ₂	1H	3.33	3.33	D_{3h}	5	4.67	4.63 ⁶	1.19(d)
ReS ₂	1T'	6.46	6.38	C_{1h}	18	4.18*		1.34(d)
ReSe ₂	1T'	6.71	6.60	C_{1h}	18	4.71*		1.27(d)
BP	P	4.57	3.31	D_{2h}	6	4.32*		0.88(d)

were determined by a direct diagonalization of the dynamical matrix. The calculations were performed using GGA functional with the inclusion of DFT-D2 method of Grimme vdW functional with a k -point set of $24 \times 24 \times 1$. The k -point set was increased step by step until the convergence for the frequencies of acoustic modes was reached (0.0 cm^{-1} for each acoustic mode). Once the accurate phonon mode frequencies were obtained at the Γ point, the change of macroscopic dielectric tensor was calculated with respect to each vibrational mode to get the corresponding Raman activities.

8.1. Strain-Dependent Raman Activity

Raman spectroscopy is a special technique for the observation of vibrational modes in a sample. It is a fingerprint for distinguishing different crystal phases of a material and also for distinguishing layer number in layered materials. Basically in the Raman theory, inelastic scattering of incident photons is detected and the intensity of the scattered radiation from the oscillating dipoles in the crystal is measured.

The treatment of Raman intensities is based on Placzek's classical theory of polarizability. According to the classical Placzek approximation, the intensity of a Raman active phonon mode is proportional to $|\hat{e}_s \cdot R \cdot \hat{e}_i|^2$ where \hat{e}_s and \hat{e}_i stand for the polarization vectors of scattered radiation and incident light, respectively. R is a 3×3 second rank tensor called 'Raman tensor' whose elements are derivatives of polarizability of the material with respect to vibrational normal modes,

$$\begin{bmatrix} \frac{\partial \alpha_{11}}{\partial Q_k} & \frac{\partial \alpha_{12}}{\partial Q_k} & \frac{\partial \alpha_{13}}{\partial Q_k} \\ \frac{\partial \alpha_{21}}{\partial Q_k} & \frac{\partial \alpha_{22}}{\partial Q_k} & \frac{\partial \alpha_{23}}{\partial Q_k} \\ \frac{\partial \alpha_{31}}{\partial Q_k} & \frac{\partial \alpha_{32}}{\partial Q_k} & \frac{\partial \alpha_{33}}{\partial Q_k} \end{bmatrix} \quad (8.1)$$

where the Q_k is the normal mode describing the whole motion of individual atoms participating to the k^{th} vibrational mode. α_{ij} is the polarizability tensor of the material. Generally, Raman tensor is written with the knowledge of group theory for every vibrational mode. The term $|\hat{e}_s \cdot R \cdot \hat{e}_i|^2$ is called as the Raman activity which is calculated from the change of polarizability. For a back scattering experimental geometry, if orientational averaging is considered, the Raman activity is represented in terms of Raman invariants given by,

$$\alpha_s \equiv \frac{1}{3}(\tilde{\alpha}_{xx} + \tilde{\alpha}_{yy} + \tilde{\alpha}_{zz}) \quad (8.2)$$

$$\beta \equiv \frac{1}{2}\{(\tilde{\alpha}_{xx} - \tilde{\alpha}_{yy})^2 + (\tilde{\alpha}_{yy} - \tilde{\alpha}_{zz})^2 + (\tilde{\alpha}_{zz} - \tilde{\alpha}_{xx})^2 + 6[(\tilde{\alpha}_{xy})^2 + (\tilde{\alpha}_{yz})^2 + (\tilde{\alpha}_{xz})^2]\} \quad (8.3)$$

where $\tilde{\alpha}_s$ and β represents the isotropic and anisotropic parts of the derivative of polarizability tensor, respectively. The $\tilde{\alpha}$ represents the derivative of polarizability with respect to a normal mode. The importance of representing the intensity in terms of these two variables is being invariant to a change in the sample orientation. Finally, using these forms of isotropic and anisotropic polarizability derivative tensors, the Raman activity, R_A , can be written as,

$$R_A = 45\tilde{\alpha}^2 + 7\beta^2 \quad (8.4)$$

8.1.1. Mono-Elemental Single-Layer Crystals

As mono-atomic single-layer crystals, graphene, silicene, and germanene, have hexagonal crystal structures. Due to sp^2 hybridization of C atoms in graphene, its structure is planar and belongs to $P\bar{6}/mmm$ space group symmetry. On the other hand, sp^3 hybridization in silicene and germanene results in a buckled geometry (see Fig. 8.1(a)). The structure of these two mono-atomic buckled single-layers belong to $P\bar{3}m\bar{1}$ space group. Different from graphene, silicene and germanene exhibit tiny electronic band gap (1.55-7.90 meV (Tabert and Nicol, 2013) and 24-93 meV (Liu *et al.*, 2011) for silicene and germanene, respectively) due to spin-orbit coupling effect.

Mono-elemental single-layers, graphene, silicene, and germanene, have 2-atomic primitive unitcell which corresponds to 6 phonon branches that consist of 3 acoustic and 3 optical branches. These single-layers have 3 optical phonon modes one of which is out-of-plane (ZO) mode. Our calculated frequencies for ZO mode are 872.8, 193.8, and 172.2 cm^{-1} for graphene, silicene, and germanene, respectively. The strength of atomic bonding between the atoms determines the position of all phonon modes in frequency space. The ZO mode is a Raman inactive mode for graphene due to its planar crystal structure. However, as result of buckled geometry of silicene and germanene ZO should be a Raman active mode. It was reported that both silicene and germanene were synthesized on

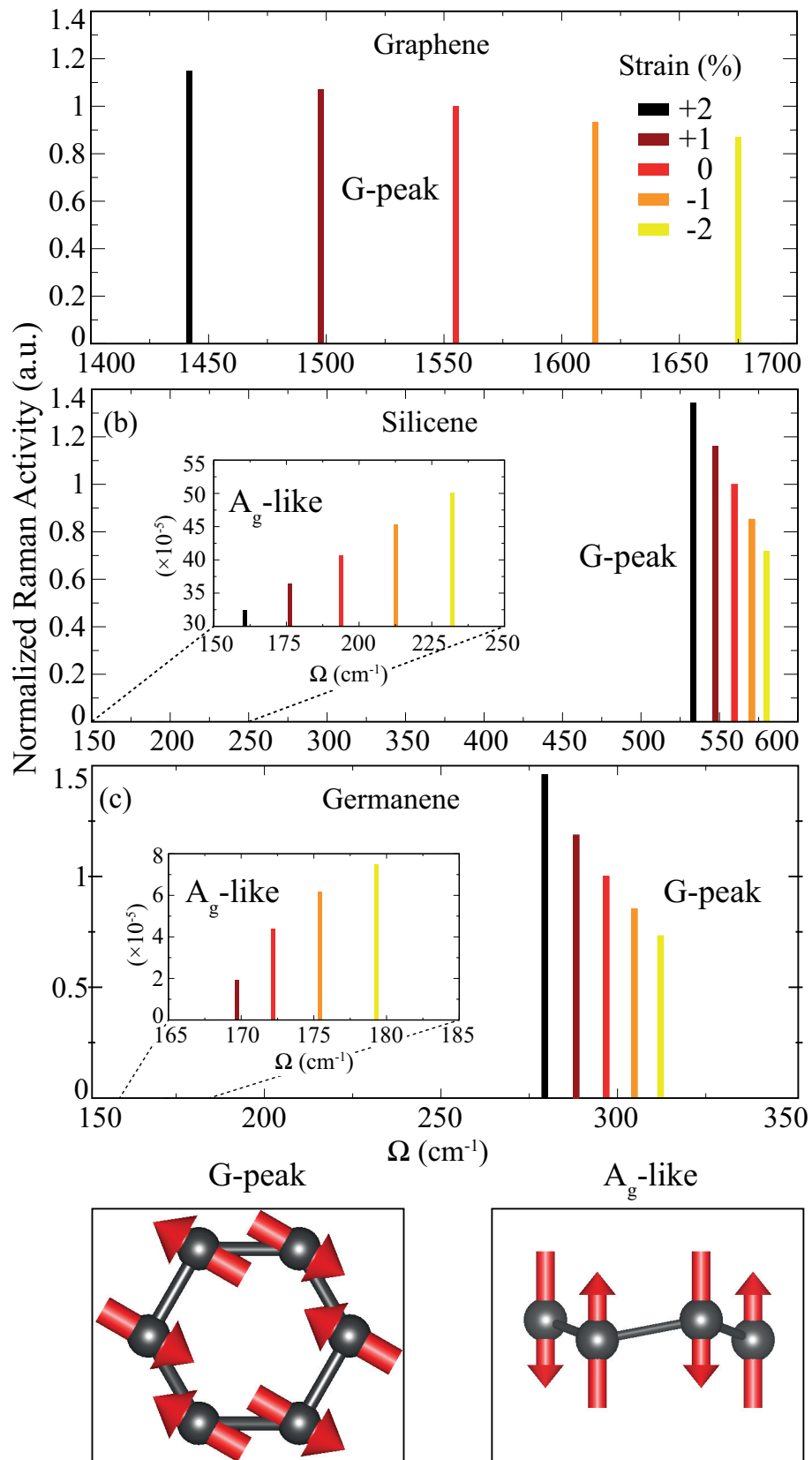


Figure 8.2. The response of activity of Raman active modes to the applied biaxial strain for (a) graphene, (b) silicene, and (c) germanene. The insets in (b) and (c) are for ZO phonon mode.

different substrates and they are not stable in their free standing forms. Thus, because of the effect of substrate on this A_g -like phonon mode, it is not possible to observe ZO mode in experiments.

The other two optical modes, transverse optical (TO) and longitudinal optical (LO), are doubly degenerate for these single-layer crystals. The frequencies are calculated to be 1555.0, 559.6, and 296.8 cm^{-1} for graphene, silicene, and germanene, respectively. This Raman active mode is a characteristic peak and known as the G-peak observed in experiments. As mentioned above, ZO mode is Raman inactive for graphene and calculated to be Raman active for silicene and germanene. The calculated Raman activity of ZO mode in silicene and germanene is smaller than that of LO and TO modes about 10^4 times (see Figs. 8.2(b) and 8.2(c)).

In addition to the analysis of these optical phonon branches, we also investigate the effect of biaxial strain on the activity of these modes. The biaxial strain is applied in the harmonic regime (between $\pm 2\%$). For all 3 single-layer materials, as shown in Fig. 8.4(a) we find that a significant phonon softening occurs under tensile biaxial strain while a phonon hardening is investigated under compressive strain. This trend can be expected because of the varying atomic bond lengths which affects the strength of the bonds. Our calculated Raman activities demonstrate that ZO and LO-TO phonon modes have opposite trends under applied biaxial strain (see Fig. 8.2). The activity of ZO mode decreases with the increase of tensile strain while increases under compressive strain. It is found that when the applied tensile strain is increased, buckling of silicene and germanene decreases and the Raman activity of ZO mode approaches to zero. On the other hand, the Raman activity of LO-TO phonon modes increases under tensile strain while it decreases with compression of the structure.

8.1.2. Diatomic Single-Layer Crystals

Similar to graphene crystal structure, diatomic single-layers of group-III Nitrides (h -BN, h -AlN, and h -GaN) have planar, one-atom-thick structure as shown in Fig. 8.1(b). These crystal structures belong to space group of $P6_3/mmc$.

The crystal structure of these 3 single-layers is planar like graphene structure and thus, the same trends in both frequencies and Raman activities of phonon modes are expected for the diatomic single-layers. Due to number of atoms in the primitive unitcell of the single-layers, 6 phonon branches are calculated as in the case of mono-elemental single-layer crystals. The inter-atomic bond lengths of atoms decrease from h -BN to

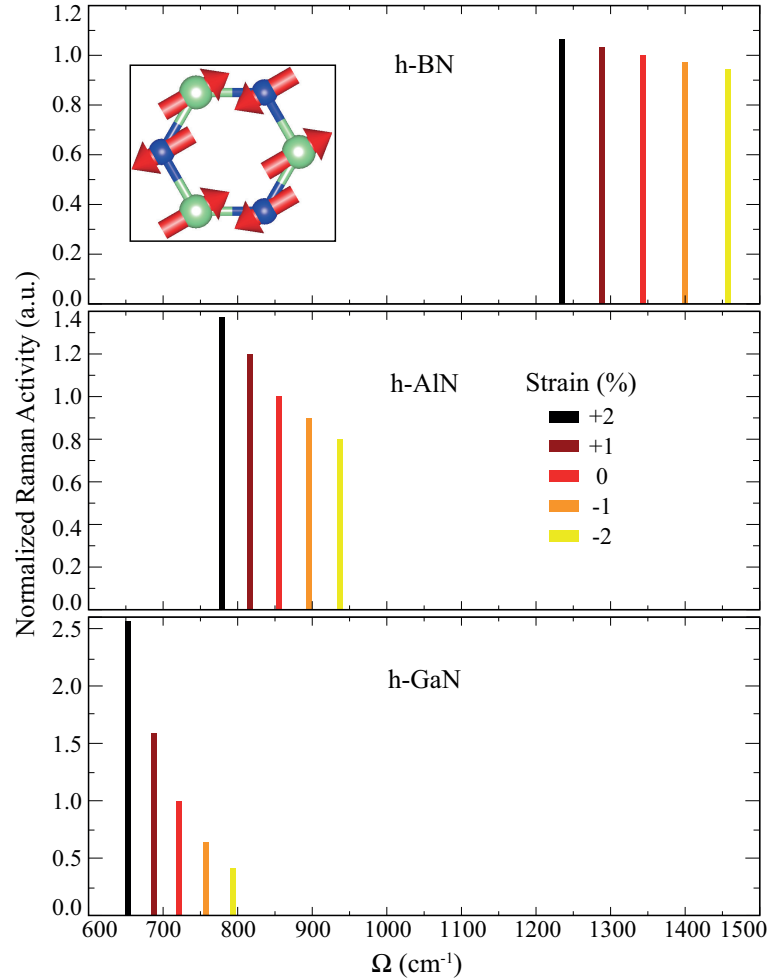


Figure 8.3. The response of activity of Raman active modes to the applied biaxial strain for single-layer (a) *h*-BN, (b) *h*-AlN, and (c) *h*-GaN. The given response is for the LO-TO phonon mode which is the only Raman active mode for diatomic single-layers.

h-GaN that determines the position of frequencies of the optical phonon modes. As in the case of graphene, ZO phonon mode is a Raman inactive mode for these diatomic single-layer crystals. The frequencies of ZO mode are calculated to be 800.9, 412.5, and 263.6 cm^{-1} for *h*-BN, *h*-AlN, and *h*-GaN, respectively. When a biaxial strain is applied, a significant phonon softening is observed from compressive strain to tensile strain as shown in Fig. 8.4(a).

Our calculated Raman activities indicate that single-layers of *h*-BN, *h*-AlN, and *h*-GaN have only degenerate TO-LO phonon modes to be Raman active. The frequencies of this doubly degenerate optical modes are calculated to be 1343.4, 855.5, and 721.6 cm^{-1} for *h*-BN, *h*-AlN, and *h*-GaN, respectively. Under applied compressive biaxial strain,

the frequencies of these modes shift to 1457.7, 936.9, and 793.2 cm^{-1} while a phonon softening to 1235.5, 779.4, and 653.5 cm^{-1} frequencies is seen under tensile biaxial strain for *h*-BN, *h*-AlN, and *h*-GaN, respectively. When the response of Raman activities are analyzed, the largest response to applied strain can be seen for single-layer *h*-GaN under tensile strain as 157% increase.

8.1.3. TMDs Single-Layer Crystals

The single-layer of TMDs has a hexagonally packed structure in which the sub-layer of metal (M) atom is sandwiched between two sub-layers of chalcogen (X) atoms (see Fig. 8.1(d)). Thus, the structural unit is formulated by MX_2 . Most of the single-layer TMDs crystallize in either 1H or 1T phases. Here, we consider single-layers of Mo- and W-dichalcogenides all of which have 1H crystal structure. These single-layer crystals have $P\bar{6}/m\bar{2}$ space group symmetry. Our structural analysis reveals that depending on the atomic radii, single-layers of MSe_2 (M=Mo or W) have larger lattice constants than that of MS_2 .

Monolayers of Mo- and W-dichalcogenides with S or Se atoms, have 3-atomic primitive unitcell and thus, totally 9 phonon branches are calculated. Out of 3 acoustic phonon branches, 6 optical phonon branches exist in their phonon-band structure. The in-plane shear modes are known to be doubly degenerate for in-plane isotropic single-layer TMDs, MoS_2 , MoSe_2 , WS_2 , and WSe_2 . These in-plane optical phonon modes, LO-TO modes, are known as the E' , the chalcogen atoms move in opposite direction to the transition metal atom, and E'' , the transition metal atom is stationary and the chalcogen atoms move in opposite directions. These two doubly degenerate modes are expected to be Raman active since their motion have an in-plane inversion symmetry which results in the change of polarizability. The E'' phonon mode is the lowest frequency optical mode for all these single-layer TMDs. The calculated frequencies are 277.8, 162.5, 289.5, and 167.9 cm^{-1} for single-layer MoS_2 , MoSe_2 , WS_2 , and WSe_2 , respectively. As it is seen for Mo-dichalcogenides there is a huge difference in frequencies of the phonon modes which is a natural result of Mo-S and Mo-Se bonds. When the S and Se atoms are compared, both the atomic radius and masses are larger for Se atom which results in longer M-X bond length. The same trend can be seen when the transition metal atom is changed from Mo atom to W. In fact, all the factors affecting the frequencies of phonon modes are strongly related (atomic masses, radii, bond lengths, etc.). In this phonon mode, since only the chalcogen atoms move in opposite directions, the change in the dielectric tensor

is very small. Thus, the lowest Raman activity is calculated for E'' optical phonon mode. When compared with the Raman activity of other two modes, activity of E'' is in the order of 10^{-4} for TMDs with S-atom while it is in the order of 10^{-3} for TMDs with Se-atom. The response of the Raman activity of this phonon mode to the applied biaxial strain is in the same order with its unstrained value. Thus, experimentally it still difficult to be observed since there is no significant change in the Raman activity (see left panel of Figs. 8.5(a)-(d)).

The group theory analysis indicate that these single-layer TMDs have all D_{3h} symmetry group which should give totally 5 Raman active modes. Our calculations well match with this knowledge that in addition to E'' phonon mode we have another doubly degenerate Raman active mode, E' , and a singly degenerate ZO Raman active mode called as A_1 as shown in bottom panel of Fig. 8.5. Differing from E'' phonon mode, in the characteristic of E' mode the chalcogen atoms move in opposite direction to the transition metal atom. In all single-layers, the frequency of this Raman active mode is higher than that of E'' which is due to the additional motion of transition metal atom. The calculated frequencies are 375.8, 278.3, 348.2, and 239.0 cm^{-1} for single-layer MoS_2 , MoSe_2 , WS_2 , and WSe_2 , respectively. It was reported in many experiments that this E' phonon mode is a characteristic Raman active mode observed for single-layer TMDs. As in the case of another single-layer crystals, the response of the Raman activity of E' phonon mode shows an increasing trend from compressive biaxial strain to tensile one. The frequency of E' phonon mode is smaller than that of A_1 mode except for single-layer MoSe_2 while its Raman activity is only smaller for single-layer MoSe_2 than that of A_1 mode. The change in the activity of E' phonon mode is meaningless itself because there are two characteristic Raman active modes and thus, the relative activities of E' and the A_1 mode should be taken into account.

The A_1 phonon mode is the only Raman active out-of-plane mode for these single-layer TMDs. Another out-of-plane phonon mode, A_2'' , is a Raman inactive mode which represents the opposite vibrations of chalcogen and transition metal atoms move in out-of-plane direction. This mode in fact is known to be an infrared active phonon mode from the group theory analysis. The frequency of A_1 mode is higher than that of E' phonon mode except for the single-layer MoSe_2 . Our calculated frequencies for A_1 mode are 401.0, 237.3, 412.4, and 244.4 cm^{-1} for single-layer MoS_2 , MoSe_2 , WS_2 , and WSe_2 , respectively. The large difference in frequencies occur due to the larger vertical distance between Se atoms. Due to this larger distance of Se-Se atoms, the out-of-plane stiffness will be smaller for Se-based TMDs and thus, the frequencies of out-of-plane phonon

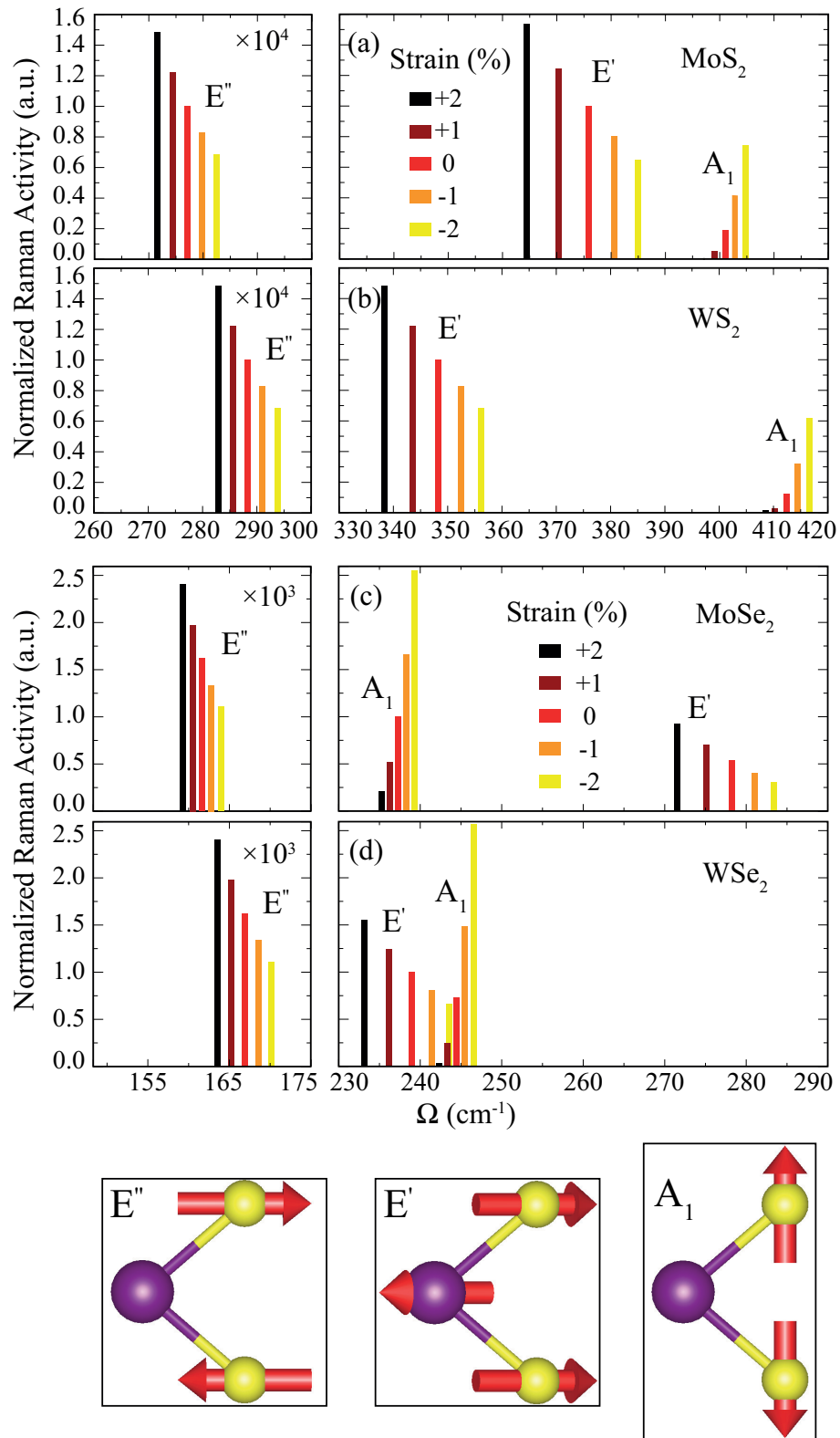


Figure 8.4. (a) The response of frequencies and (b) Raman activities of Raman active modes to the applied biaxial strain for single-layers of mono- and di-atomic crystal structures.

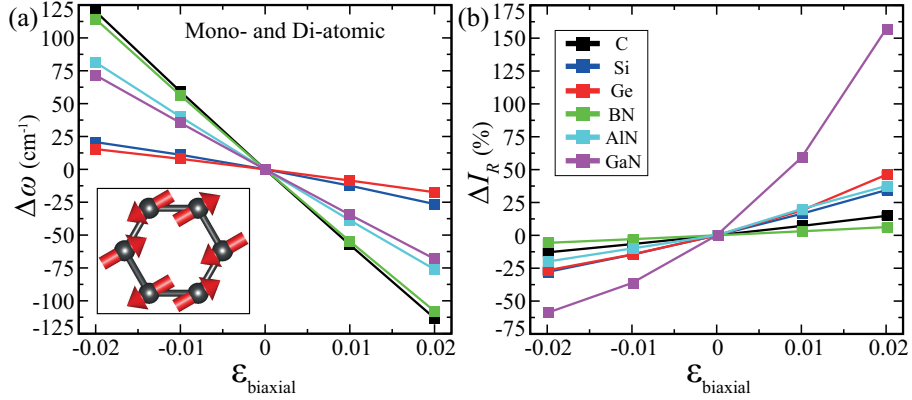


Figure 8.5. The response of activity of Raman active modes to the applied biaxial strain for single-layer (a) MoS₂, (b) WS₂, (c) MoSe₂, and (d) WSe₂. The vibrational motions of atoms in corresponding phonon modes are shown below.

modes will be softer. For the response of Raman activity of the Raman active modes to the applied biaxial strain, we will discuss only the E' and A₁ phonon modes and their relative activities. For the unstrained crystal structures, the ratios of Raman activities of E' mode to A₁ mode ($\frac{I_{E'}}{I_{A_1}}$) are calculated to be 5.35, 0.53, 8.32, and 1.37 for single-layer MoS₂, MoSe₂, WS₂, and WSe₂, respectively. As a general behavior the in-plane and out-of-plane modes are affected oppositely from the applied biaxial strain. When the single-layer material is compressed about 2%, the activity of A₁ phonon mode increases while the activity of E' decreases. Therefore, we will expect that the ratio ($\frac{I_{E'}}{I_{A_1}}$) gets smaller than its unstrained value. For the maximum compression (-2%) the calculated ratios are, 0.87, 0.12, 1.11, and 0.26, respectively. It is seen that the significant change in these ratios can be a fingerprint for determining the amount of compressive strain on the single-layer TMDs. In contrast when the single-layer is stretched at a maximum strain (+2%), the activity of A₁ decreases and the ratio will increase. Our calculated values are 574.82, 4.47, 203.29, and 51.37, respectively. It is seen that the change in ratios of Raman activities is more sensitive to applied biaxial tensile strain. Thus, one can identify the amount of tensile strain originated in the structure by analyzing these activity ratios. The significant change in $\frac{I_{E'}}{I_{A_1}}$ for especially S-based TMDs occurs due to the sharp decrease in the Raman activity of A₁ phonon mode under tensile strain.

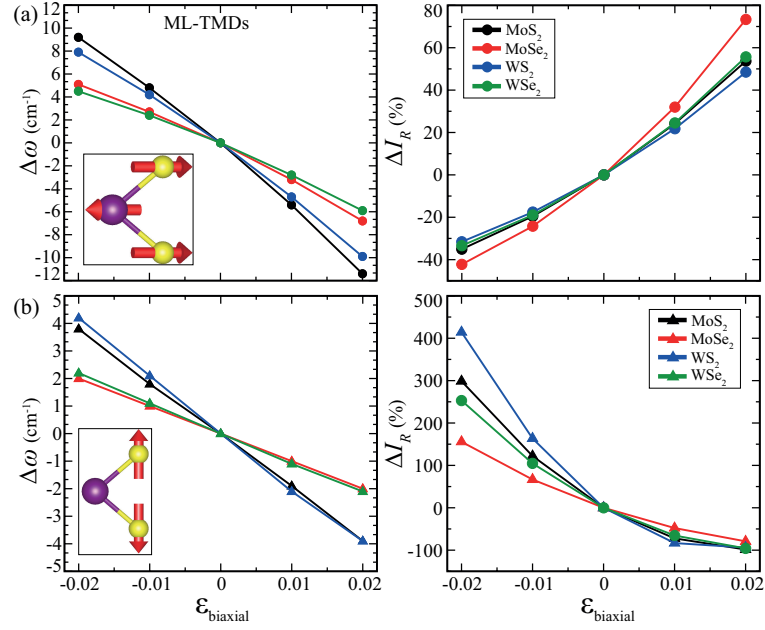


Figure 8.6. The response of frequencies of Raman active modes and their Raman activities to the applied biaxial strain for single-layers of TMDs for (a) E' mode and (b) A_1 .

8.1.4. Anisotropic Single-Layer Crystals

8.1.4.1. Rhenium Dichalcogenides (ReS_2 and ReSe_2) Single-Layer Crystals

Besides the perfect hexagonal lattice, there are also in-plane anisotropic single-layer crystals such as ReS_2 , ReSe_2 and black phosphorus (BP). As shown in Fig. 8.1(e), single-layers of ReS_2 and ReSe_2 have distorted 1T ($1T'$) crystal structure, which belongs to space group of $P\bar{1}$. (Tongay *et al.*, 2014) Unit cell of $1T'$ phase consists of eight chalcogen atoms coordinated around diamond-like Re_4 clusters. The angle between the in-plane unit cell vectors is 61.1° due to distortion in the crystal structure.

Monolayer crystals of Rhenium dichalcogenides (ReS_2 and ReSe_2) are both different than other well-known 2D TMDs which have 1H or 1T phase in their ground state. In the structure of ReS_2 and ReSe_2 a distortion occurs due to strong interaction between Re atoms which form Re_4 diamond like chains. Thus, the primitive unitcell of these in-

plane anisotropic single-layers can be represented by twelve atoms (four Re and eight chalcogen atoms). As a result of this unitcell configuration, there are totally 36 phonon modes for these two single-layers 3 of which are acoustic. Due to their distorted and anisotropic crystal structure, all of the Raman active phonon modes are non-degenerate modes. The 18 of the 36 phonon modes of single-layer ReS₂ and ReSe₂ are known to be Raman active from the group theory (Feng *et al.*, 2015).

First, we analyze the Raman spectrum of single-layer ReS₂. The total 18 Raman active phonon modes of single-layer ReS₂ can be divided into A_g (representing out-of-plane motion of atoms), E_g (representing in-plane motion of atoms), and the other modes in which both motions are coupled. There are 4 A_g phonon modes for single-layer ReS₂ two of which contain the motion of Re atoms and the other two contain motion of S atoms. The modes calculated at frequencies 132.6 and 139.9 cm⁻¹ represent the out-of-plane motion of Re atoms while the modes at 429.0 and 402.7 cm⁻¹ represent that of S atoms. Our calculated Raman activities for these A_g modes demonstrate that the activities of the low frequency modes that correspond to the motion of Re atoms, are smaller than those for the modes of S atoms. This is expectable since the bonding between Re atoms in a Re₄ cluster is stronger than that of a Re-S bond. Thus, the response of the vibration of Re atoms to the external incident light will be smaller. The total number of E_g modes for single-layer ReS₂ is known to be 6 four of which represent the in-plane motion of Re atoms while the other two represent that of S atoms. The same frequency trend is calculated for these E_g modes that is the motion of Re atoms occur again at lower frequencies than those of S atoms. Our calculated frequencies are 151.3, 165.0, 218.9, and 239.5 cm⁻¹ for the E_g phonon modes of Re atoms and 298.2 and 307.0 cm⁻¹ for those of S atoms. The calculated Raman activities of these modes also indicate the strong bonding between Re atoms in a Re₄ cluster. The remaining 8 Raman active modes represent the both in-plane and out-of-plane motion of Re and S atoms. Six of these modes contain the knowledge about the motion of only S atoms while for the other two modes both Re and S atoms are vibrating. Since an opposite trend is observed for the responses of A_g and E_g phonon modes to the applied biaxial strain, the responses of these coupled phonon modes will totally be smaller than those of A_g and E_g modes, separately. When the Raman activities of other modes are analyzed, it is seen that there are no significant changes in the activities which can be a result of rigidity of single-layer ReS₂. Because, at this level of applied strain ($\pm 2\%$) no significant deformations can be observed due to the formed Re₄ clusters in the structure. The most significant change is observed for the coupled phonon mode with frequency 412.0 cm⁻¹. In this mode the motion of atoms in out-of-

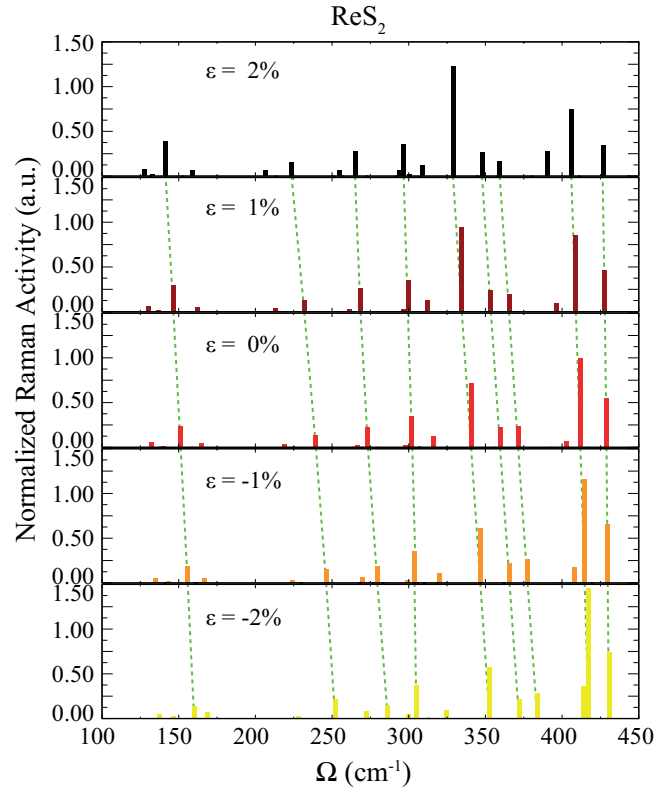


Figure 8.7. The response of frequencies and Raman activities of 18 Raman active modes of single-layer ReS_2 to the biaxial strain.

plane direction is dominant to that of in-plane. Thus, the activity of the mode displays a decreasing trend under tensile strain at a rate of 36% while a rate of increment (47%) is calculated under compressive strain.

In the case of single-layer ReSe_2 , the frequencies of the Raman active phonon modes significantly change due to same reasons mentioned for other 2D single-layers in this study. When S atoms are replaced by Se atoms, the Re-Se bond lengths gets larger and so the lattice. This results in a decrease of in-plane stiffness in the single-layer which results in softening of the phonon modes. Therefore, the highest Raman active phonon mode of single-layer ReSe_2 is calculated at 290.7 cm^{-1} which is found as 429.0 cm^{-1} for single-layer ReS_2 . The A_g phonon modes of Re atoms are calculated to be at frequencies 106.5 and 116.0 cm^{-1} while they are found at 157.0 and 176.2 cm^{-1} for the A_g phonon modes of Se atoms. As it is seen there is a large difference in the frequencies of out-of-plane modes representing the motions of chalcogen atoms. Since the mass of Se atom is larger than that of S atom, the frequency of the modes for S atoms is much higher than that of Se atoms. The response of the Raman active modes of single-layer ReSe_2 to

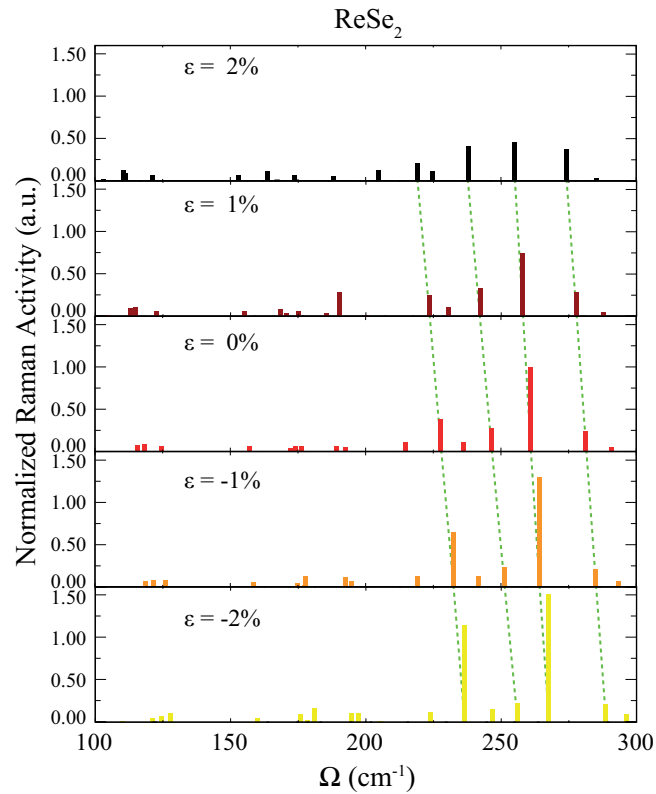


Figure 8.8. The response of frequencies and Raman activities of 18 Raman active modes of single-layer ReSe₂ to the biaxial strain.

applied strain can be significantly detected for the most intense peak which is at 260.9 cm⁻¹. This Raman active mode describes the coupled motion of both Re and Se atoms and the calculated to be the most intense peak in 18 peaks. Under compressive strain the activity of this mode increases about 50% of its unstrained value while it decreases about 55%. As it is seen the response of the mode is approximately symmetric. This mode can be a finger print in experiments to detect the stress on the single-layer ReSe₂. However, due to the strong Re-Re bonds in these two single-layers, one can not observe significant changes in the relative activities of Raman active modes in these single-layers.

8.1.4.2. Monolayer Black Phosphorus Single-Layer Crystal

Monolayer black phosphorus is a recently synthesized, in-plane anisotropic member of 2D single-layer family. Due to its puckered crystal structure (see Fig. 8.1(e)), single-layer BP possesses anisotropic physical properties which make this material an

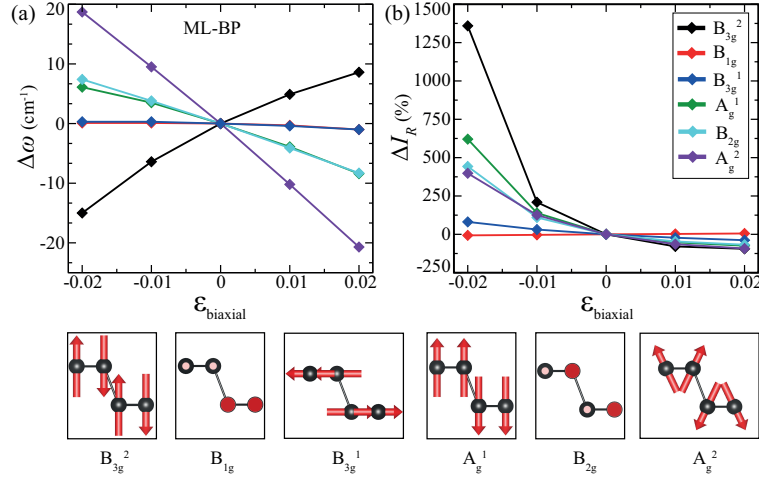


Figure 8.9. (a) The response of frequencies and (b) Raman activities of 6 Raman active modes of single-layer BP to the biaxial strain. Vibrational motion of P atoms in each phonon mode are given below.

important candidate for various applications. There are 4 P atoms in its rectangular primitive unitcell. The crystal structure of single-layer BP belongs to $Cmca$ space group.

Phonon-band structure of single-layer BP demonstrates that due to its 4-atomic primitive unitcell, totally 12 phonon modes exist 3 of which are acoustical phonon branches. According to the group theory analysis, single-layer BP has 6 Raman active phonon modes which are called as B_{1g} , B_{3g}^1 , A_g^1 , B_{3g}^2 , B_{2g} , and A_g^2 . The Raman active modes B_{1g} , B_{3g}^1 , B_{3g}^2 , and B_{2g} represent the in-plane vibration of P atoms while A_g^1 and A_g^2 represent out-of-plane motion. Although, it has 6 Raman active phonon modes only 3 of them (A_g^1 , B_{2g} , and A_g^2) exhibit prominent Raman scattering intensity as observed in experiments (Wang *et al.*, 2015; Favron *et al.*, 2015). Our calculated frequencies are 352.1, 424.2, and 455.2 cm⁻¹ for A_g^1 , B_{2g} , and A_g^2 , respectively. When compared with the reported experimental results(361, 438, and 466 cm⁻¹ for A_g^1 (Wang *et al.*, 2015), B_{2g} (Wang *et al.*, 2015), and A_g^2 (Wang *et al.*, 2015), respectively), our calculated frequencies are underestimated due to our methodology (GGA+vdW). For the unstrained single-layer BP, calculated Raman activities demonstrate that the A_g^1 and A_g^2 have much higher activities than that of B_{2g} which was also observed in the experiment (Favron *et al.*, 2015). However, since the relative intensities of Raman active modes depend strongly on the experimental conditions, here we will focus on the response of these modes to applied strain.

When single-layer BP is biaxially compressed up to 2%, the frequency of A_g^2

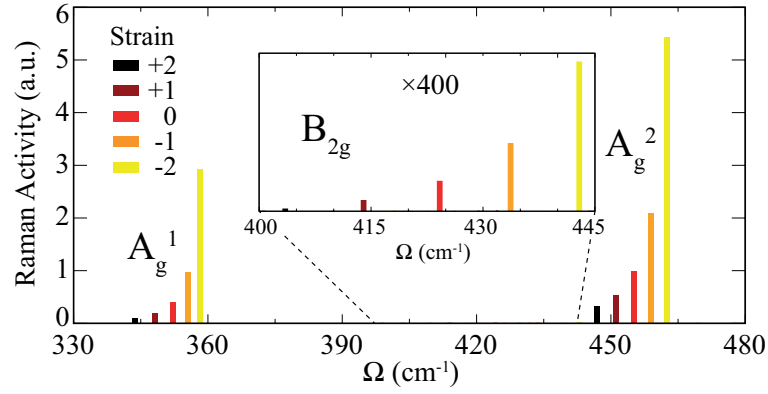


Figure 8.10. The response of 3 prominent Raman active modes of single-layer BP to the applied biaxial strain.

phonon mode displays a hardening from 455.2 to 462.6 cm^{-1} while a softening to 446.9 cm^{-1} is found under 2% tensile biaxial strain. The Raman activity of A_g^2 phonon mode is highly affected by the applied strain that it displays the same trend calculated for single-layer TMDs. If we normalize the Raman activity of this peak to 1, we find that the Raman activity of A_g^2 increases up to 5.4 times of its unstrained value under 2% of compressive strain. However, its Raman activity is found to be less sensitive to tensile strain when compared with that of compressive strain. Our results demonstrate that under 2% of tensile strain, the Raman activity decreases about 68% of its initial value which is much lower than that of compressive value. The frequency of B_{2g} phonon mode displays the same trend as the A_g^2 mode under biaxial strain. A softening to 403.5 cm^{-1} and a hardening to 442.9 cm^{-1} are found for the frequency of B_{2g} phonon mode under tensile and compressive strains, respectively. It is seen that for the strain range of $\pm 2\%$, the response of frequency of B_{2g} is much larger than that of A_g^2 mode. The calculated Raman activity of B_{2g} phonon mode is approximately 375 times smaller than that of the value for A_g^2 mode for the unstrained crystal structure. For the Raman activity of B_{2g} mode nearly a symmetric response is calculated under compressive and tensile biaxial strains. We find that the activity of this mode decreases(increases) about 10 times of its unstrained value under tensile(compressive) biaxial strains. Due to the out-of-plane nature of the mode, the same trend is also illustrated for B_{2g} mode. Another characteristic Raman active mode of single-layer BP is A_g^1 which represents the out-of-plane vibrations of the P atoms in upper and lower layer of single-layer BP in opposite directions. The frequency of this phonon mode softens to 343.7 cm^{-1} under 2% of tensile strain while it hardens to 358.2 cm^{-1}

under that of compressive strain. The calculated Raman activity of A_g^1 phonon mode is in the order of that of A_g^2 mode in unstrained structure. Since the two modes display the same trend under biaxial strain, it will be meaningful to compare the Raman activity of A_g^1 with its unstrained value. When 2% of compressive strain is applied, the Raman activity of A_g^1 increases about 7 times of its unstrained value while a decrease to 1/4 of its initial value.

As we mentioned, totally 6 Raman active modes exist for single-layer BP 3 of which have very low Raman activities (at the order of 10^{-5} of the value of A_g^2 mode). The Raman active modes B_{1g} and B_{3g}^1 are calculated to have frequencies 193.8 and 232.8 cm^{-1} , respectively. Our results show that both the frequencies and their Raman activities are mostly insensitive to the applied biaxial strain. A small amount of shift, from 193.8 to 192.8 cm^{-1} , is found for B_{1g} while a shift from 232.8 to 231.8 cm^{-1} is found for B_{3g}^1 under tensile strain. The response of frequencies is about 1 cm^{-1} which is very small when compared to other Raman active modes of single-layer BP. Their frequency responses to the compressive strain are also very small (193.8 to 193.9 cm^{-1} and 232.8 to 233.1 cm^{-1} for B_{1g} and B_{3g}^1 , respectively). Thus, the frequencies of these two Raman active modes are not key for determination of the strain on the structure. In addition to their frequencies, Raman activities of B_{1g} and B_{3g}^1 modes are mostly insensitive to the applied biaxial strain. We find that the activities mostly stay in the same range of their unstrained values. So, the direct detection of these modes in experiments under biaxial strain will not be clear as in the unstrained case.

8.2. Conclusions

In this study, the first-order off-resonant Raman spectra of 2D single-layers of mono-atomic (graphene, Si, and Ge), diatomic (h -BN, h -AlN, and h -GaN), in-plane isotropic TMDs (MoS_2 , MoSe_2 , WS_2 , and WSe_2), and in-plane anisotropic crystals (ReS_2 , ReSe_2 , and BP) and their strain-dependent behaviors were investigated by performing DFT-based calculations. Our results well fit into the reported experimental results for the first-order off-resonant Raman activities. In addition, the effect of biaxial strain on the Raman spectra of these single-layer crystals was analyzed in terms of their phonon frequencies and Raman activities. Our findings can be summarized as follows; (i) strain can be directly observed in Raman scattering experiments by the knowledge of the peak positions of Raman active phonon modes, (ii) the ZO phonon mode of the single-layer Si and Ge disappear under sufficient tensile strain, (iii) in the case of isotropic single-layer TMDs

(MoS₂, MoSe₂, WS₂, and WSe₂) the intensity ratio of E' to A₁ phonon mode, $\frac{I_{E'}}{I_{A_1}}$, is a key for the determination of the induced strain since this ratio significantly increases when a tensile strain is applied while it decreases under compressive strain due to the opposite responses of these phonon modes to the applied strain, and (iv) finally, a remarkable point for the anisotropic single-layers of ReX₂ is that there is no significant change in Raman intensities under strain. Our study elucidates the substrate-induced strain effect on Raman spectrum of the several single-layer materials. This is of importance for the characterization and utilization of the materials in nanoelectronic device applications.

CHAPTER 9

CONCLUSION

The electronic and mechanical properties of ultra-thin 2D materials are of great interest due to their use in optoelectronic and nanomechanical applications. Despite lack of a band gap in graphene, it has a large variety of use in most applications due to its extreme mechanical properties. Thus, searching for other novel 2D monolayer materials with even small or large electronic band gaps became an important issue.

In this thesis, electronic, magnetic, and mechanical properties of novel 2D monolayer materials such as pentagonal monolayers, holey graphene crystals, Ga-chalcogenides, functionalized ReS_2 , heterobilayer crystal structure of $\text{Mg}(\text{OH})_2$ and WS_2 , and other novel 2D monolayer materials were investigated by means of first-principles calculations based on DFT. Following the prediction of monolayer p-graphene, we demonstrated that penta- B_2N_4 can exist as a dynamically stable auxetic material. Even though penta- B_4N_2 is energetically feasible, it was found to be dynamically unstable monolayer. Motivated by the successful synthesis of monolayer C_2N , we predicted the feasibility of other monolayer holey graphene structures with As or P atoms instead of N atom. Calculated cohesive energies suggest that these two monolayer crystals are potential candidate for experimental synthesis with their mechanically flexible properties.

A detailed mechanical property analysis was demonstrated for monolayers of Ga-monochalcogenides (GaS and GaSe). It was shown that these two monolayer structures are highly flexible materials which can be important for their flexomechanical applications. In addition, their electronic and mechanical properties were shown to be tunable under external biaxial strain and electron charging. The mechanical properties of in-plane anisotropic monolayer ReS_2 and effect of hydrogenation on its structural, electronic, and mechanical properties were reported as another study. We found that full hydrogenation of monolayer ReS_2 lead to the formation of a new, dynamically stable structural phase which is mechanically more anisotropic and flexible when compared with its bare structure.

Apart from mechanical properties, electronic properties of a possible heterobilayer structure composed of monolayers $\text{Mg}(\text{OH})_2$ and WS_2 were investigated under the effect of an external out-of-plane electric field. It was demonstrated that electronically a transition from type-II (staggered) heterobilayer to type-I (straddling) heterobilayer can be observed after a critical value of the external field. In addition, it was predicted that

the low energy spectrum of the heterobilayer are dominated by the intralayer excitons of WS₂ monolayer.

The Raman measurement is a powerful and commonly used tool for characterization of 2D materials. In addition to experimental observations, the theoretical investigations of Raman intensities take an important place in scientific community. In this thesis, we also investigated the effect of biaxial strain on the Raman spectra of novel 2D monolayer materials. Our results demonstrated that strain can significantly affect the position(frequency) and intensity of Raman active modes in these materials which can be a finger print for determination of the effect of substrates on the synthesized monolayer material. We believe that our findings in this thesis will be helpful; (i) to understand the limitations of both elastic and non-elastic mechanical properties of 2D monolayer materials for their applications in nanomechanics and (ii) to distinguish the structural phases of a monolayer material through its Raman spectrum.

REFERENCES

- Alcock, N. and A. Kjekshus (1965). The crystal structure of reSe_2 . *Acta Chem. Scand* 19(1), 79.
- Alfè, D. (2009). Phon: A program to calculate phonons using the small displacement method. *Computer Physics Communications* 180(12), 2622–2633.
- Alfe, D. (2009). Phon: A program to calculate phonons using the small displacement method. *Computer Physics Communications* 180(12), 2622–2633.
- Aono, T., K. Kase, and A. Kinoshita (1993). Near-blue photoluminescence of zn-doped gas single-crystals. *Journal of Applied Physics* 74(4), 2818–2820.
- Aslan, O. B., D. A. Chenet, A. M. van der Zande, J. C. Hone, and T. F. Heinz (2015). Linearly polarized excitons in single-and few-layer reSe_2 crystals. *Acs Photonics* 3(1), 96–101.
- Ataca, C., H. Sahin, and S. Ciraci (2012). Stable, single-layer mx_2 transition-metal oxides and dichalcogenides in a honeycomb-like structure. *Journal of Physical Chemistry C* 116(16), 8983–8999.
- Bacaksiz, C., H. Sahin, H. Ozaydin, S. Horzum, R. Senger, and F. Peeters (2015). Hexagonal aln : Dimensional-crossover-driven band-gap transition. *Physical Review B* 91(8), 085430.
- Berger, C., Z. Song, X. Li, X. Wu, N. Brown, C. Naud, D. Mayou, T. Li, J. Hass, A. N. Marchenkov, E. H. Conrad, P. N. First, and W. A. de Heer (2006). Electronic confinement and coherence in patterned epitaxial graphene. *Science* 312(5777), 1191–1196.
- Berkdemir, A., H. R. Gutiérrez, A. R. Botello-Méndez, N. Perea-López, A. L. Elías, C.-I. Chia, B. Wang, V. H. Crespi, F. López-Urías, J.-C. Charlier, *et al.* (2013). Identification of individual and few layers of ws_2 using raman spectroscopy. *Scientific reports* 3.
- Berseneva, N., A. Gulans, A. V. Krasheninnikov, and R. M. Nieminen (2013). Electronic structure of boron nitride sheets doped with carbon from first-principles calculations. *Physical Review B* 87(3).
- Bertolazzi, S., J. Brivio, and A. Kis (2011a). Stretching and breaking of ultrathin mos_2 . *ACS nano* 5(12), 9703–9709.
- Bertolazzi, S., J. Brivio, and A. Kis (2011b). Stretching and breaking of ultrathin mos_2 . *Acs Nano* 5(12), 9703–9709.
- Boker, T., R. Severin, A. Muller, C. Janowitz, R. Manzke, D. Voss, P. Kruger, A. Mazur, and J. Pollmann (2001). Band structure of mos_2 , mose_2 , and $\alpha\text{-mote}_2$: Angle-

- resolved photoelectron spectroscopy and ab initio calculations. *Physical Review B* 64(23).
- Born, M. and R. Oppenheimer (1927). Zur quantentheorie der molekeln. *Annalen der Physik* 389(20), 457–484.
- Burns, S. (1987). Negative poissons ratio materials. *Science* 238(4826), 551–551.
- Cai, H., J. Kang, H. Sahin, B. Chen, A. Suslu, K. Wu, F. Peeters, X. Meng, and S. Tongay (2016). Exciton pumping across type-i gallium chalcogenide heterojunctions. *Nanotechnology* 27(6), 065203.
- Çakır, D., H. Sahin, and F. M. Peeters (2014). Doping of rhenium disulfide monolayers: a systematic first principles study. *Physical Chemistry Chemical Physics* 16(31), 16771–16779.
- Cao, Q., F. Huang, Z. Zhuang, and Z. Lin (2012). A study of the potential application of nano-mg(oh)(2) in adsorbing low concentrations of uranyl tricarbonate from water. *Nanoscale* 4(7), 2423–2430.
- Castellanos-Gomez, A., M. Poot, G. A. Steele, H. S. van der Zant, N. Agrait, and G. Rubio-Bollinger (2012). Elastic properties of freely suspended mos2 nanosheets. *Advanced Materials* 24(6), 772–775.
- Castro, E. V., K. S. Novoselov, S. V. Morozov, N. M. R. Peres, J. M. B. L. Dos Santos, J. Nilsson, F. Guinea, A. K. Geim, and A. H. Castro Neto (2007). Biased bilayer graphene: Semiconductor with a gap tunable by the electric field effect. *Physical Review Letters* 99(21).
- Catti, M., G. Ferraris, S. Hull, and A. Pavese (1995). Static compression and h-disorder in brucite, mg(oh)(2), to 11 gpa - a powder neutron-diffraction study. *Physics and Chemistry of Minerals* 22(3), 200–206.
- Ceperley, D. M. and B. Alder (1980). Ground state of the electron gas by a stochastic method. *Physical Review Letters* 45(7), 566.
- Chang, K. and W. Chen (2011). L-cysteine-assisted synthesis of layered mos2/graphene composites with excellent electrochemical performances for lithium ion batteries. *Acs Nano* 5(6), 4720–4728.
- Charlier, J. C. and G. M. Rignanese (2001). Electronic structure of carbon nanocones. *Physical Review Letters* 86(26), 5970–5973.
- Chen, H., Y. Li, L. Huang, and J. Li (2015a). Influential electronic and magnetic properties of the gallium sulfide monolayer by substitutional doping. *Journal of Physical Chemistry C* 119(52), 29148–29156.

- Chen, H., Y. Li, L. Huang, and J. Li (2015b). Intrinsic defects in gallium sulfide monolayer: a first-principles study. *Rsc Advances* 5(63), 50883–50889.
- Chen, J.-H., C. Jang, S. Xiao, M. Ishigami, and M. S. Fuhrer (2008). Intrinsic and extrinsic performance limits of graphene devices on sio₂. *Nature nanotechnology* 3(4), 206–209.
- Chenet, D. A., O. B. Aslan, P. Y. Huang, C. Fan, A. M. van der Zande, T. F. Heinz, and J. C. Hone (2015a). In-plane anisotropy in mono- and few-layer res₂ probed by raman spectroscopy and scanning transmission electron microscopy. *Nano letters* 15(9), 5667–5672.
- Chenet, D. A., O. B. Aslan, P. Y. Huang, C. Fan, A. M. van der Zande, T. F. Heinz, and J. C. Hone (2015b). In-plane anisotropy in mono- and few-layer res₂ probed by raman spectroscopy and scanning transmission electron microscopy. *Nano letters* 15(9), 5667–5672.
- Chu, T., H. Ilatikhameneh, G. Klimeck, R. Rahman, and Z. Chen (2015). Electrically tunable bandgaps in bilayer mos₂. *Nano Letters* 15(12), 8000–8007.
- Colomban, P. (2003). Raman analyses and "smart" imaging of nanophases and nanosized materials. *Spectroscopy Europe* 15(6), 8–16.
- Colson, J. W. and W. R. Dichtel (2013). Rationally synthesized two-dimensional polymers. *Nature Chemistry* 5(6), 453–465.
- Colson, J. W., A. R. Woll, A. Mukherjee, M. P. Levendorf, E. L. Spitler, V. B. Shields, M. G. Spencer, J. Park, and W. R. Dichtel (2011). Oriented 2d covalent organic framework thin films on single-layer graphene. *Science* 332(6026), 228–231.
- Colton, R. J. and J. W. Rabalais (1976). Electronic-structure of some inorganic azides from x-ray electron-spectroscopy. *Journal of Chemical Physics* 64(8), 3481–3486.
- Cooper, R. C., C. Lee, C. A. Marianetti, X. Wei, J. Hone, and J. W. Kysar (2013). Non-linear elastic behavior of two-dimensional molybdenum disulfide. *Physical Review B* 87(3), 035423.
- Dai, L. (2013). Functionalization of graphene for efficient energy conversion and storage. *Accounts of Chemical Research* 46(1), 31–42.
- Dai, L., D. W. Chang, J.-B. Baek, and W. Lu (2012). Carbon nanomaterials for advanced energy conversion and storage. *Small* 8(8), 1130–1166.
- Desgranges, L., G. Calvarin, and G. Chevrier (1996). Interlayer interactions in m(oh)(2): A neutron diffraction study of mg(oh)(2). *Acta Crystallographica Section B-Structural Science* 52, 82–86.

- Dettoni, R., E. Cadelano, and L. Colombo (2012). Elastic fields and moduli in defected graphene. *Journal of Physics: Condensed Matter* 24(10), 104020.
- Drescher, T., F. Niefind, W. Bensch, and W. Gruenert (2012). Sulfide catalysis without coordinatively unsaturated sites: Hydrogenation, cis-trans isomerization, and h-2/d-2 scrambling over mos₂ and ws₂. *Journal of the American Chemical Society* 134(46), 18896–18899.
- Du, Y., J. Maassen, W. Wu, Z. Luo, X. Xu, and P. D. Ye (2016). Auxetic black phosphorus: a 2d material with negative poisson's ratio. *Nano Letters* 16(10), 6701–6708.
- Eda, G., H. Yamaguchi, D. Voiry, T. Fujita, M. Chen, and M. Chhowalla (2011). Photoluminescence from chemically exfoliated mos₂. *Nano Letters* 11(12), 5111–5116.
- El-Kaderi, H. M., J. R. Hunt, J. L. Mendoza-Cortes, A. P. Cote, R. E. Taylor, M. O'Keeffe, and O. M. Yaghi (2007). Designed synthesis of 3d covalent organic frameworks. *Science* 316(5822), 268–272.
- Elias, D. C., R. R. Nair, T. Mohiuddin, S. Morozov, P. Blake, M. Halsall, A. Ferrari, D. Boukhvalov, M. Katsnelson, A. Geim, *et al.* (2009). Control of graphene's properties by reversible hydrogenation: evidence for graphane. *Science* 323(5914), 610–613.
- Estrela, C., F. C. Pimenta, I. Y. Ito, and L. L. Bammann (1998). In vitro determination of direct antimicrobial effect of calcium hydroxide. *Journal of Endodontics* 24(1), 15–17.
- Fang, M., K. Wang, H. Lu, Y. Yang, and S. Nutt (2009). Covalent polymer functionalization of graphene nanosheets and mechanical properties of composites. *Journal of Materials Chemistry* 19(38), 7098–7105.
- Favron, A., E. Gaufrès, F. Fossard, N. Y. Tang, P. L. Lévesque, A. Loiseau, R. Leonelli, S. Francoeur, R. Martel, *et al.* (2015). Photooxidation and quantum confinement effects in exfoliated black phosphorus. *Nature materials* 14(8), 826.
- Feng, X., X. Ding, and D. Jiang (2012). Covalent organic frameworks. *Chemical Society Reviews* 41(18), 6010–6022.
- Feng, Y., W. Zhou, Y. Wang, J. Zhou, E. Liu, Y. Fu, Z. Ni, X. Wu, H. Yuan, F. Miao, *et al.* (2015). Raman vibrational spectra of bulk to monolayer re s₂ with lower symmetry. *Physical Review B* 92(5), 054110.
- Fermi, E. (1927). Statistical method to determine some properties of atoms. *Rend. Accad. Naz. Lincei* 6(602-607), 5.
- Ferrari, A. C. and D. M. Basko (2013). Raman spectroscopy as a versatile tool for study-

- ing the properties of graphene. *Nature nanotechnology* 8(4), 235–246.
- Frostig, H., T. Bayer, N. Dudovich, Y. C. Eldar, and Y. Silberberg (2015). Single-beam spectrally controlled two-dimensional raman spectroscopy. *Nature Photonics* 9(5), 339–343.
- Geim, A. K. and P. Kim (2008). Carbon wonderland. *Scientific American* 298(4), 90–97.
- Ghali, E., W. Dietzel, and K. U. Kainer (2004). General and localized corrosion of magnesium alloys: A critical review. *Journal of Materials Engineering and Performance* 13(1), 7–23.
- Gmitra, M., S. Konschuh, C. Ertler, C. Ambrosch-Draxl, and J. Fabian (2009). Band-structure topologies of graphene: Spin-orbit coupling effects from first principles. *Physical Review B* 80(23), 235431.
- Gong, K., F. Du, Z. Xia, M. Durstock, and L. Dai (2009). Nitrogen-doped carbon nanotube arrays with high electrocatalytic activity for oxygen reduction. *Science* 323(5915), 760–764.
- Gordienko, A. and A. Poplavnoi (2004). Electronic structure of heavy-metal azides. *Russian physics journal* 47(10), 1056–1061.
- Gordienko, A. B. and A. S. Poplavnoi (2005). Local structure of the chemical bond in metal azides calculated in a basis set of wannier functions. *Journal of Structural Chemistry* 46(6), 968–972.
- Gordienko, A. B., Y. N. Zhuravlev, and A. S. Poplavnoi (1996). Electronic structure of metal azides. *Physica Status Solidi B-Basic Solid State Physics* 198(2), 707–719.
- Gordon, R., D. Yang, E. Crozier, D. Jiang, and R. Frindt (2002). Structures of exfoliated single layers of ws 2, mos 2, and mose 2 in aqueous suspension. *Physical Review B* 65(12), 125407.
- Gouadec, G. and P. Colomban (2007). Raman spectroscopy of nanomaterials: How spectra relate to disorder, particle size and mechanical properties. *Progress in crystal growth and characterization of materials* 53(1), 1–56.
- Grantab, R., V. B. Shenoy, and R. S. Ruoff (2010). Anomalous strength characteristics of tilt grain boundaries in graphene. *Science* 330(6006), 946–948.
- Grima, J. N., S. Winczewski, L. Mizzi, M. C. Grech, R. Cauchi, R. Gatt, D. Attard, K. W. Wojciechowski, and J. Rybicki (2015). Tailoring graphene to achieve negative poisson’s ratio properties. *Advanced Materials* 27(8), 1455–1459.
- Grimme, S. (2006). Semiempirical gga-type density functional constructed with a long-

- range dispersion correction. *Journal of Computational Chemistry* 27(15), 1787–1799.
- Guinea, F., M. Katsnelson, and A. Geim (2009). Energy gaps, topological insulator state and zero-field quantum hall effect in graphene by strain engineering. *Nature Publishing Group*.
- Guzman, D. M. and A. Strachan (2014). Role of strain on electronic and mechanical response of semiconducting transition-metal dichalcogenide monolayers: An ab-initio study. *Journal of Applied Physics* 115(24), 243701.
- Hafeez, M., L. Gan, H. Li, Y. Ma, and T. Zhai (2016). Chemical vapor deposition synthesis of ultrathin hexagonal reSe flakes for anisotropic raman property and optoelectronic application. *Advanced Materials* 28(37), 8296–8301.
- Han, S. S., H. Furukawa, O. M. Yaghi, and I. Goddard, William A. (2008). Covalent organic frameworks as exceptional hydrogen storage materials. *Journal of the American Chemical Society* 130(35), 11580–+.
- Havel, M., D. Baron, and P. Colomban (2004). Raman/rayleigh imaging of nano-sized sic materials using the spatial correlation model. *Journal of materials science* 39(20), 6183–6190.
- He, K., C. Poole, K. F. Mak, and J. Shan (2013). Experimental demonstration of continuous electronic structure tuning via strain in atomically thin mos₂. *Nano letters* 13(6), 2931–2936.
- He, R., J.-A. Yan, Z. Yin, Z. Ye, G. Ye, J. Cheng, J. Li, and C. Lui (2016). Coupling and stacking order of reSe atomic layers revealed by ultralow-frequency raman spectroscopy. *Nano letters* 16(2), 1404–1409.
- Henkelman, G., A. Arnaldsson, and H. Jonsson (2006). A fast and robust algorithm for bader decomposition of charge density. *Computational Materials Science* 36(3), 354–360.
- Heyd, J., G. E. Scuseria, and M. Ernzerhof (2003). Hybrid functionals based on a screened coulomb potential. *Journal of Chemical Physics* 118(18), 8207–8215.
- Ho, C.-H., M.-H. Hsieh, and C.-C. Wu (2006). Photoconductance and photoresponse of layer compound photodetectors in the uv-visible region. *Review of Scientific Instruments* 77(11).
- Hohenberg, P. and W. Kohn (1964). Inhomogeneous electron gas. *Physical review* 136(3B), B864.
- Hou, D., F. Zhang, C. Ji, T. Hannon, H. Zhu, J. Wu, V. I. Levitas, and Y. Ma (2011). Phase transition and structure of silver azide at high pressure. *Journal of Applied*

Physics 110(2).

- Hu, P., Z. Wen, L. Wang, P. Tan, and K. Xiao (2012). Synthesis of few-layer gase nanosheets for high performance photodetectors. *Acs Nano 6(7)*, 5988–5994.
- Huang, C.-H., Y.-L. Jan, and W.-C. Lee (2011). Investigation of mg(o,oh) films prepared by chemical bath deposition as buffer layers for cu(in,ga)se-2 solar cells. *Journal of the Electrochemical Society 158(9)*, H879–H888.
- Huang, M., H. Yan, T. F. Heinz, and J. Hone (2010). Probing strain-induced electronic structure change in graphene by raman spectroscopy. *Nano letters 10(10)*, 4074–4079.
- Hüser, F., T. Olsen, and K. S. Thygesen (2013). How dielectric screening in two-dimensional crystals affects the convergence of excited-state calculations: Monolayer mos 2. *Physical Review B 88(24)*, 245309.
- Huser, F., T. Olsen, and K. S. Thygesen (2013). How dielectric screening in two-dimensional crystals affects the convergence of excited-state calculations: Monolayer mos2. *Physical Review B 88(24)*.
- Iijima, S. and T. Ichihashi (1993). Single-shell carbon nanotubes of 1-nm diameter. *Nature 363(6430)*, 603–605.
- Island, J. O., M. Buscema, M. Barawi, J. M. Clamagirand, J. R. Ares, C. Sánchez, I. J. Ferrer, G. A. Steele, H. S. van der Zant, and A. Castellanos-Gomez (2014). Ultrahigh photoresponse of few-layer tis3 nanoribbon transistors. *Advanced Optical Materials 2(7)*, 641–645.
- Jain, P., J. Sahariya, S. Mund, M. Sharma, and B. L. Ahuja (2013). Ab initio calculations for electronic and optical properties of explosive silver azide. *Computational Materials Science 72*, 101–106.
- Jariwala, B., D. Voiry, A. Jindal, B. A. Chalke, R. Bapat, A. Thamizhavel, M. Chhowalla, M. Deshmukh, and A. Bhattacharya (2016). Synthesis and characterization of res2 and rese2 layered chalcogenide single crystals. *Chemistry of Materials 28(10)*, 3352–3359.
- Jiang, J.-W. and H. S. Park (2014). Negative poisson’s ratio in single-layer black phosphorus. *arXiv preprint arXiv:1403.4326*.
- Jin, C., H. Lan, L. Peng, K. Suenaga, and S. Iijima (2009). Deriving carbon atomic chains from graphene. *Physical Review Letters 102(20)*.
- Jing, N., Q. Xue, C. Ling, M. Shan, T. Zhang, X. Zhou, and Z. Jiao (2012). Effect of defects on young’s modulus of graphene sheets: a molecular dynamics simulation. *Rsc Advances 2(24)*, 9124–9129.

- Kandemir, A., H. Yapicioglu, A. Kinaci, T. Çağın, and C. Sevik (2016). Thermal transport properties of mos2 and mose2 monolayers. *Nanotechnology* 27(5), 055703.
- Kang, J., H. Sahin, and F. M. Peeters (2015). Mechanical properties of monolayer sulphides: a comparative study between mos2, hfs2 and tis3. *Physical Chemistry Chemical Physics* 17(41), 27742–27749.
- Kim, K., A. Hsu, X. Jia, S. Kim, Y. Shi, M. Dresselhaus, T. Palacios, and J. Kong. *Acs nano* 2012, 6, 8583–8590.
- Kim, K., Z. Lee, W. Regan, C. Kisielowski, M. Crommie, and A. Zettl (2011). Grain boundary mapping in polycrystalline graphene. *ACS nano* 5(3), 2142–2146.
- Klein, A., S. Tiefenbacher, V. Eyert, C. Pettenkofer, and W. Jaegermann (2001). Electronic band structure of single-crystal and single-layer ws2: Influence of interlayer van der waals interactions. *Physical Review B* 64(20).
- Kohn, W. and L. J. Sham (1965). Self-consistent equations including exchange and correlation effects. *Physical review* 140(4A), A1133.
- Kresse, G. and J. Furthmuller (1996a). Efficiency of ab-initio total energy calculations for metals and semiconductors using a plane-wave basis set. *Computational Materials Science* 6(1), 15–50.
- Kresse, G. and J. Furthmuller (1996b). Efficient iterative schemes for ab initio total-energy calculations using a plane-wave basis set. *Physical Review B* 54(16), 11169–11186.
- Kroto, H. W., J. R. Heath, S. C. O'Brien, R. F. Curl, and R. E. Smalley (1985). C-60 - buckminsterfullerene. *Nature* 318(6042), 162–163.
- Kudin, K. N., G. E. Scuseria, and B. I. Yakobson (2001). C 2 f, bn, and c nanoshell elasticity from ab initio computations. *Physical Review B* 64(23), 235406.
- Kuzmenko, A., E. Van Heumen, F. Carbone, and D. Van Der Marel (2008). Universal optical conductance of graphite. *Physical review letters* 100(11), 117401.
- Lai, K., W.-B. Zhang, F. Zhou, F. Zeng, and B.-Y. Tang (2016). Bending rigidity of transition metal dichalcogenide monolayers from first-principles. *Journal of Physics D: Applied Physics* 49(18), 185301.
- Lamfers, H.-J., A. Meetsma, G. Wieggers, and J. De Boer (1996). The crystal structure of some rhenium and technetium dichalcogenides. *Journal of alloys and compounds* 241(1-2), 34–39.
- Late, D. J., B. Liu, J. Luo, A. Yan, H. Matte, M. Grayson, C. Rao, and V. P. Dravid (2012).

- Gas and gase ultrathin layer transistors. *Advanced Materials* 24(26), 3549–3554.
- Late, D. J., B. Liu, H. S. S. R. Matte, C. N. R. Rao, and V. P. Dravid (2012). Rapid characterization of ultrathin layers of chalcogenides on sio₂/si substrates. *Advanced Functional Materials* 22(9), 1894–1905.
- Lee, C., X. Wei, J. W. Kysar, and J. Hone (2008). Measurement of the elastic properties and intrinsic strength of monolayer graphene. *Science* 321(5887), 385–388.
- Lee, G.-H., R. C. Cooper, S. J. An, S. Lee, A. van der Zande, N. Petrone, A. G. Hammerberg, C. Lee, B. Crawford, W. Oliver, J. W. Kysar, and J. Hone (2013). High-strength chemical-vapor deposited graphene and grain boundaries. *Science* 340(6136), 1073–1076.
- Li, H., Z. Yin, Q. He, H. Li, X. Huang, G. Lu, D. W. H. Fam, A. I. Y. Tok, Q. Zhang, and H. Zhang (2012). Fabrication of single- and multilayer mos₂ film-based field-effect transistors for sensing no at room temperature. *Small* 8(1), 63–67.
- Li, L., Y. Yu, G. J. Ye, Q. Ge, X. Ou, H. Wu, D. Feng, X. H. Chen, and Y. Zhang (2014). Black phosphorus field-effect transistors. *Nature nanotechnology* 9(5), 372–377.
- Li, X., L. Basile, M. Yoon, C. Ma, A. A. Puzdovskiy, J. Lee, J. C. Idrobo, M. Chi, C. M. Rouleau, D. B. Geohegan, and K. Xiao (2015). Revealing the preferred interlayer orientations and stackings of two-dimensional bilayer gallium selenide crystals. *Angewandte Chemie-International Edition* 54(9), 2712–2717.
- Li, X., M.-W. Lin, A. A. Puzdovskiy, J. C. Idrobo, C. Ma, M. Chi, M. Yoon, C. M. Rouleau, I. I. Kravchenko, D. B. Geohegan, *et al.* (2014). Controlled vapor phase growth of single crystalline, two-dimensional gase crystals with high photoresponse. *Scientific reports* 4, 5497.
- Li, Y., L. Xu, H. Liu, and Y. Li (2014). Graphdiyne and graphyne: from theoretical predictions to practical construction. *Chemical Society Reviews* 43(8), 2572–2586.
- Lin, Q.-Y., G. Jing, Y.-B. Zhou, Y.-F. Wang, J. Meng, Y.-Q. Bie, D.-P. Yu, and Z.-M. Liao (2013). Stretch-induced stiffness enhancement of graphene grown by chemical vapor deposition. *ACS nano* 7(2), 1171–1177.
- Liu, C.-C., H. Jiang, and Y. Yao (2011). Low-energy effective hamiltonian involving spin-orbit coupling in silicene and two-dimensional germanium and tin. *Physical Review B* 84(19), 195430.
- Liu, E., Y. Fu, Y. Wang, Y. Feng, H. Liu, X. Wan, W. Zhou, B. Wang, L. Shao, C.-H. Ho, *et al.* (2015). Integrated digital inverters based on two-dimensional anisotropic res₂ field-effect transistors. *Nature communications* 6.

- Liu, F., P. Ming, and J. Li (2007). Ab initio calculation of ideal strength and phonon instability of graphene under tension. *Physical Review B* 76(6), 064120.
- Liu, H., A. T. Neal, Z. Zhu, Z. Luo, X. Xu, D. Tománek, and D. Y. Peide (2014). Phosphorene: an unexplored 2d semiconductor with a high hole mobility.
- Liu, K., Q. Yan, M. Chen, W. Fan, Y. Sun, J. Suh, D. Fu, S. Lee, J. Zhou, S. Tongay, *et al.* (2014). Elastic properties of chemical-vapor-deposited monolayer mos₂, ws₂, and their bilayer heterostructures. *Nano letters* 14(9), 5097–5103.
- Liu, N., J. Hong, R. Pidaparti, and X. Wang (2016). Fracture patterns and the energy release rate of phosphorene. *Nanoscale* 8(10), 5728–5736.
- Loh, K. P., Q. Bao, P. K. Ang, and J. Yang (2010). The chemistry of graphene. *Journal of Materials Chemistry* 20(12), 2277–2289.
- Lorchat, E., G. Froehlicher, and S. Berciaud (2016). Splitting of interlayer shear modes and photon energy dependent anisotropic raman response in n-layer rese₂ and res₂. *ACS nano* 10(2), 2752–2760.
- Lothe, J. H. J. and J. P. Hirth (1982). Theory of dislocations. *Wiley, New York*, 270.
- Lu, X., M. I. B. Utama, J. Lin, X. Gong, J. Zhang, Y. Zhao, S. T. Pantelides, J. Wang, Z. Dong, Z. Liu, *et al.* (2014). Large-area synthesis of monolayer and few-layer mose₂ films on sio₂ substrates. *Nano letters* 14(5), 2419–2425.
- Mahmood, J., E. K. Lee, M. Jung, D. Shin, I.-Y. Jeon, S.-M. Jung, H.-J. Choi, J.-M. Seo, S.-Y. Bae, S.-D. Sohn, N. Park, J. H. Oh, H.-J. Shin, and J.-B. Baek (2015). Nitrogenated holey two-dimensional structures. *Nature Communications* 6.
- Mak, K. F., K. He, C. Lee, G. H. Lee, J. Hone, T. F. Heinz, and J. Shan (2013). Tightly bound trions in monolayer mos₂. *Nature Materials* 12(3), 207–211.
- Mayorov, A. S., R. V. Gorbachev, S. V. Morozov, L. Britnell, R. Jalil, L. A. Ponomarenko, P. Blake, K. S. Novoselov, K. Watanabe, T. Taniguchi, *et al.* (2011). Micrometer-scale ballistic transport in encapsulated graphene at room temperature. *Nano letters* 11(6), 2396–2399.
- Moser, J., A. Barreiro, and A. Bachtold (2007). Current-induced cleaning of graphene. *Applied Physics Letters* 91(16), 163513.
- Murakami, T., T. Honjo, and T. Kuji (2011). Dos calculation analysis of new transparent conductor mg(oh)₂-c. *Materials Transactions* 52(8), 1689–1692.
- Nair, R. R., P. Blake, A. N. Grigorenko, K. S. Novoselov, T. J. Booth, T. Stauber, N. M. Peres, and A. K. Geim (2008). Fine structure constant defines visual transparency of

- graphene. *Science* 320(5881), 1308–1308.
- Nair, R. R., W. Ren, R. Jalil, I. Riaz, V. G. Kravets, L. Britnell, P. Blake, F. Schedin, A. S. Mayorov, S. Yuan, *et al.* (2010). Fluorographene: A two-dimensional counterpart of teflon. *small* 6(24), 2877–2884.
- Nasr Esfahani, D., O. Leenaerts, H. Sahin, B. Partoens, and F. Peeters (2015). Structural transitions in monolayer mos2 by lithium adsorption. *The Journal of Physical Chemistry C* 119(19), 10602–10609.
- Ni, Z. H., T. Yu, Y. H. Lu, Y. Y. Wang, Y. P. Feng, and Z. X. Shen (2008). Uniaxial strain on graphene: Raman spectroscopy study and band-gap opening. *ACS nano* 2(11), 2301–2305.
- Novoselov, K., D. Jiang, F. Schedin, T. Booth, V. Khotkevich, S. Morozov, and A. Geim (2005). Two-dimensional atomic crystals. *Proceedings of the National Academy of Sciences of the United States of America* 102(30), 10451–10453.
- Novoselov, K. S., A. K. Geim, S. V. Morozov, D. Jiang, M. I. Katsnelson, I. V. Grigorieva, S. V. Dubonos, and A. A. Firsov (2005). Two-dimensional gas of massless dirac fermions in graphene. *Nature* 438(7065), 197–200.
- Novoselov, K. S., A. K. Geim, S. V. Morozov, D. Jiang, Y. Zhang, S. V. Dubonos, I. V. Grigorieva, and A. A. Firsov (2004). Electric field effect in atomically thin carbon films. *Science* 306(5696), 666–669.
- Nye, J. F. (1985). *Physical properties of crystals: their representation by tensors and matrices*. Oxford university press.
- Osella, S., A. Narita, M. G. Schwab, Y. Hernandez, X. Feng, K. Muellen, and D. Beljonne (2012). Graphene nanoribbons as low band gap donor materials for organic photovoltaics: Quantum chemical aided design. *Acs Nano* 6(6), 5539–5548.
- Pan, H. (2014). Magnetic and electronic evolutions of hydrogenated vte2 monolayer under tension. *Scientific reports* 4, 7524.
- Perdew, J. P., K. Burke, and M. Ernzerhof (1996a). Generalized gradient approximation made simple. *Physical review letters* 77(18), 3865.
- Perdew, J. P., K. Burke, and M. Ernzerhof (1996b). Generalized gradient approximation made simple. *Physical Review Letters* 77(18), 3865–3868.
- Popov, I., G. Seifert, and D. Tomanek (2012). Designing electrical contacts to mos2 monolayers: A computational study. *Physical Review Letters* 108(15).
- Pradhan, N. R., A. McCreary, D. Rhodes, Z. Lu, S. Feng, E. Manousakis, D. Smirnov,

- R. Namburu, M. Dubey, A. R. Hight Walker, *et al.* (2015). Metal to insulator quantum-phase transition in few-layered res₂. *Nano letters* 15(12), 8377–8384.
- Qiao, X.-F., X.-L. Li, X. Zhang, W. Shi, J.-B. Wu, T. Chen, and P.-H. Tan (2015). Substrate-free layer-number identification of two-dimensional materials: A case of mo_{0.5}w_{0.5}s₂ alloy. *Applied Physics Letters* 106(22), 223102.
- Radisavljevic, B., A. Radenovic, J. Brivio, i. V. Giacometti, and A. Kis (2011). Single-layer mos₂ transistors. *Nature nanotechnology* 6(3), 147–150.
- Ramakrishna Matte, H., A. Gomathi, A. K. Manna, D. J. Late, R. Datta, S. K. Pati, and C. Rao (2010). Mos₂ and ws₂ analogues of graphene. *Angewandte Chemie* 122(24), 4153–4156.
- Raman, C. V. (1928). A new radiation.
- Ramasubramaniam, A. (2012). Large excitonic effects in monolayers of molybdenum and tungsten dichalcogenides. *Physical Review B* 86(11).
- Ruiz-Vargas, C. S., H. L. Zhuang, P. Y. Huang, A. M. van der Zande, S. Garg, P. L. McEuen, D. A. Muller, R. G. Hennig, and J. Park (2011). Softened elastic response and unzipping in chemical vapor deposition graphene membranes. *Nano letters* 11(6), 2259–2263.
- Sahin, H. (2015). Structural and phononic characteristics of nitrogenated holey graphene. *Physical Review B* 92(8).
- Sahin, H., S. Cahangirov, M. Topsakal, E. Bekaroglu, E. Akturk, R. T. Senger, and S. Ciraci (2009). Monolayer honeycomb structures of group-iv elements and iii-v binary compounds: First-principles calculations. *Physical Review B* 80(15).
- Sahin, H. and S. Ciraci (2012). Chlorine adsorption on graphene: Chlorographene. *The Journal of Physical Chemistry C* 116(45), 24075–24083.
- Sahin, H. and F. M. Peeters (2013). Adsorption of alkali, alkaline-earth, and 3 d transition metal atoms on silicene. *Physical Review B* 87(8), 085423.
- Şahin, H., M. Topsakal, and S. Ciraci (2011). Structures of fluorinated graphene and their signatures. *Physical Review B* 83(11), 115432.
- Schmidt, C. L., R. Dinnebier, U. Wedig, and M. Jansen (2007). Crystal structure and chemical bonding of the high-temperature phase of agn₃. *Inorganic Chemistry* 46(3), 907–916.
- Seayad, A. M. and D. M. Antonelli (2004). Recent advances in hydrogen storage in metal-containing inorganic nanostructures and related materials. *Advanced Materials* 16(9-

10), 765–777.

- Shi, H., H. Pan, Y.-W. Zhang, and B. I. Yakobson (2013). Quasiparticle band structures and optical properties of strained monolayer mos2 and ws2. *Physical Review B* 87(15).
- Sofo, J. O., A. S. Chaudhari, and G. D. Barber (2007). Graphane: A two-dimensional hydrocarbon. *Physical Review B* 75(15), 153401.
- Song, L., L. Ci, H. Lu, P. B. Sorokin, C. Jin, J. Ni, A. G. Kvashnin, D. G. Kvashnin, J. Lou, B. I. Yakobson, and P. M. Ajayan (2010). Large scale growth and characterization of atomic hexagonal boron nitride layers. *Nano Letters* 10(8), 3209–3215.
- Suslu, A., K. Wu, H. Sahin, B. Chen, S. Yang, H. Cai, T. Aoki, S. Horzum, J. Kang, F. M. Peeters, and S. Tongay (2016). Unusual dimensionality effects and surface charge density in 2d mg(oh)(2). *Scientific Reports* 6.
- Tabert, C. J. and E. J. Nicol (2013). Ac/dc spin and valley hall effects in silicene and germanene. *Physical Review B* 87(23), 235426.
- Tan, P., W. Han, W. Zhao, Z. Wu, K. Chang, H. Wang, Y. Wang, N. Bonini, N. Marzari, G. Savini, *et al.* (2011). The shear mode of multi-layer graphene. *arXiv preprint arXiv:1106.1146*.
- Tao, J., W. Shen, S. Wu, L. Liu, Z. Feng, C. Wang, C. Hu, P. Yao, H. Zhang, W. Pang, *et al.* (2015). Mechanical and electrical anisotropy of few-layer black phosphorus. *ACS nano* 9(11), 11362–11370.
- Tatsuyam.C, Y. Watanabe, Hamaguch.C, and J. Nakai (1970). Some optical properties of layer-type semiconductor gate. *Journal of the Physical Society of Japan* 29(1), 150.
- Thomalla, M. and H. Tributsch (2006). Photosensitization of nanostructured tio2 with ws2 quantum sheets. *Journal of Physical Chemistry B* 110(24), 12167–12171.
- Thomas, L. H. (1927). The calculation of atomic fields. In *Mathematical Proceedings of the Cambridge Philosophical Society*, Volume 23, pp. 542–548. Cambridge University Press.
- Tongay, S., H. Sahin, C. Ko, A. Luce, W. Fan, K. Liu, J. Zhou, Y.-S. Huang, C.-H. Ho, J. Yan, D. F. Ogletree, S. Aloni, J. Ji, S. Li, J. Li, F. M. Peeters, and J. Wu (2014). Monolayer behaviour in bulk res2 due to electronic and vibrational decoupling. *Nature Communications* 5.
- Topsakal, M., E. Aktuerk, and S. Ciraci (2009). First-principles study of two- and one-dimensional honeycomb structures of boron nitride. *Physical Review B* 79(11).

- Torun, E., H. Sahin, and F. M. Peeters (2016). Optical properties of gas-ca(oh)(2) bilayer heterostructure. *Physical Review B* 93(7).
- Tsen, A. W., L. Brown, M. P. Levendorf, F. Ghahari, P. Y. Huang, R. W. Havener, C. S. Ruiz-Vargas, D. A. Muller, P. Kim, and J. Park (2012). Tailoring electrical transport across grain boundaries in polycrystalline graphene. *Science* 336(6085), 1143–1146.
- Tsipas, P., S. Kassavetis, D. Tsoutsou, E. Xenogiannopoulou, E. Golias, S. Giamini, C. Grazianetti, D. Chiappe, A. Molle, M. Fanciulli, *et al.* (2013). Evidence for graphite-like hexagonal aln nanosheets epitaxially grown on single crystal ag (111). *Applied Physics Letters* 103(25), 251605.
- Wan, J., J.-W. Jiang, and H. S. Park (2017). Negative poisson's ratio in graphene oxide. *Nanoscale* 9(11), 4007–4012.
- Wang, L., A. Kutana, X. Zou, and B. I. Yakobson (2015). Electro-mechanical anisotropy of phosphorene. *Nanoscale* 7(21), 9746–9751.
- Wang, Q. H., K. Kalantar-Zadeh, A. Kis, J. N. Coleman, and M. S. Strano (2012). Electronics and optoelectronics of two-dimensional transition metal dichalcogenides. *Nature nanotechnology* 7(11), 699–712.
- Wang, X., A. M. Jones, K. L. Seyler, V. Tran, Y. Jia, H. Zhao, H. Wang, L. Yang, X. Xu, and F. Xia (2015). Highly anisotropic and robust excitons in monolayer black phosphorus. *Nature nanotechnology* 10(6), 517–521.
- Wang, X., X. Li, L. Zhang, Y. Yoon, P. K. Weber, H. Wang, J. Guo, and H. Dai (2009). N-doping of graphene through electrothermal reactions with ammonia. *Science* 324(5928), 768–771.
- Warner, J. H., E. R. Margine, M. Mukai, A. W. Robertson, F. Giustino, and A. I. Kirkland (2012). Dislocation-driven deformations in graphene. *Science* 337(6091), 209–212.
- Wei, D., Y. Liu, Y. Wang, H. Zhang, L. Huang, and G. Yu (2009). Synthesis of n-doped graphene by chemical vapor deposition and its electrical properties. *Nano Letters* 9(5), 1752–1758.
- Wei, Y., J. Wu, H. Yin, X. Shi, R. Yang, and M. Dresselhaus (2012). The nature of strength enhancement and weakening by pentagon–heptagon defects in graphene. *Nature materials* 11(9), 759–763.
- Wildervanck, J. and F. Jellinek (1971). The dichalcogenides of technetium and rhenium. *Journal of the Less Common Metals* 24(1), 73–81.
- Wilson, J. and A. Yoffe (1969). The transition metal dichalcogenides discussion and interpretation of the observed optical, electrical and structural properties. *Advances in*

Physics 18(73), 193–335.

- Wolverson, D., S. Crampin, A. S. Kazemi, A. Ilie, and S. J. Bending (2014). Raman spectra of monolayer, few-layer, and bulk reSe₂: An anisotropic layered semiconductor. *Acs Nano* 8(11), 11154–11164.
- Wu, J.-B., Z.-X. Hu, X. Zhang, W.-P. Han, Y. Lu, W. Shi, X.-F. Qiao, M. Ijäs, S. Milana, W. Ji, *et al.* (2015). Interface coupling in twisted multilayer graphene by resonant raman spectroscopy of layer breathing modes. *ACS nano* 9(7), 7440–7449.
- Wu, J.-B., X. Zhang, M. Ijäs, W.-P. Han, X.-F. Qiao, X.-L. Li, D.-S. Jiang, A. C. Ferrari, and P.-H. Tan (2014). Resonant raman spectroscopy of twisted multilayer graphene. *Nature communications* 5, 5309.
- Xiang, Z. and D. Cao (2013). Porous covalent-organic materials: synthesis, clean energy application and design. *Journal of Materials Chemistry A* 1(8), 2691–2718.
- Xu, B., H. Xiang, Q. Wei, J. Q. Liu, Y. D. Xia, J. Yin, and Z. G. Liu (2015). Two-dimensional graphene-like c₂n: an experimentally available porous membrane for hydrogen purification. *Physical Chemistry Chemical Physics* 17(23), 15115–15118.
- Xu, Y., W. Hong, H. Bai, C. Li, and G. Shi (2009). Strong and ductile poly (vinyl alcohol)/graphene oxide composite films with a layered structure. *Carbon* 47(15), 3538–3543.
- Xue, Y., J. Liu, H. Chen, R. Wang, D. Li, J. Qu, and L. Dai (2012). Nitrogen-doped graphene foams as metal-free counter electrodes in high-performance dye-sensitized solar cells. *Angewandte Chemie-International Edition* 51(48), 12124–12127.
- Yagmurcukardes, M., C. Bacaksiz, R. T. Senger, and H. Sahin (2017). Hydrogen-induced structural transition in single layer reSe₂. *2D Materials* 4(3), 035013.
- Yagmurcukardes, M., R. Senger, F. Peeters, and H. Sahin (2016). Mechanical properties of monolayer gas and gas crystals. *Physical Review B* 94(24), 245407.
- Yamamoto, A., A. Syouji, T. Goto, E. Kulatov, K. Ohno, Y. Kawazoe, K. Uchida, and N. Miura (2001). Excitons and band structure of highly anisotropic gate single-crystals. *Physical Review B* 64(3).
- Yang, S., C. Wang, H. Sahin, H. Chen, Y. Li, S.-S. Li, A. Suslu, F. M. Peeters, Q. Liu, J. Li, *et al.* (2015). Tuning the optical, magnetic, and electrical properties of reSe₂ by nanoscale strain engineering. *Nano letters* 15(3), 1660–1666.
- Yu, Q., L. A. Jauregui, W. Wu, R. Colby, J. Tian, Z. Su, H. Cao, Z. Liu, D. Pandey, D. Wei, *et al.* (2011). Control and characterization of individual grains and grain boundaries in graphene grown by chemical vapour deposition. *Nature materials* 10(6), 443–449.

- Yu, Z. G., Y. Cai, and Y.-W. Zhang (2015). Robust direct bandgap characteristics of one- and two-dimensional res₂. *Scientific reports* 5.
- Zeng, H., C. Zhi, Z. Zhang, X. Wei, X. Wang, W. Guo, Y. Bando, and D. Golberg (2010). "white graphenes": boron nitride nanoribbons via boron nitride nanotube unwrapping. *Nano letters* 10(12), 5049–5055.
- Zhang, J., F. Zhao, Z. Zhang, N. Chen, and L. Qu (2013). Dimension-tailored functional graphene structures for energy conversion and storage. *Nanoscale* 5(8), 3112–3126.
- Zhang, R., B. Li, and J. Yang (2015). Effects of stacking order, layer number and external electric field on electronic structures of few-layer c_{2n}-h_{2d}. *Nanoscale* 7(33), 14062–14070.
- Zhang, S., J. Zhou, Q. Wang, X. Chen, Y. Kawazoe, and P. Jena (2015). Penta-graphene: A new carbon allotrope. *Proceedings of the National Academy of Sciences of the United States of America* 112(8), 2372–2377.
- Zhang, X., X.-F. Qiao, W. Shi, J.-B. Wu, D.-S. Jiang, and P.-H. Tan (2015). Phonon and raman scattering of two-dimensional transition metal dichalcogenides from monolayer, multilayer to bulk material. *Chemical Society Reviews* 44(9), 2757–2785.
- Zhao, L., R. He, K. T. Rim, T. Schiros, K. S. Kim, H. Zhou, C. Gutierrez, S. P. Chockalingam, C. J. Arguello, L. Palova, D. Nordlund, M. S. Hybertsen, D. R. Reichman, T. F. Heinz, P. Kim, A. Pinczuk, G. W. Flynn, and A. N. Pasupathy (2011). Visualizing individual nitrogen dopants in monolayer graphene. *Science* 333(6045), 999–1003.
- Zhao, X., Q. Zhang, D. Chen, and P. Lu (2010). Enhanced mechanical properties of graphene-based poly (vinyl alcohol) composites. *Macromolecules* 43(5), 2357–2363.
- Zhong, H.-X., S. Gao, J.-J. Shi, and L. Yang (2015). Quasiparticle band gaps, excitonic effects, and anisotropic optical properties of the monolayer distorted 1 t diamond-chain structures res₂ and rese₂. *Physical Review B* 92(11), 115438.
- Zhou, X., J. Cheng, Y. Zhou, T. Cao, H. Hong, Z. Liao, S. Wu, H. Peng, K. Liu, and D. Yu (2015). Strong second-harmonic generation in atomic layered gase. *Journal of the American Chemical Society* 137(25), 7994–7997.
- Zhu, W. and H. Xiao (2007). First-principles study of structural and vibrational properties of crystalline silver azide under high pressure. *Journal of Solid State Chemistry* 180(12), 3521–3528.
- Zhu, W. and H. Xiao (2008). Ab initio study of electronic structure and optical properties of heavy-metal azides: Tln₃, agn₃, and cun₃. *Journal of Computational Chemistry* 29(2), 176–184.

Zhu, W. and H. Xiao (2010). First-principles band gap criterion for impact sensitivity of energetic crystals: a review. *Structural Chemistry* 21(3), 657–665.

VITA

Date and Place of Birth: 05.05.1986, İzmir-TURKEY

EDUCATION

2011 - 2017 Doctor of Philosophy in Physics

Graduate School of Engineering and Sciences, İzmir Institute of Technology,
İzmir -Turkey

Thesis Title: ELECTRONIC, MAGNETIC, AND MECHANICAL PROPERTIES
OF NOVEL TWO DIMENSIONAL MONOLAYER MATERIALS

Supervisor: Prof. Dr. R. Tuğrul SENGER

2008 - 2011 Master of Science in Physics

Graduate School of Engineering and Sciences, İzmir Institute of Technology
İzmir -Turkey

Thesis Title: DARK ENERGY MECHANISIMS IN THE CONTEXT OF
EXTRA DIMENSIONAL MODELS

Supervisor: Prof. Dr. Recai ERDEM

2003 - 2008 Bachelor of Physics

Department of Physics, Faculty of Science, İzmir Institute of Technology
İzmir - Turkey

SELECTED PUBLICATIONS

Yagmurcukardes, M., Torun, E., Senger, R. T., Peeters, F. M., and Sahin, H. (2016).
Mg(OH)₂-WS₂ van der Waals heterobilayer: Electric field tunable band-gap crossover.
Physical Review B, 94(19), 195403.
Volume: 94, Issue 19, 2016, Pp. 195403.
<https://doi.org/10.1103/PhysRevB.94.195403>

Yagmurcukardes, M., Senger, R. T., Peeters, F. M., and Sahin, H. (2016).
Mechanical properties of monolayer GaS and GaSe crystals.
Physical Review B, 94(24), 245407.
Volume: 94, Issue 24, 2016, Pp. 245407.
<https://doi.org/10.1103/PhysRevB.94.245407>